NASA/TM-2005-213754

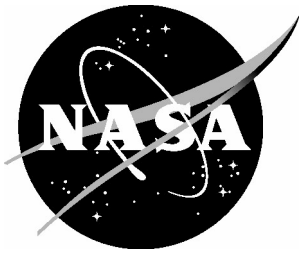

Longitudinal Aerodynamic Characteristics and Wing Pressure Distributions of a Blended-Wing-Body Configuration at Low and High Reynolds Numbers

Richard J. Re
Langley Research Center, Hampton, Virginia

August 2005

The NASA STI Program Office . . . in Profile

Since its founding, NASA has been dedicated to the advancement of aeronautics and space science. The NASA Scientific and Technical Information (STI) Program Office plays a key part in helping NASA maintain this important role.

The NASA STI Program Office is operated by Langley Research Center, the lead center for NASA's scientific and technical information. The NASA STI Program Office provides access to the NASA STI Database, the largest collection of aeronautical and space science STI in the world. The Program Office is also NASA's institutional mechanism for disseminating the results of its research and development activities. These results are published by NASA in the NASA STI Report Series, which includes the following report types:

- TECHNICAL PUBLICATION. Reports of completed research or a major significant phase of research that present the results of NASA programs and include extensive data or theoretical analysis. Includes compilations of significant scientific and technical data and information deemed to be of continuing reference value. NASA counterpart of peer-reviewed formal professional papers, but having less stringent limitations on manuscript length and extent of graphic presentations.

- TECHNICAL MEMORANDUM. Scientific and technical findings that are preliminary or of specialized interest, e.g., quick release reports, working papers, and bibliographies that contain minimal annotation. Does not contain extensive analysis.

- CONTRACTOR REPORT. Scientific and technical findings by NASA-sponsored contractors and grantees.

- CONFERENCE PUBLICATION. Collected papers from scientific and technical conferences, symposia, seminars, or other meetings sponsored or co-sponsored by NASA.

- SPECIAL PUBLICATION. Scientific, technical, or historical information from NASA programs, projects, and missions, often concerned with subjects having substantial public interest.

- TECHNICAL TRANSLATION. English-language translations of foreign scientific and technical material pertinent to NASA's mission.

Specialized services that complement the STI Program Office's diverse offerings include creating custom thesauri, building customized databases, organizing and publishing research results ... even providing videos.

For more information about the NASA STI Program Office, see the following:

- Access the NASA STI Program Home Page at ***http://www.sti.nasa.gov***

- E-mail your question via the Internet to help@sti.nasa.gov

- Fax your question to the NASA STI Help Desk at (301) 621-0134

- Phone the NASA STI Help Desk at (301) 621-0390

- Write to:
  NASA STI Help Desk
  NASA Center for AeroSpace Information
  7121 Standard Drive
  Hanover, MD 21076-1320

NASA/TM-2005-213754

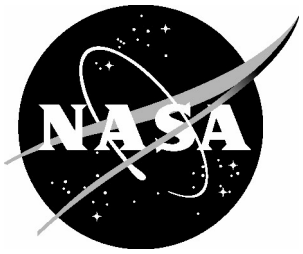

Longitudinal Aerodynamic Characteristics and Wing Pressure Distributions of a Blended-Wing-Body Configuration at Low and High Reynolds Numbers

Richard J. Re
Langley Research Center, Hampton, Virginia

National Aeronautics and
Space Administration

Langley Research Center
Hampton, Virginia 23681-2199

August 2005

Available from:

NASA Center for AeroSpace Information (CASI)
7121 Standard Drive
Hanover, MD 21076-1320
(301) 621-0390

National Technical Information Service (NTIS)
5285 Port Royal Road
Springfield, VA 22161-2171
(703) 605-6000

Summary

An investigation was conducted to obtain force balance and wing pressure data on a 0.017-scale model of an early blended-wing-body double deck subsonic transport configuration (without a simulated propulsion system installation). The purpose of the investigation was to obtain experimental data at different Reynolds numbers to validate the capability of recently developed computational fluid dynamic codes to predict the performance of such thick sectioned configurations. The design Mach number was 0.85 for a design lift coefficient of 0.45. Tests were conducted in the Langley Research Center National Transonic Facility at Reynolds numbers of 3.5×10^6, 12.3×10^6, 21.5×10^6, and 25.0×10^6 at Mach numbers within the range from 0.25 to 0.86. Data were obtained in the pitch plane only, at angles of attack within the range of –1° to 8° for Mach numbers greater than 0.25. A configuration with winglets was tested only at a Reynolds numbet of 25.0×10^6 at Mach numbers from 0.83 to 0.86.

Introduction

The performance of the traditional wing-body-tail subsonic transport passenger airplane configuration has improved greatly over the years as aerodynamic, structures, materials, propulsion, and systems technologies have matured. However, except for small incremental performance improvements due to evolution in the various disciplines, it is not likely that further large breakthrough performance improvements are possible for this type subsonic transport configuration, unless it is by utilization of configuration morphing and innovative controls.

Recent analytical studies of blended-wing-body airplane concepts have shown that there is potential for significant cruise performance improvement for the flying-wing type configuration (for large passenger capacity commercial airplanes), when compared to the traditional wing-body-tail configuration. The large capacity blended-wing-body configuration (600 or more passengers) would have a thicker than normal center section inboard for a double-deck passenger cabin and would likely incorporate advanced supercritical airfoil sections on the outboard wing panels. All the state of the art technologies available in the various disciplines, including morphing and innovative controls, would be as applicable to the blended-wing-body concept as well as to any contemporary wing-body-tail design. A detailed discussion of the promise and challenges of the blended-wing-body concept as a subsonic passenger transport airplane is contained in reference 1.

The analytic studies of the blended-wing-body concepts have utilized computational fluid dynamic (CFD) design tools developed to support the Integrated Wing Design Element of the NASA Advanced Subsonic Technology program, including an inverse design methodology coupled with a Navier Stokes flow solver and turbulence model. The design conditions selected for detailed study were for a Mach number of 0.85 and a mid-cruise lift coefficient of 0.45. To validate the applicability of the CFD codes to a configuration with such a thick center section (a chordwise maximum thickness ratio of over 17 percent) it was necessary to obtain experimental force and moment data and wing pressure distributions at high Reynolds numbers for comparison purposes. Since the design study on such a configuration was at an early stage and CFD design tool applicability and validation was the primary concern, representation of the propulsion system was not included so that the effort could be simplified. To this end a 0.017-scale model of a blended-wing-body configuration was designed and built for testing in the Langley Research Center's National Transonic Facility, which, using cryogenic nitrogen as a test medium, provides Reynolds numbers much greater than conventional wind tunnels.

The purpose of this report is to present a summary of some of the experimental force balance and wing pressure data from this investigation of an early blended-wing-body configuration. The investigation was conducted at Reynolds numbers of 3.5×10^6, 12.3×10^6, 21.5×10^6, and 25.0×10^6

at Mach numbers within the range from 0.25 to 0.86. Data were obtained in the pitch plane only, at angles of attack within the range of –1° to 8° for Mach numbers greater than 0.25. One configuration had winglets (that at this early stage of study were not intended to be well integrated with the wing design) and was tested only at a Reynolds number of 25.0 x 10^6 at Mach numbers from 0.83 to 0.86.

Symbols and Abbreviations

The longitudinal aerodynamic force and moment coefficient data are presented in the stability-axis system. Model geometric characteristics and reference constants are contained in table 1. All dimensional data are presented in U.S. customary units.

b	wing span, in.
c	local chord, in.
C_D	drag coefficient
$C_{D,base}$	drag coefficient at model base (calculated from pressure measured in sting cavity)
CFD	computational fluid dynamics
C_L	lift coefficient
$C_{L\alpha}$	lift curve slope at $C_L = 0.45$, deg^{-1}
$C_{L,pu}$	lift coefficient at pitch up
C_m	pitching-moment coefficient
$C_{m_{C_L}}$	static longitudinal stability parameter at $C_L = 0.45$, dC_m/dC_L
C_p	static pressure coefficient
$C_{p,te}$	static pressure coefficient measured at the wing trailing edge
E	wing material modulus of elasticity, psi
ESP	electronically scanned pressure module
Lower	lower surface of model
l.e.	wing leading edge
L/D_{max}	maximum lift-drag ratio
MAC	mean aerodynamic chord, in.
M_∞	free-stream Mach number
NTF	National Transonic Facility
q	free-stream dynamic pressure, psi
R_c	Reynolds number based on wing mean aerodynamic chord
t	local thickness, in.
$(t/c)_{max}$	maximum streamwise wing thickness to chord ratio
t.e.	wing trailing edge
T_t	tunnel stagnation temperature, °F
Upper	upper surface of model
x	chordwise distance from the wing leading edge, in.
y	spanwise distance from the model centerline, in.
α	angle of attack, deg
η	wing semispan location, y/(b/2)
θ	local wing twist relative to the model unloaded (jig) shape, deg
1g	the force of gravity
3-D	three dimensional

Wind Tunnel

The National Transonic Facility (located at NASA's Langley Research Center) is capable of

testing aircraft configurations from low subsonic speeds to low supersonic speeds at Reynolds numbers up to full-scale flight values (depending on aircraft size and performance envelope). The NTF is a continuous flow fan driven pressure wind tunnel that uses dry air or warm nitrogen as a test gas for low Reynolds numbers, or cryogenic nitrogen gas for high Reynolds numbers. In air or warm nitrogen operation, a heat exchanger upstream of the contraction section is utilized for airstream cooling. For this investigation the 25 foot long 8.2 by 8.2 foot test section had a total of six longitudinal slots in the floor and ceiling (porosity of 6 percent). The test section side walls were not slotted. The adjustable test section floor and ceiling divergence angles, reentry flap angles, and the step height for the slot flow reentry from the plenum were fixed for this investigation. There are four anti-turbulence screens in the settling chamber between the heat exchanger and the start of the contraction section. The contraction ratio between the settling chamber and test section throat is 15.0. Standard model support for 3-D models in the test section is provided by aft-mounted stings attached to a vertical arc sector which has a pitch range from about -11° to 19°. The interface between the arc sector and sting is a remotely controlled roll coupling with an angle range from -90° to 180°.

The NTF has an operating pressure range from about 15 to 125 psia, a temperature range from -320°F to 150°F, and a Mach number range from 0.20 to 1.20. In the cryogenic operating mode the maximum Reynolds number per foot is 146 x 10^6 at a Mach number of 1.0. Information on the NTF is contained in references 2 and 3 and some details of flow quality are presented in references 4, 5, and 6.

Model

The 0.017-scale model of the blended-wing-body configuration (shown installed in the tunnel test section in figure 1) was constructed of steel appropriate for use at cryogenic conditions. The selected model scale resulted in a model span-to-tunnel width ratio of 0.58 and a solid blockage ratio (at 0° model pitch angle) of 0.7 percent. These values are within the NTF model sizing guidelines of 0.6 and 1 percent, respectively. The sting positioned the model longitudinally on the test section centerline so that the center of the model was near the center of rotation of the arc sector support system. A plan view of the model is shown in figure 2(a) and details of the two wingtip configurations are shown in figure 2(b). Model geometric parameters and constants are presented in table 1 and streamwise maximum wing thickness ratios and the 1g mid-cruise twist distribution are presented in table 2.

The model was designed to obtain a first set of experimental data at high Reynolds numbers to validate the computational fluid dynamic design process for this type of airplane configuration. Stress computations on the model wing indicated that machined passages large enough for all the desired pressure tubes could not be installed in one wing panel. To address this problem it was decided that all the upper surface wing pressure orifices would be installed in the right wing panel and all the lower surface pressures would be installed in the left wing panel. To maintain structural aeroelastic similarity between the left and right wing panels (so that the upper and lower wing surface pressures would be obtained at the same local chord angle of attack under loaded conditions) troughing for routing the pressure tubes was identical on the lower surface of both wing panels. The lower surface was chosen for troughing so that the rougher external surface that results when filler material is used in the tubing troughs would not be on the wing upper surfaces. There were 203 functional orifices on the wings for most of the investigation and 6 orifices on the model upper surface centerline of the sting shroud. The nominal locations of the model orifices are presented in table 3 and a schematic of their locations is presented as figure 3.

The model structural design process included an iteration to adjust wing twist angles so that at the high Reynolds number design Mach number the wing would have the 1g spanwise twist variation of the full scale airplane at the mid-cruise lift coefficient. This was accomplished by having the model vendor include the pressure tubing

passages and troughs in the preliminary design of the wing structural components and then incrementally adjusting the local wing twist angles of that design to represent the proper airplane mid-cruise twist distribution of the loaded wing in the wind tunnel.

Sting support of a model of a blended-wing-body configuration in the wind tunnel becomes a challenging endeavor since the sting must pass through a major lifting surface portion of the model rather than through the aft portion of an essentially non-lifting boattailed cylindrical fuselage of a typical wing-body–tail transport configuration. CFD design effort was expended in developing a sting-shroud fairing that would cause as little flow distortion on the model as possible. The sting used for the investigation was cylindrical in shape (3.0 in. diameter) for 11.782 in. downstream of the model base where a flare angle of 1° began (fig. 2(a)).

The only model geometric variable consisted of winglets (fig. 2(b)) which were designed as an add-on to the basic wing and were not well developed as an integrated design with the wing.

Instrumentation

The model forces and moments were measured on a six-component strain gage balance which was designed for use at cryogenic temperatures and had component capacities and full-scale component calibration accuracies as shown in table 4. Model pitch angle was measured with an accelerometer package mounted to the balance block in the model nose. The laboratory environment accuracy of the accelerometer package is ±0.01°.

The static pressure orifices were installed in the wing in 7 chordwise rows at span stations (η) of 0.13, 0.27, 0.41, 0.55, 0.68, 0.80, and 0.96. There were six orifices on the model centerline (η = 0.0) three of which were on the sting shroud and three on the model ahead of the sting shroud. The nominal chordwise locations of the orifices in each row are listed in table 3 and shown schematically on the wing planform in figure 3. Upper surface orifices were installed in the right wing panel and lower surface orifices were installed in the left wing panel. The orifice diameter at the wing surface was 0.015 inches. Eighteen rearward facing pressure orifices were installed in the wing trailing edges on the right and left wing panels.

The pressures were measured by four electronically scanned pressure (ESP) modules housed in a temperature controlled enclosure in the forward portion of the model. Two of the ESP modules had a capacity of 30 psi and two had a capacity of 45 psi. The manufacturer's quoted measurement accuracy of the modules is ±0.1 percent of full scale.

Wing deformation under load was measured using photogrammetry. Details of the photogrammetric technique may be found in references 7 and 8. Wing twist data at span stations (η) of 0.17, 0.575, 0.75 and 0.915 were measured on the left wing panel (looking upstream).

Data Reduction

The force balance data are presented in coefficient form in the stability axis system, based on the reference constants given in table 1. Model pitch angle, as measured by the attitude transmitter housed in a temperature controlled enclosure in the nose of the model, was corrected for test section flow angularity to obtain model angle of attack. Test section flow angularity in the pitch plane (which was within the range 0.1° to 0.2°) was determined from force balance measurements by testing the model upright and inverted at several Mach numbers at the different Reynolds number conditions. The upflow angles determined at Mach numbers of 0.25, 0.50, and 0.70 were applied to data taken at those Mach numbers while the upflow angle determined at Mach 0.85 was applied at Mach numbers of 0.80 and above. Corrections for buoyancy, based on model volume, were computed and applied to the data.

No corrections or adjustments have been applied to the data for test section wall interference or wing aeroelastic deformation under load.

Measured drag was adjusted to the condition of freestream static pressure acting in the sting cavity at the model base. Pressures for this adjustment were measured internally near the base of the model cavity through which the sting passed by means of an ESP module located in the support system arc sector. Typical magnitudes of the base drag coefficient corrections which were subtracted from the data are presented in figure 4 as a function af angle of attack for various Mach numbers and Reynolds numbers.

Tests and Procedures

The extent of the NTF operating envelope and model safety constraints limited the maximum Reynolds number to which the model could be tested to 25.0 x 10^6. This is about half the flight Reynolds number for the full scale vehicle, but based on previous high Reynolds number research it is high enough so that only small differences in the test results are likely to occur. Data for the basic configuration were also obtained with air as the test medium at a Reynolds number of 3.5 x 10^6 so that the differences in aerodynamic and wing pressure measurements between conventional and high Reynolds number cryogenic wind tunnels for a configuration of this type could be assessed. At a Reynolds number of 3.5 x 10^6 data was obtained with boundary layer transition artificially fixed (as shown in fig. 5) and with free transition. Low speed data was obtained at Mach number 0.25 for Reynolds numbers 3.5 x 10^6 (transition fixed) and 21.5 x 10^6, and also at Mach number 0.50 for Reynolds number 3.5 x 10^6 (transition fixed) and 25.0 x 10^6. Data at Mach numbers of 0.83 and above were also obtained on the basic configuration at the intermediate Reynolds number of 12.3 x 10^6. A model configuration with winglets was tested only at a Reynolds number of 25.0 x 10^6 at Mach numbers near cruise (mini-tufts were attached to the left wing upper surface during data taking). A listing of the nominal test conditions for the various Reynolds and Mach number combinations is contained in table 5.

Models in NTF with pressure tubes (supplying calibration pressure, backing pressure, and pressure for plate movement) and electrical wires for the ESPs (which were housed in the forward portion of the model) crossing from the support sting to the balance have little effect on lift or pitching moment but can affect the accuracy of drag measurements, especially at cryogenic conditions. To minimize the restraint effects of tubing and wires on force balance readings at cryogenic conditions NTF models are routinely assembled in a test bay prior to installation in the tunnel and then cold soaked in a cryogenic chamber to determine whether significant temperature effects are indicated by the force balance readings. If significant effects are observed the model is disassembled, the instrumentation routing modified, and then, after reassembly, the cooling down process is repeated. This is done as many times as necessary to obtain an arrangement that minimizes the effect of temperature on force balance output due to increased stiffness and/or contraction of the tubes and wires. To examine the effect of tubing and wires on the model force and moment data the basic configuration was tested at a Reynolds number of 25.0 x 10^6 at Mach numbers from 0.83 through 0.86 with and without the tubes and wires connected. Since the time of this test, new procedures which in most cases eliminate the need for separate pressure and force data testing have been established and demonstrated (ref. 6).

At selected Mach numbers the model was tested upright and inverted to determine test section flow angularity in the pitch plane. This was done at each of the Reynolds numbers since flow angularity can also vary with Reynolds number.

Presentation of Results

Some of the data obtained in this investigation are presented graphically in this report. The scales used in the presentation of the aerodynamic drag data were selected based on the restraint effects of the pressure tubes and wires crossing from the model to the sting (observed in figures 6 through 9). As has sometimes been the experience in tests at cryogenic conditions there can still be a restraint effect of the tubes and wires on

force balance readings during wind-on testing despite pre-installation assembly and disassembly efforts with temperature cycling in the test bay. The aerodynamic coefficient data (figs. 6 through 9) show that there was essentially no restraint effect of the tubes and wires on the lift and pitching-moment coefficients but that there was a definite effect on drag coefficient. Therefore, to put a more reasonable perspective on the measured drag coefficient accuracy all the drag data subsequent to figures 6 through 9 have the drag coefficient scale doubled when the tubes and wires are connected. (As mentioned in the previous section much progress toward the elimination of instrumentation restraint has been made since this test was conducted.)

Measured wing twist due to aerodynamic loading relative to the unloaded model wing jig twist angle at four span stations is presented graphically in figures 10 through 13 for the various Reynolds numbers for the basic wing configuration.

Selected wing pressure data are also presented graphically as chordwise pressure coefficient plots for the various test conditions and model configurations. At cryogenic conditions the tubing to some of the wing pressure orifices either collapsed or became blocked. When this occurred the data from the affected pressure orifices were deleted from the plots.

Basic wing aeroelastic twist angles, aerodynamic force and moment balance data, and chordwise pressure coefficient distributions are presented in the following figures:

Wing aeroelastic twist angle relative to the unloaded condition for the basic configuration

$R_c = 3.5 \times 10^6$

$M_\infty = 0.25$ to 0.86 (Fixed transition) — Figure 10

$R_c = 12.3 \times 10^6$

$M_\infty = 0.83$ to 0.86 — 11

$R_c = 25.0 \times 10^6$

$M_\infty = 0.83$ to 0.86 — 12

$M_\infty = 0.50$ to 0.85 (Tubes and wires disconnected) — 13

Longitudinal aerodynamic characteristics of the basic configuration at

$R_c = 3.5 \times 10^6$

$M_\infty = 0.25$ and 0.50 (Fixed transition) — Figure 14

$M_\infty = 0.70$ to 0.86 (Fixed transition) — 15

$M_\infty = 0.80$ to 0.86 (Free transition) — 16

$R_c = 12.3 \times 10^6$

$M_\infty = 0.83$ to 0.86 — 17

$R_c = 21.5 \times 10^6$

$M_\infty = 0.25$ — 18

$R_c = 25.0 \times 10^6$

$M_\infty = 0.83$ to 0.86 — 19

$M_\infty = 0.50$ to 0.85 (Tubes and wires disconnected) — 20

Longitudinal aerodynamic characteristics of the model with winglets at

$R_c = 25.0 \times 10^6$

$M_\infty = 0.83$ to 0.86 — Figure 21

Wing chordwise pressure coefficient distributions at

$R_c = 3.5 \times 10^6$, basic configuration (Fixed transition)

$M_\infty = 0.25$ — Figure 22

$M_\infty = 0.50$ — 23

$M_\infty = 0.70$ 24
$M_\infty = 0.80$ 25
$M_\infty = 0.83$ 26
$M_\infty = 0.84$ 27
$M_\infty = 0.85$ 28
$M_\infty = 0.86$ 29

$R_c = 3.5 \times 10^6$, basic configuration (Free transition)
$M_\infty = 0.85$ 30

$R_c = 12.3 \times 10^6$, basic configuration
$M_\infty = 0.83$ 31
$M_\infty = 0.84$ 32
$M_\infty = 0.85$ 33
$M_\infty = 0.86$ 34

$R_c = 21.5 \times 10^6$, basic configuration
$M_\infty = 0.25$ 35

$R_c = 25.0 \times 10^6$, basic configuration
$M_\infty = 0.83$ 36
$M_\infty = 0.84$ 37
$M_\infty = 0.85$ 38
$M_\infty = 0.86$ 39

$R_c = 25.0 \times 10^6$, configuration with winglets
$M_\infty = 0.83$ 40
$M_\infty = 0.84$ 41
$M_\infty = 0.85$ 42

Discussion of Results

This report presents experimental force and moment and pressure coefficient data obtained from the blended-wing-body wind tunnel investigation. Validation of the applicability of the CFD subsonic transport design and analysis tools to such a thick winged configuration by comparison of CFD predictions to the experimental data is beyond the scope of this report.

Effect of ESP Pressure Tubing and Wires

The steps taken during model buildup to minimize the effect of pressure tubing and wires crossing from the non-metric sting to the balance-supported model are described in the Tests and Procedures section and their effect on the force balance data is discussed qualitatively in the Presentation of Results section.

Wind-on tests with the pressure tubing and wires disconnected were conducted only on the basic configuration at the highest Reynolds number and comparison of their effect on the force balance data could only be made in the vicinity of the cruise Mach number. In figures 6(a) through 9(a) the lift and pitching-moment coefficient data comparisons show no discernible effect of the tubes and wires at Mach numbers from 0.83 through 0.86. However drag coefficient with the tubes and wires disconnected (figures 6(b) through 9(b)) was between 0.0005 and 0.0010 lower over this Mach number range at lift coefficients in the range of most interest. Therefore, for purposes of discussion, drag coefficient comparisons that can be made when the tubes and wires are connected should be viewed qualitatively while the limited amount of data obtained with the tubes and wires disconnected (basic configuration for Mach numbers 0.50 through 0.86 at a

Reynolds number of 25.0 x 10^6, figure 20) should be referred to when an absolute level of drag coefficient is desired.

Aeroelastic Effects

While the model force balance and pressure data were being recorded wing twist angles relative to the unloaded wing (wind-off) condition were measured photogrammetrically (refs. 7 and 8) at four span stations. Twist angles for the basic configuration over the Mach number and angle of attack ranges are presented in figures 10 through 13 at Reynolds numbers of 3.5 x 10^6, 12.3 x 10^6, and 25.0 x 10^6.

These data indicate, as would be expected, that the aeroelastic twist resulting from increased dynamic pressure at the higher Reynolds numbers was small on the thick inboard wing sections because of the structural rigidity. The differences shown in the inboard pressure distributions should therefore be due to Reynolds number and dynamic pressure although at the lowest Reynolds number the state of the boundary layer inboard may also be a factor due to the inability to artificially fix boundary layer transition inboard of span station 0.361 (see figure 5). For a given outboard wing section significant aeroelastic effects (compare figures 10 through 13) occurred for a given angle of attack when Reynolds number and dynamic pressure were increased and this is especially noticeable in the wing upper surface pressure distributions at span stations 0.80 and 0.96 (e.g. compare data from figures 28(b), 33(b), and 38(b) at specific conditions). Selected data from these figures at the cruise Mach number has been replotted in figure 43 to illustrate the pressure distribution differences at a constant angle of attack (3.3°) and also at a constant lift coefficient (0.5).

Effect of Fixing Transition at $R_c = 3.5 \times 10^6$

At a Reynolds number of 3.5 x 10^6 boundary layer transition was artificially fixed on the upper and lower surfaces of the outboard portion of the wing of the basic configuration by means of cylindrical disks (figure 5). The transition fixing arrangement was intended to duplicate (at a Reynolds number of 3.5 x 10^6) the trailing-edge boundary layer thickness predicted for a Reynolds number of 25.0 x 10^6 at the Mach number 0.85 mid-cruise condition. This was done to provide comparative experimental data (figures 14 and 15) at a low Reynolds number so that a level of confidence (relative to high Reynolds number data) could be gained for results obtained from future tests of similar configurations in conventional wind tunnels. Tests with free transition on the model were also conducted at this low Reynolds number at Mach numbers from 0.80 to 0.86 (figure 16) since it has been found in tests of conventional transport configurations that the free transition condition at low Reynolds numbers often yields a better simulation for some flight Reynolds number aerodynamic characteristics at angles of attack above that for cruise.

At Mach numbers 0.80 to 0.86 comparison of the aerodynamic characteristics with and without fixed transition indicate there was a slight decrease in lift over the angle of attack range and a decrease in nose down pitching moment over the lift coefficient range with transition fixed. The decrease in nose down pitching moment increased with lift coefficient and Mach number so that there was a decrease in stability at the higher lift coefficients with transition fixed.

Comparison of data obtained at Reynolds number 3.5 x 10^6 with fixed (fig. 15) and free (fig. 16) transition with Reynolds number 25.0 x 10^6 data (fig. 19) at angles of attack above that for cruise lift indicates that for this configuration neither low Reynolds number transition condition was a significantly better representation of the high Reynolds number aerodynamic characteristics at high angles of attack.

Reynolds Number Effects on the Basic Configuration

The model was longitudinally stable over a range of lift coefficients to well above that for cruise at all Mach numbers and exhibited no abrupt pitch up (or stall) tendencies at Mach numbers greater than 0.25. The trapezoidal wing

reference planform selected (dashed line in figure 2(a)) placed considerable inboard blended planform area well aft of the moment reference center and, as is shown in the pressure distributions, loading in this area contributes to the large nose down pitching-moment coefficients measured. On a configuration such as this these moments would be very difficult to trim (with respect to the moment reference center selected) since by design there are no far aft airframe components to provide a long moment arm for a reasonable trimming force.

A limited amount of testing was done at a Mach number of 0.25 at Reynolds numbers of 3.5×10^6 (transition fixed, figure 14) and 21.5×10^6 (figure 18) to determine Reynolds number effects on the longitudinal aerodynamic characteristics of the basic configuration at low speeds. The model was longitudinally stable over a wide range of lift coefficients at this Mach number and the level of nose down pitching moment is such that significant control forces would be required to trim. Comparison of the force and moment coefficient data at the two Reynolds numbers indicates large differences at high angles of attack. At a Reynolds number of 21.5×10^6 the lift curve was more nearly linear but showed an abrupt stall at about 11° angle of attack which was reflected in the pitch curve by an abrupt pitch up at a lift coefficient of 1.4. At a Reynolds number of 3.5×10^6 neither the lift nor pitch curves showed an abrupt change in trend although there was a gentle transition to pitch up at a lift coefficient of 1.1. These effects appear to be a result of differences in upper surface flow separation on the wing outboard of station 0.41 as shown in the chordwise pressure distributions of figures 22(b) and 35(b). At the high Reynolds number separation occurred at lower angles of attack at span stations 0.55, 0.68, and 0.80 (the area of the wing in the vicinity of the trailing-edge kink, figure 3). The separation at stations 0.68 and 0.80 extended forward to the wing leading edge at the high Reynolds number which may explain the abruptness of the breaks in the lift and pitch curves. However at span station 0.96 the upper surface leading-edge pressure peak was maintained to a higher angle of attack at the higher Reynolds number. Due to the earlier collapse of the high angle of attack leading-edge suction peak at a Reynolds number of 3.5×10^6 (compare figures 22(b) and 35(b)) drag coefficient in the lift coefficient range 1.1 to 1.4 (angle of attack range 8° to 10°) was considerably lower at the high Reynolds number. These pitching moment and drag differences are most likely due to greater local aeroelastic twist on the outboard portion of the wing at the higher Reynolds number (higher dynamic pressure). However, aeroelastic data was not obtained at Reynolds number 21.5×10^6 so no definitive twist comparisons can be made.

It should be noted that the model had a clean wing configuration and that under actual flight conditions at this low Mach number a commercial transport airplane would likely deploy control surfaces such as leading- and trailing-edge devices to improve longitudinal aerodynamic control and maintain a more level airplane attitude.

The basic configuration was tested at two Reynolds numbers at Mach numbers of 0.50, 0.70, and 0.80 and at three Reynolds numbers at Mach numbers above 0.80. However, differences shown in the data are not solely due to Reynolds number but also include the effects of aeroelastic twist differences since the parameter q/E was not held constant for a given Mach number at the different Reynolds numbers. The most accurate comparisons for Reynolds number effects on the model aerodynamic characteristics can be made at the low lift coefficients where the wing is lightly loaded and the effect of differing dynamic pressure on wing twist is minimized. The same reasoning applies to comparisons of wing pressure distributions although at higher lift coefficients the pressure data from $\eta = 0.55$ inboard will only be slightly affected by dynamic pressure differences because of the large inboard wing thickness. For reference purposes the pertinent values of q/E are contained in the data figure keys for a better understanding of the tunnel flow conditions at which the data were obtained.

At Mach numbers of 0.50 and 0.70 the low Reynolds number lift curves were shifted in the

positive angle of attack direction by about 0.2° relative to the high Reynolds number lift curves in the low lift coefficient range and nose down pitching-moment coefficient was decreased by about 0.02 at lift coefficients up to about 0.45 (compare figures 14(a) and 15(a) with 20(a)). Above that lift coefficient the decrease in nose down pitching-moment coefficient was somewhat greater. At Mach number 0.80 the effects of Reynolds number were similar except that the lift coefficient at which pitch up occurred was about 0.07 lower at the high Reynolds number.

At Mach number 0.85 at the low lift coefficients the low Reynolds number lift curve and pitching moment curve shifts were similar to those observed at Mach number 0.80 (compare figs. 15(a) and 19(a) or 20(a)). These differences are also illustrated in figures 44 and 45 which are summary plots of lift and pitch parameters at the cruise lift coefficient of 0.45 for the various model configurations and test conditions. At the cruise lift coefficient the model was stable throughout the Mach number and Reynolds number ranges and stability increased with Mach number up to a Mach number of 0.85. The magnitude of nose down pitching moment at cruise lift coefficient increased with Mach number and Reynolds number up to a Mach number of 0.86.

Pressure distribution comparisons for 3.3° angle of attack at a Mach number of 0.85 are shown in figure 43(a) for three Reynolds numbers and indicate the upper surface wing shock is further aft at the two higher Reynolds numbers at span stations inboard of 0.68. Outboard of that station where local wing twist (figs. 10 to 12) is most affected by the dynamic pressure differences the shock is further aft for the low Reynolds number which means, when coupled with the further forward shock location inboard, that the wing shock has greater sweep at the low Reynolds number. The increased aft loading on the inboard portion of the wing at the higher Reynolds numbers influences a much larger area of the wing (lift coefficient at the highest Reynolds number was 9 percent greater) than the increased outboard loading at the low Reynolds number as indicated by the increase in nose down pitching-moment coefficient (compare pitching-moment coefficient at 3.3° angle of attack in figures 15(a) and 19(a) at Mach number 0.85).

To obtain the same lift coefficient (0.5) at the low Reynolds number as at the highest Reynolds number it was necessary to set the model angle of attack 0.3° higher (see fig. 43(b) key). The wing still had increased aft loading inboard at the highest Reynolds number relative to the low Reynolds number but at the lowest Reynolds number the forward loading outboard of the 0.27 span station was slightly higher due to the higher angle of attack and lower outboard twist angles at the reduced dynamic pressure.

There were differences in the lift coefficient at which pitch up occurred (figure 46) and at the high Reynolds number the model was quite unstable above that lift coefficient. Some of the differences at high lift coefficients may be influenced by differences in aeroelastic twist but at the very low lift coefficients dynamic pressure differences (aeroelastics) cannot be viewed as the dominant effect.

To draw qualitative conclusions for the effect of Reynolds number on drag at Mach numbers above 0.80 it would be consistent to compare only data from the configurations with the tubes and wires connected (figures 15(b), 19(b), 44, and 45). The drag coefficient for the basic configuration with the tubes and wires disconnected (figures 20 and 44) should be viewed as the most accurate representation of drag coefficient. At a Reynolds number of 25.0×10^6 and at the design Mach number of 0.85 the basic configuration (with the tubes and wires disconnected) reached a maximum untrimmed lift-drag ratio of 20.7 at a lift coefficient of about 0.49 (fig. 45). The steepness of the maximum lift-drag ratio drop off above Mach number 0.85 indicates that this is the beginning of the drag rise and that in all likelihood measures taken to trim the configuration or add a propulsion system would cause the drag rise to start at a lower Mach number and put the configuration higher on the drag rise. A complete configuration incorporating this wing would probably perform more efficiently at a Mach number of about 0.84.

Effect of Winglets at $R_c = 25.0 \times 10^6$

The model was also tested with winglets (shown in figure 2(b)) at Mach numbers from 0.83 to 0.86 at a Reynolds number of 25.0×10^6 (fig. 21). Winglet integration with the baseline wing was not a priority at this stage of blended-wing-body development and the resulting configuration should not be considered to be geometrically or aerodynamically optimized.

Rapidly changing flow conditions over the wing upper surface in the vicinity of the trailing-edge kink had been predicted during computational design and this model configuration was selected for the installation of minitufts to obtain visual details of the flow in that area. Since tunnel occupancy time was critical the required mini-tufts were attached to the aft portion of the left wing upper surface at the same time as the winglets were installed to avoid the additional test section access that would have been required for a separate series of tests. Therefore all the force balance and pressure data obtained for this configuration was taken with the minitufts attached. Since the minitufts were on the left wing and all the upper surface orifices were on the right wing there were no local minituft interference effects on upper surface pressure measurements. Comparison of the force and moment data indicates that at high lift coefficients the configuration with winglets had greater lift at a given angle of attack at all the Mach numbers tested (compare figs. 19(a) and 21(a)). This would, at least in part, be attributable to the increase in effective wing area and aspect ratio since the winglets were canted outboard at a 65° angle relative to the horizontal (fig. 2(b)). Comparison of the wing upper surface pressure distributions for the two configurations indicates that at the $\eta = 0.96$ span station the configuration with the winglets is more highly loaded over the aft 50 percent of the chord especially at the higher angles of attack (compare figures 36(b) through 39(b) with figures 40(b) through 42(b)). The increased aft loading difference at the wingtip is reflected in the pitching-moment coefficient data which shows larger nose down pitching-moment coefficients and greater longitudinal stability with the winglets installed. Pitch up occurred at a slightly higher lift coefficient with the winglets installed.

Wing Trailing-edge Pressure Coefficients

Buffet onset is an important factor for the performance of subsonic commercial transports in that the margin between the angle of attack for level flight and buffet onset can be quite small especially early in the flight at cruise altitude (airplane heavy with fuel). Over the years the ability to accurately predict or obtain buffet onset and buffet boundaries for full scale airplanes from wind tunnel measurements has left much to be desired. Low Reynolds number wind tunnel model measurements of forces, moments, trailing-edge pressures, or wing bending moments have been used in the past but no technique has yet been found to be completely satisfactory. Even in wind tunnels capable of testing at high or even full scale Reynolds numbers the onset of buffeting is usually not well predicted.

The only data from this investigation intended to give some direct insight into the onset of buffet is that obtained from the wing trailing-edge pressure measurements (to sense local flow separation). Both wings had a number of rearward facing pressure orifices in the trailing edge; some were at the same span stations as the rows of upper and lower surface pressure orifices and some were at intermediate span stations (table 3). These were very small orifices and at times, especially at cryogenic conditions, some of them were not functioning properly. The data from any trailing-edge orifice that failed to leak check properly or showed signs of becoming plugged during wind-on testing has been deleted from figures 47 through 51 although there remain a few instances where the measured trailing-edge pressure data obtained at the same span station on the opposite wings appear to differ considerably (e.g. at $M_\infty = 0.83$ and 0.86 at span station 0.80 in figure 50). For example examination of upper (right wing) and lower (left wing) surface pressures (fig. 39) just forward of the trailing edge indicate that local flow conditions on the two wings differed enough such that neither trailing-edge pressure could be discarded as questionable.

When encountered, the breaks in the variation of wing trailing-edge pressure coefficient with angle of attack (figs. 47 through 51) for span stations between 0.55 and 0.80 generally occurred at about the same angle of attack as the breaks (or $dC_m/dC_L = 0.0$) in the pitch curves. The only sharp break in the lift curves (which was coincident with $dC_m/dC_L = 0.0$) occurred at Mach number 0.25 at Reynolds number 21.5 x 10^6 (fig. 18(a)) although there was a slight break in the lift curve at this Mach number at a Reynolds number of 3.5 x 10^6 (fig. 14) at the same lift coefficient. However this slight break occurred about 4° higher in angle of attack than $dC_m/dC_L = 0.0$. The upper surface pressure distributions at the wingtip at high angles of attack (fig. 22(b) and 35(b)) showed markedly different section loadings at span stations 0.68, 0.80, and 0.96 with extensive separation in some cases that will obviously affect pressure at the trailing edge. The trailing-edge pressure coefficients for these two Reynolds numbers at Mach number 0.25 (fig. 47) show that there was a large difference in trend with angle of attack at span station 0.88. The aft portion of the wing in this area was expected to be a critical flow area since the geometry was transitioning from a large-chord thick inboard wing section with forward trailing-edge sweep to a more traditional sweptback transport wing geometry outboard.

Concluding Remarks

A model of a blended-wing-body subsonic transport configuration (without representation of a propulsion system) has been tested in the NASA National Transonic Facility at the Langley Research Center at Mach numbers from 0.25 to 0.86. The purpose of the investigation was to obtain the longitudinal aerodynamic characteristics and wing pressure data at low and high Reynolds numbers so that the applicability of recently developed subsonic transport design and analysis techniques to configurations with unusually thick inboard wing sections could be determined. The design cruise Mach number was 0.85.

At Mach number 0.25 and Reynolds number 25.0 x 10^6 the model remained stable up to a lift coefficient of 1.4 where a sharp break occurred and the model became unstable. At Reynolds number 3.5 x 10^6 a much more gradual transition to instability occurred at a lift coefficient of 1.1.

At the cruise lift coefficient (0.45) the model was stable throughout the Mach number and Reynolds number ranges and stability increased with Mach number up to a Mach number of 0.85. The magnitude of nose down pitching moment increased with Mach number and Reynolds number up to a Mach number of 0.86.

The untrimmed maximum lift-drag ratio was 20.7 (at a lift coefficient of 0.49) at a Mach number of 0.85 at a Reynolds number of 25.0 x 10^6.

The variation of untrimmed maximum lift-drag ratio and drag coefficient (at cruise lift coefficient) with Mach number indicates that at Mach number 0.85 the configuration is on the start of the drag rise.

References

1. Roman, D; Allen, J. B.; and Liebeck, R. H.: *Aerodynamic Design Challenges of the Blended-Wing-Body Subsonic Transport*. AIAA-2000-4335, 2000.

2. Wahls, R. A.: *The National Transonic Facility: A Research Retrospective (Invited)*. AIAA-2001-0754, January 2001.

3. Fuller, Dennis E.: *Guide for Users of the National Transonic Facility*. NASA TM-83124, 1981.

4. Igoe, William B.: *Analysis of Fluctuating Static Pressure Measurements in a Large High Reynolds Number Transonic Cryogenic Wind Tunnel*. NASA TP-3475, 1996.

5. Bobbitt, C., Jr.; Everhart, J.; Foster, J.; Hill, J.; McHatton, R.; and Tomek, B.: *National Transonic Facility Characterization Status*. AIAA-2000-0293, January 2000.

6. Kilgore, W. A.; Balakrishna, S.; Bobbitt, C. W., Jr.; and Adcock, J. B.: *Recent National Transonic Facility Test Process Improvements (Invited)*. AIAA-2001-0756, January 2001.

7. Burner, A. W.; and Martinson, S. D.: *Automated Wing Twist and Bending Measureements under Aerodynamic Load*. AIAA-96-2253, June 1996.

8. Burner, A. W.; Wahls, R. A.; and Goad, W. K.: *Wing Twist Measurements at the National Transonic Facility*. NASA Technical Memorandum 110229, 1996.

Table 1. Model Geometric Characteristics

Wing:	
Reference area	326.269 sq in.
Mean aerodynamic chord	6.2641 in.
Span	57.12 in.
Root chord (trapezoidal wing)	8.430 in.
Tip chord (trapezoidal wing)	2.529 in.
Aspect ratio (trapezoidal wing)	10.0
l.e. sweep (trapezoidal geometry)	37.144°
c/4 sweep (trapezoidal geometry)	35.00°
t.e. sweep (trapezoidal geometry)	24.874°
Dihedral	3.0°
On model centerline:	
Length	30.702 in.
Base diameter	3.662 in.
Winglet (in plane of winglet):	
Area (true)	5.4576 sq in.
MAC	1.7308 in.
Semi span	2.4930 in.
Root chord	2.3626 in.
Tip chord	0.8269 in.
Aspect ratio	2.298
l.e. sweep	60.0°
c/4 sweep	48.298°
t.e. sweep	34.099°
Dihederal (from horizontal)	65.0°

Table 2. Wing Thickness and 1g Twist Distributions for the $M_\infty = 0.85$ Mid-cruise Condition

η	Twist, deg	$(t/c)_{max}$
0.00	0.81	0.134
.02	.80	.135
.045	.63	.140
.085	.63	.149
.13	.81	.163
.18	.71	.174
.215	.56	.177
.255	.62	.162
.312	.70	.138
.36	.60	.127
.405	.30	.121
.45	-.08	.111
.49	-.54	.098
.532	-1.04	.088
.59	-1.36	.085
.612	-1.54	.088
.664	-1.50	.092
.715	-1.55	.095
.768	-1.92	.096
.82	-2.44	.095
.872	-2.57	.093
.92	-2.74	.093
.97	-3.43	.095
.996	-4.17	.098

Table 3. Nominal Model Pressure Orifice Locations

x/c locations at – η =														x/c = 1.00	
0.0	0.13		0.27		0.41		0.55		0.68		0.80		0.96		
Upper	Upper	Lower	Upper	Lower	Upper	Lower	Upper	Lower	Upper	Lower	Upper	Lower	Upper	η	Wing
0.50	0.23	0.40	0.02	0.00	0.02	0.00	0.02	0.00	0.02	0.00	0.02	0.00	0.00	0.13	Left
.56	.29	.50	.05	.02	.05	.02	.05	.05	.05	.05	.05	.05	.02	.13	Right
.62	.35	.55	.11	.05	.11	.05	.11	.10	.11	.10	.11	.10	.05	.27	Left
.68	.47	.60	.17	.10	.17	.10	.23	.30	.17	.20	.17	.40	.10	.27	Right
.74	.52	.65	.23	.20	.23	.20	.29	.40	.23	.30	.23	.50	.20	.41	Left
.80	.56	.75	.29	.30	.29	.30	.35	.60	.29	.40	.29	.70	.25	.48	Left
	.60	.85	.35	.40	.35	.40	.41	.70	.35	.50	.35	.80	.35	.48	Right
	.64	.95	.41	.50	.41	.50	.47	.80	.40	.70	.40	.90	.40	.55	Left
	.68		.47	.55	.47	.55	.56	.90	.45	.80	.45	.95	.45	.55	Right
	.72		.52	.60	.52	.60	.64	.95	.50	.90	.50		.50	.62	Left
	.76		.56	.65	.56	.65	.68	.97	.55	.95	.60		.55	.62	Right
	.80		.60	.75	.60	.75	.72		.60	.97	.65		.60	.68	Left
	.86		.68	.85	.64	.85	.76		.65		.71		.65	.74	Left
	.92		.72	.95	.68	.95	.80		.71		.77		.70	.80	Left
			.76		.72		.92		.83		.83		.75	.80	Right
			.80		.76				.95		.90		.80	.88	Left
			.86		.80						.95		.85	.88	Right
					.86								.90	.96	Right
					.92										

Table 4. Maximum Balance Capacities and Calibration Accuracies

Balance component	Full scale load	Accuracy in % of full scale
Normal force	±6500 lbf	±0.09
Axial force	±400 lbf	±0.20
Pitching moment	±13000in-lbf	±0.12
Rolling moment	±9000 in-lbf	±0.20
Yawing moment	±6500 in-lbf	±0.22
Side force	±4000 lbf	±0.17

Table 5. Nominal Tunnel Test Conditions

$R_c \times 10^{-6}$	M_∞	$q/E \times 10^6$	T_t, °F
3.5	0.25	0.106	120
↓	.50	.202	↓
	.70	.267	
	.80	.295	
	.83	.303	
	.84	.304	
	.85	.308	
↓	.86	.310	↓
12.3	0.83	0.413	-160
↓	.84	.417	↓
	.85	.420	
↓	.86	.424	↓

$R_c \times 10^{-6}$	M_∞	$q/E \times 10^6$	T_t, °F
21.5	0.25	0.153	-250
25.0	0.50	0.319	-257
↓	.70	.417	↓
	.80	.456	
	.83	.468	
	.84	.471	
	.85	.476	
↓	.86	.479	↓

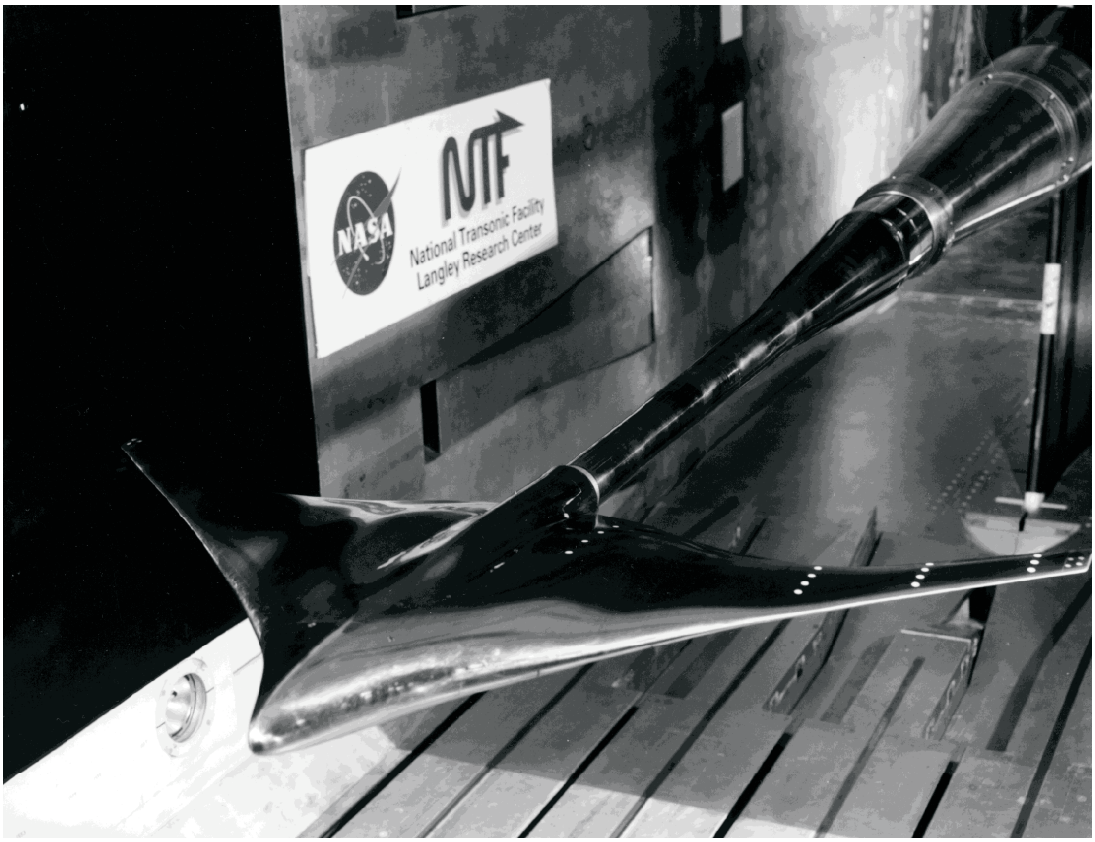

Figure 1. Photograph of basic 0.017 scale model installed in National Transonic Facility.

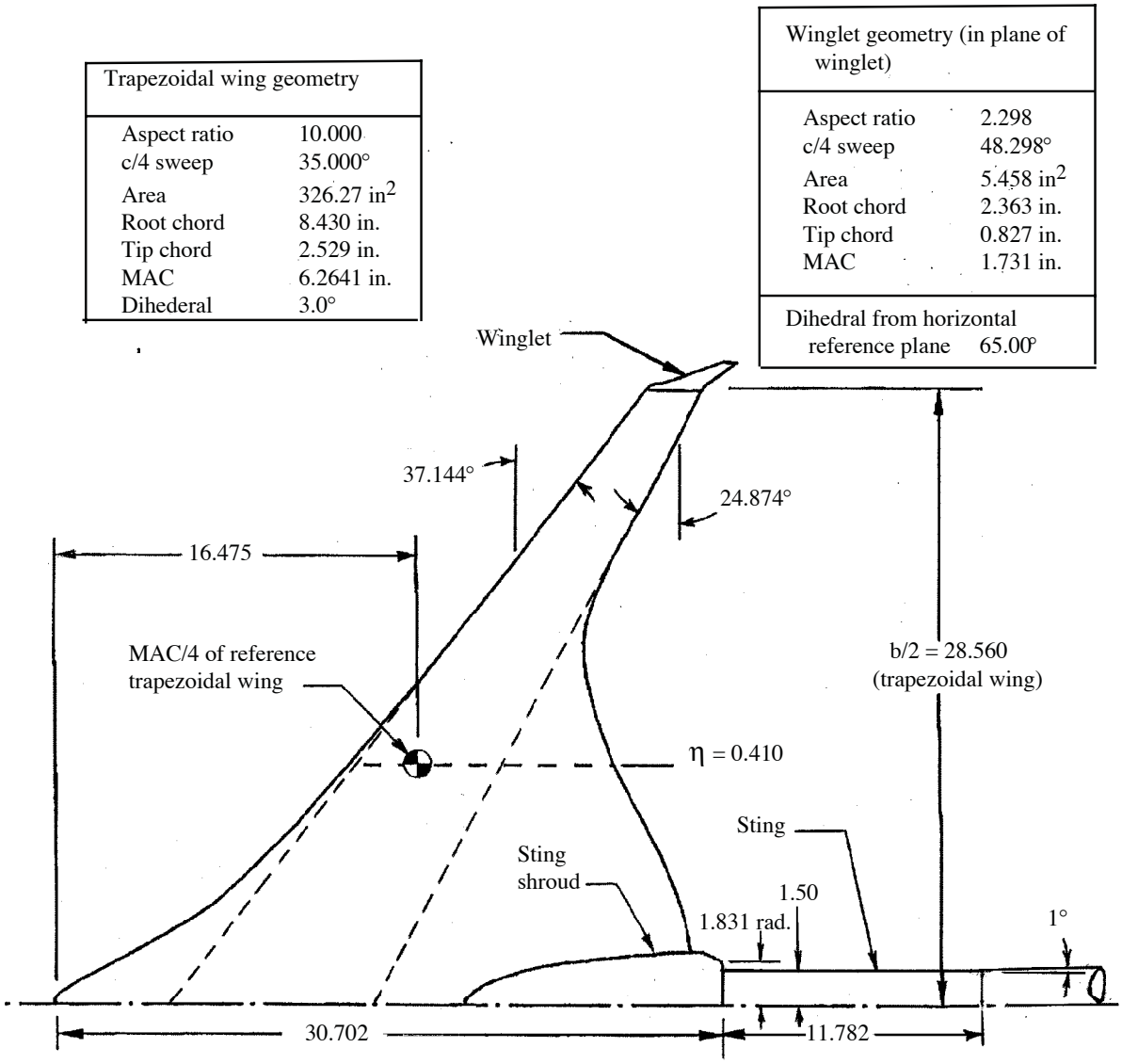

(a) Plan view of model with winglets.

Figure 2. Plan view sketch of model and wingtip geometry. (All dimensions are in inches unless otherwise indicated.)

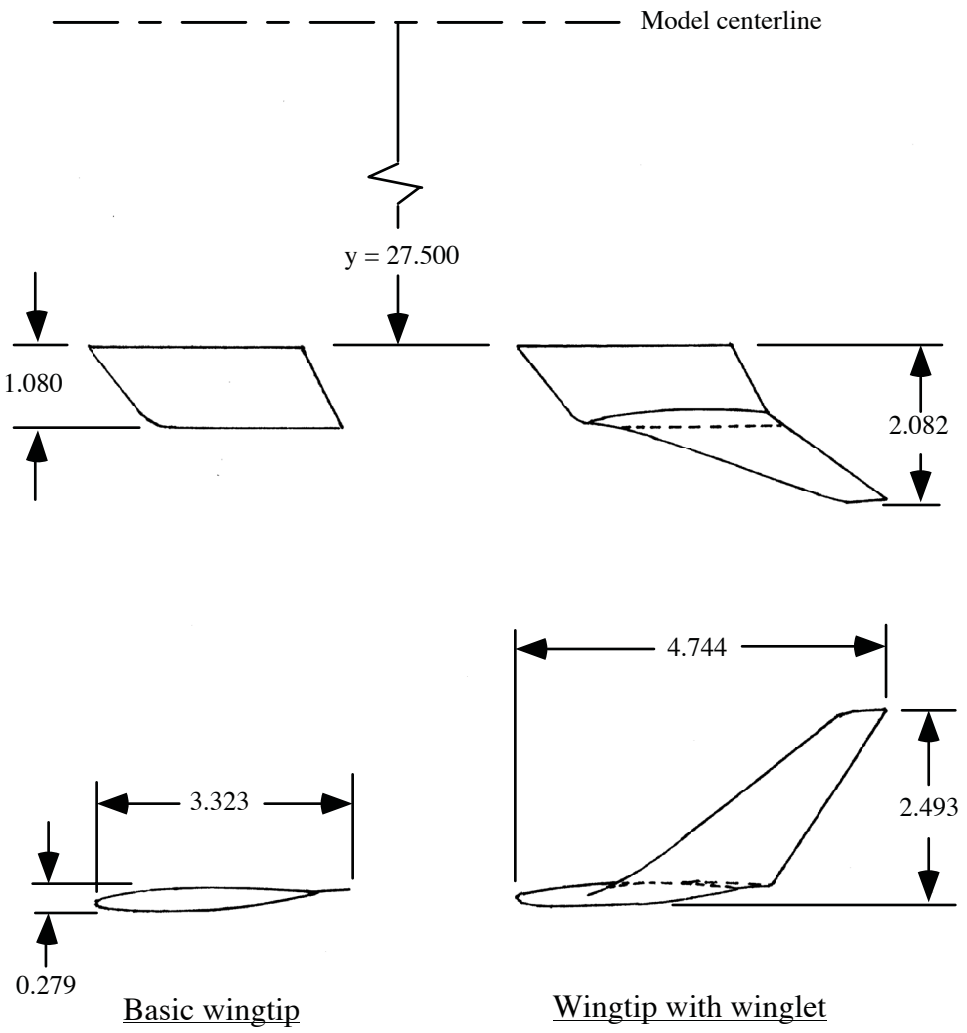

(b) Wingtip configuration.

Figure 2. Concluded.

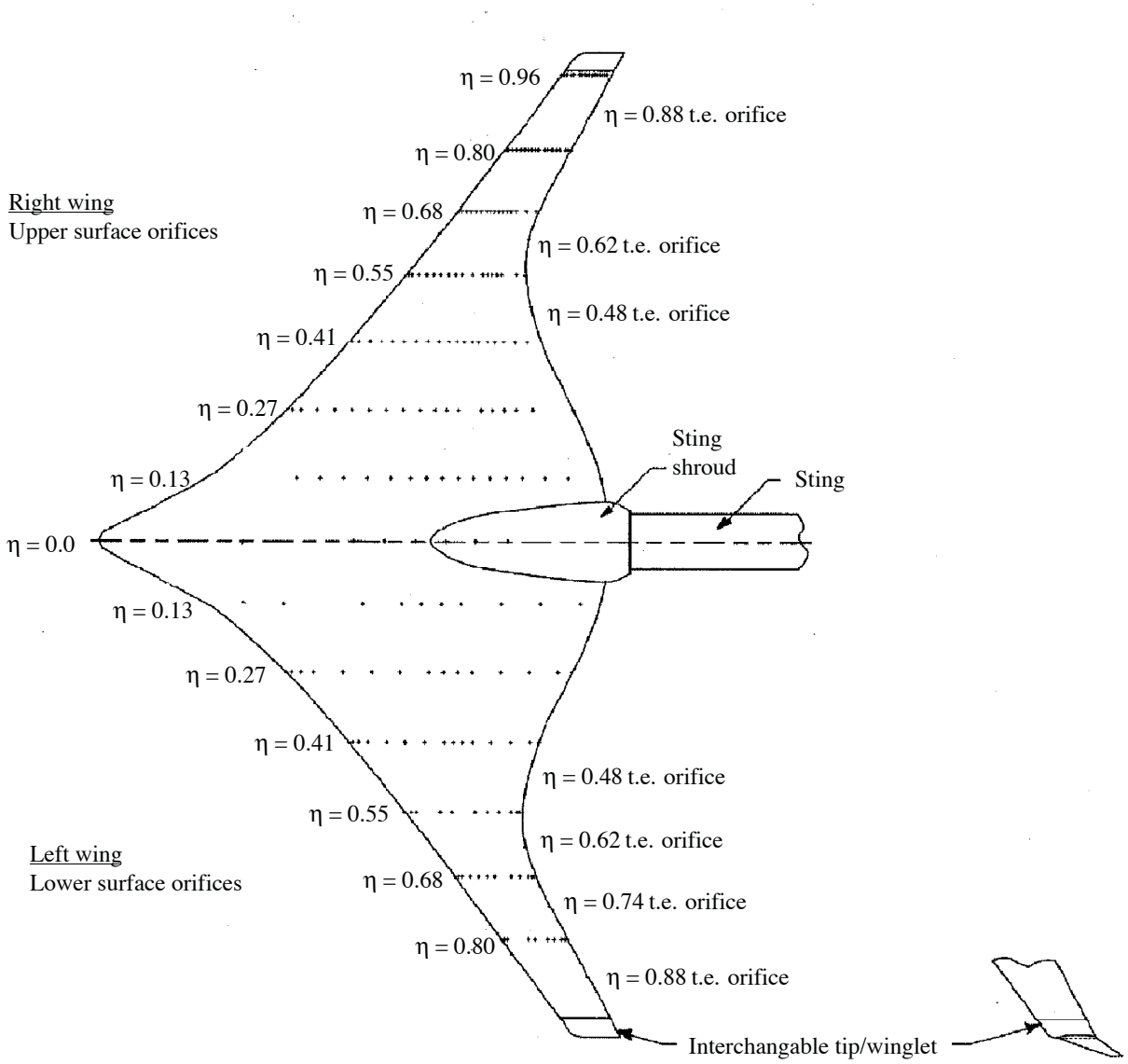

Figure 3. Plan view sketch showing distribution of pressure orifices on the wing upper and lower surfaces and in the wing trailing edge.

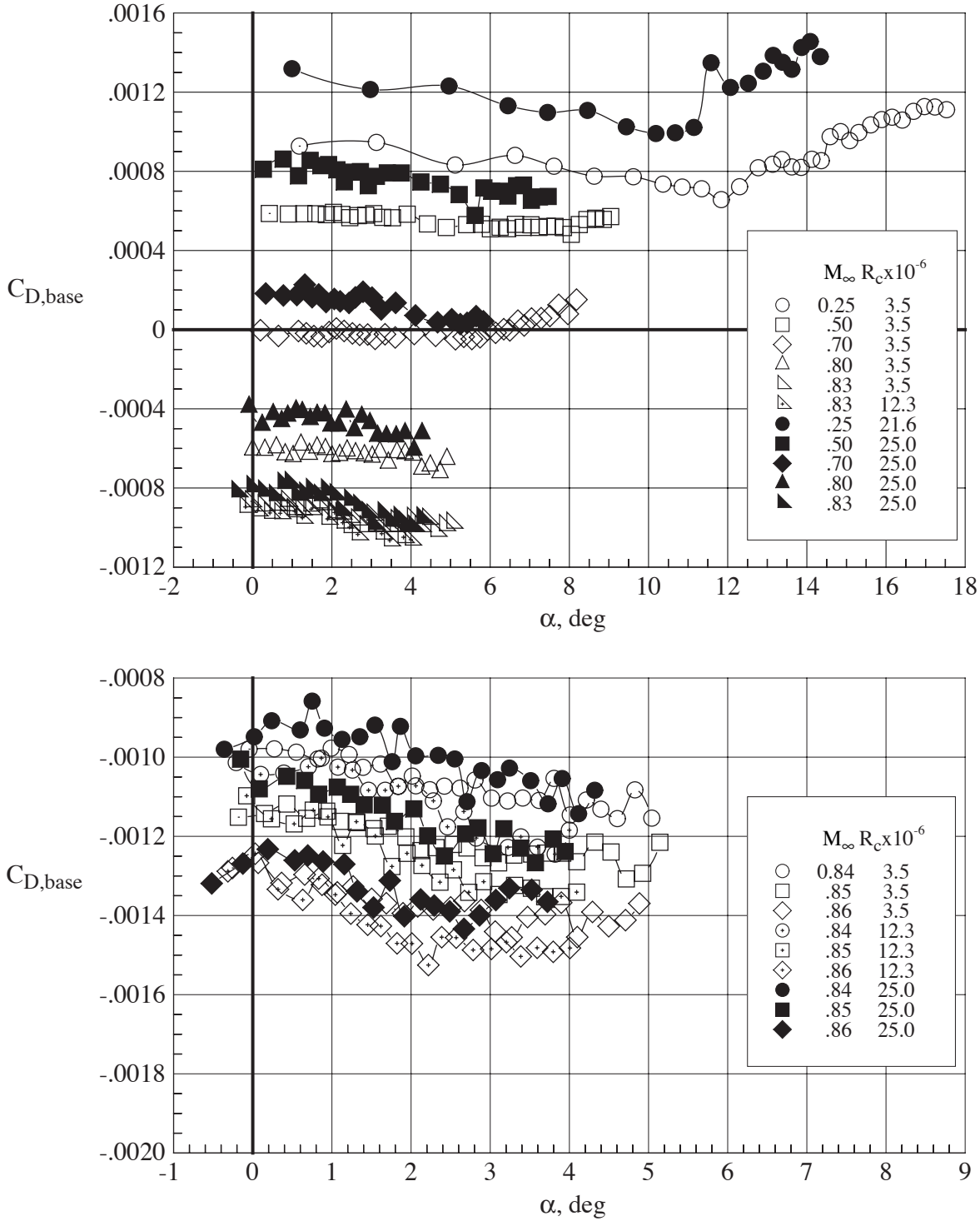

Figure 4. Base drag coefficient of the basic configuration at various Mach and Reynolds number conditions.

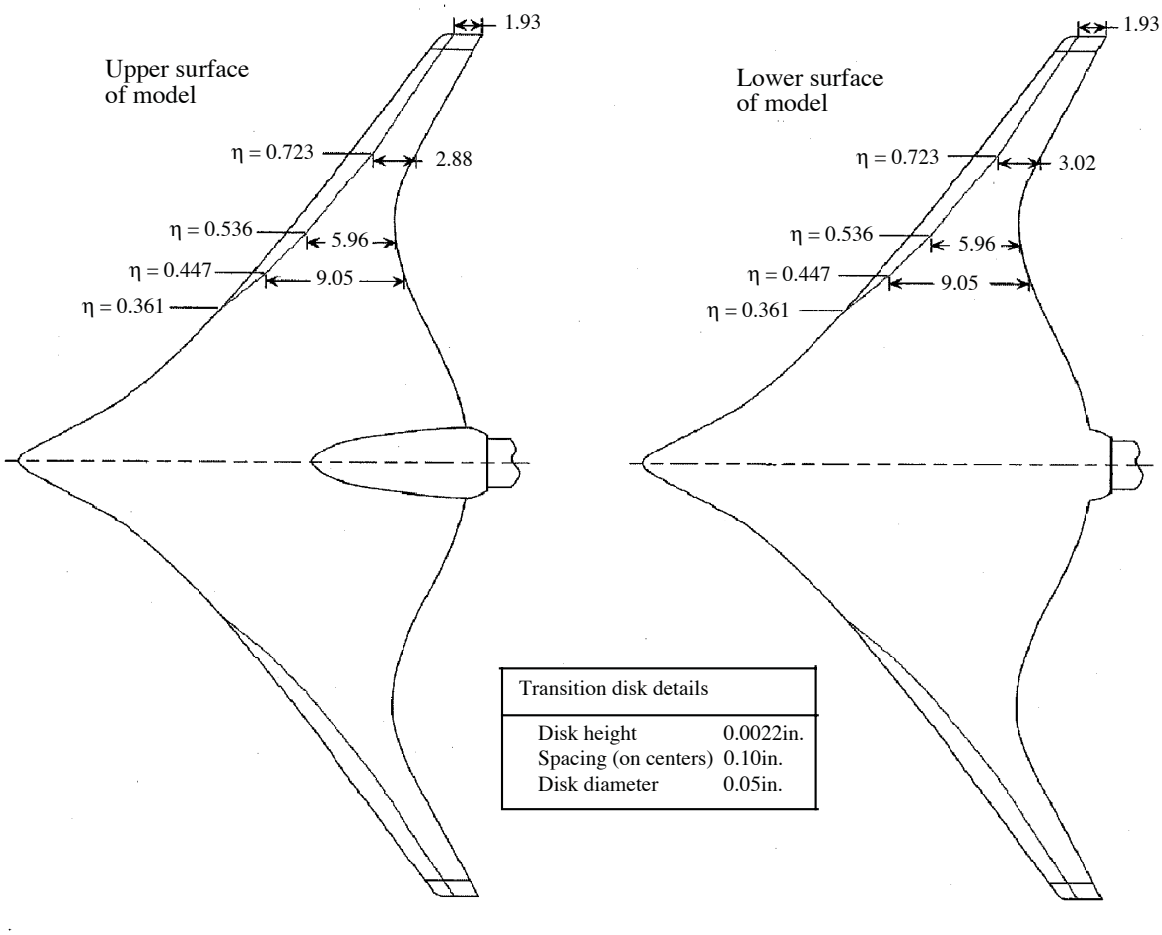

Figure 5. Details of artificial transition strips applied to the model for testing at $R_c = 3.5 \times 10^6$. (All dimensions are in inches unless otherwise indicated.)

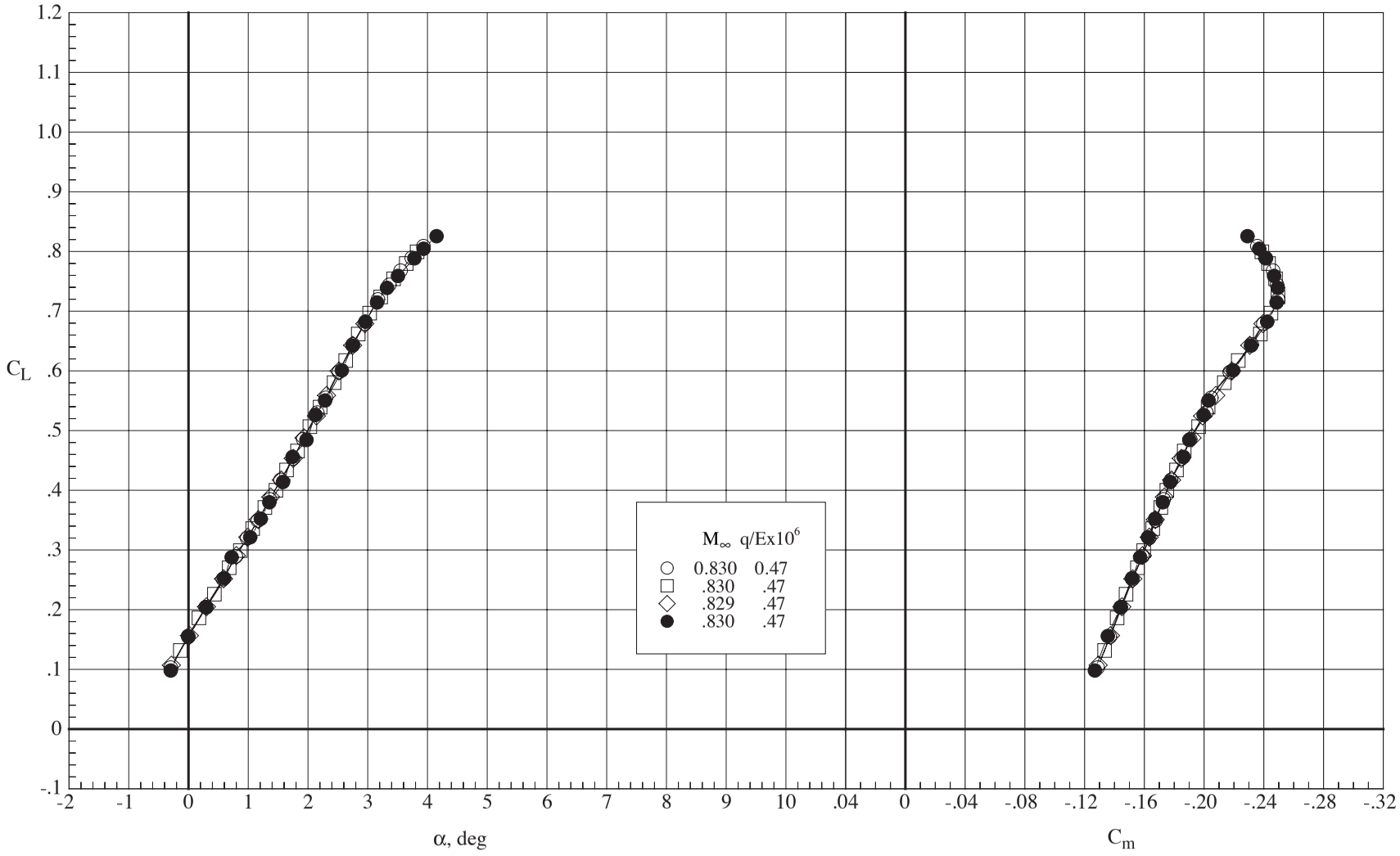

(a) Lift and pitching moment coefficients.

Figure 6. Longitudinal aerodynamic characteristics of the basic configuration with and without pressure tubes and wires crossing from the model to the sting. Reynolds number of 25.0 x 10^6 for Mach number 0.83. Solid symbols indicate instrumentation crossing from model to sting.

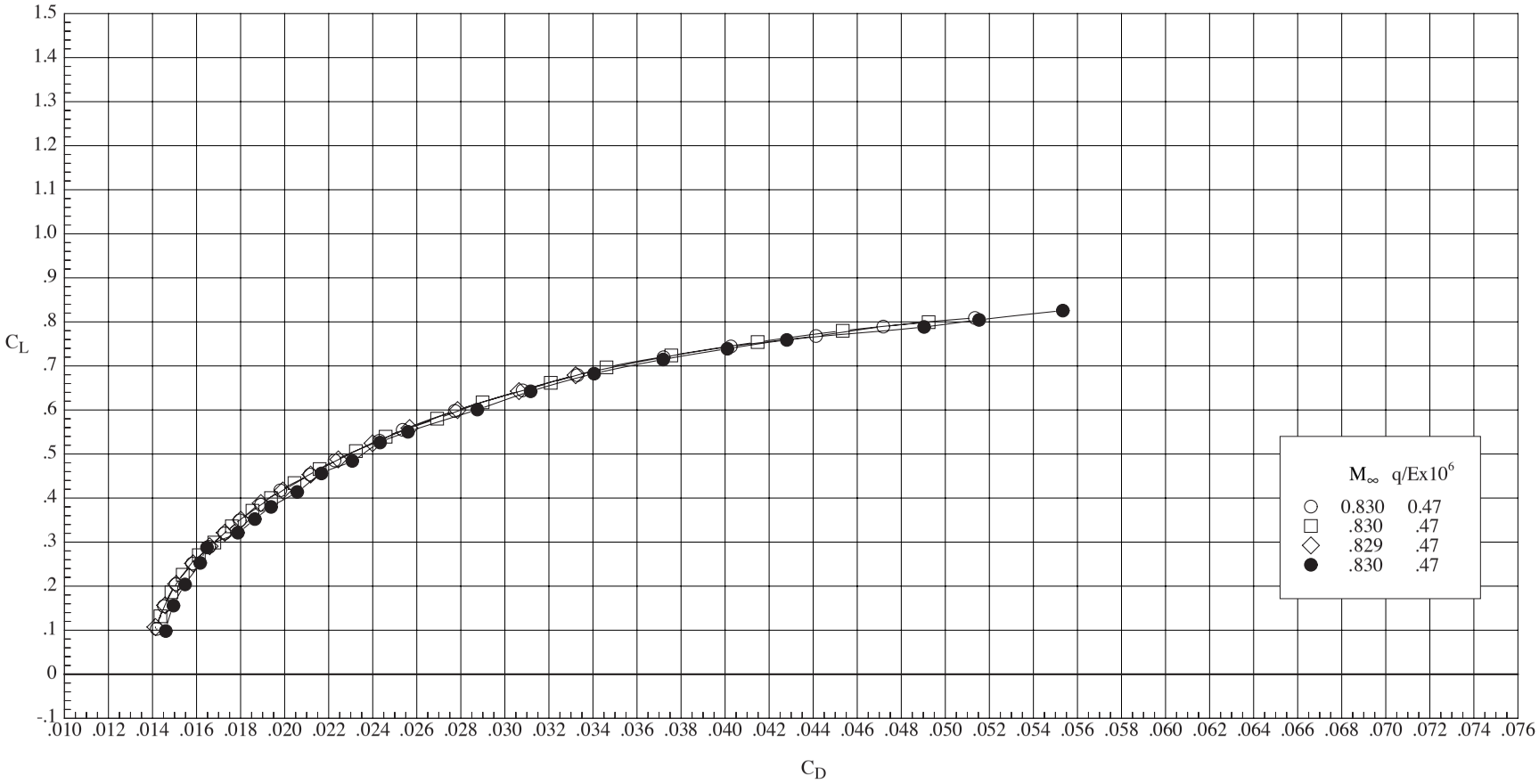

(b) Drag coefficient.

Figure 6. Concluded.

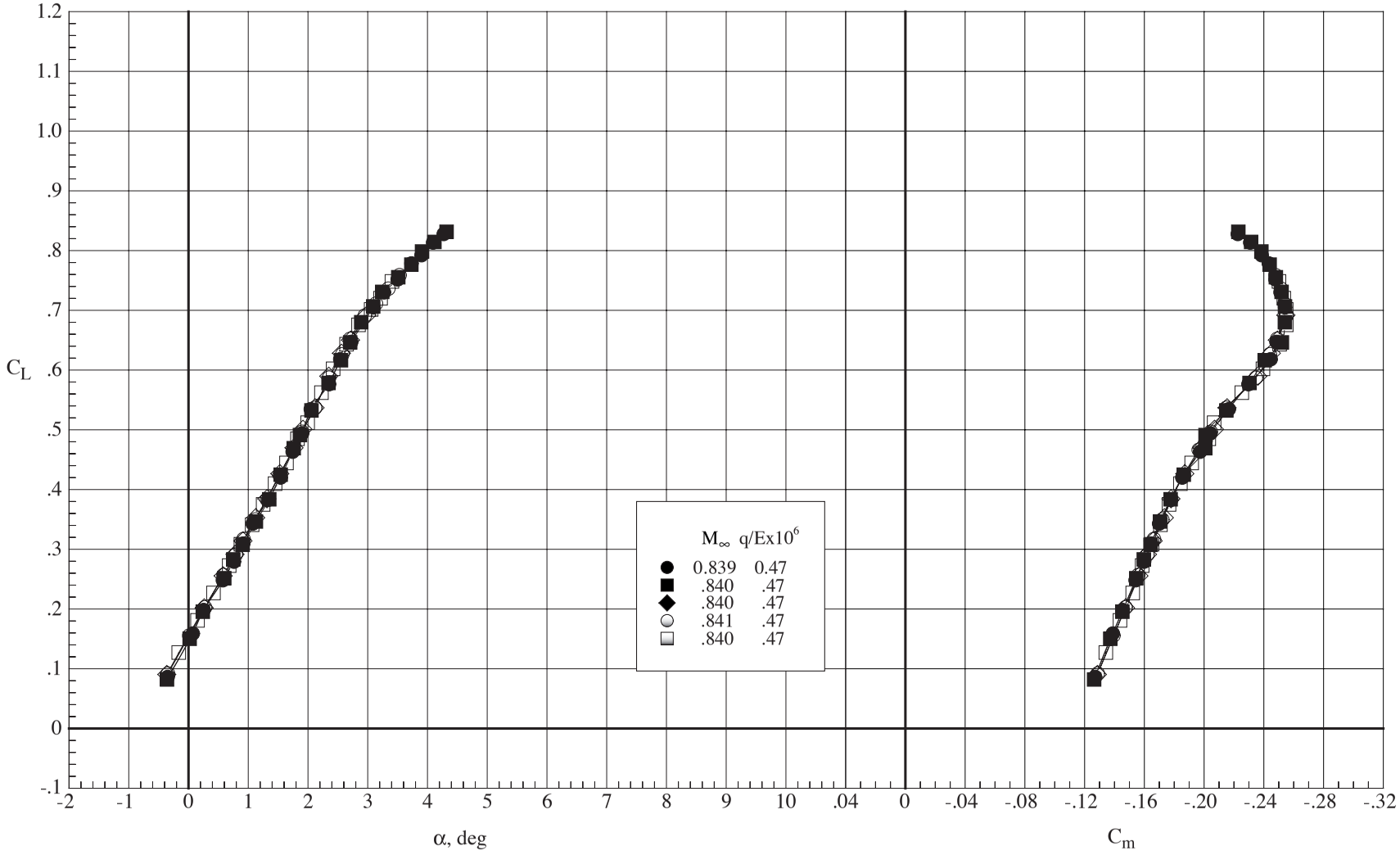

(a) Lift and pitching moment coefficients.

Figure 7. Longitudinal aerodynamic characteristics of the basic configuration with and without pressure tubes and wires crossing from the model to the sting. Reynolds number of 25.0 x 10^6 for Mach number 0.84. Solid symbols indicate instrumentation crossing from model to sting.

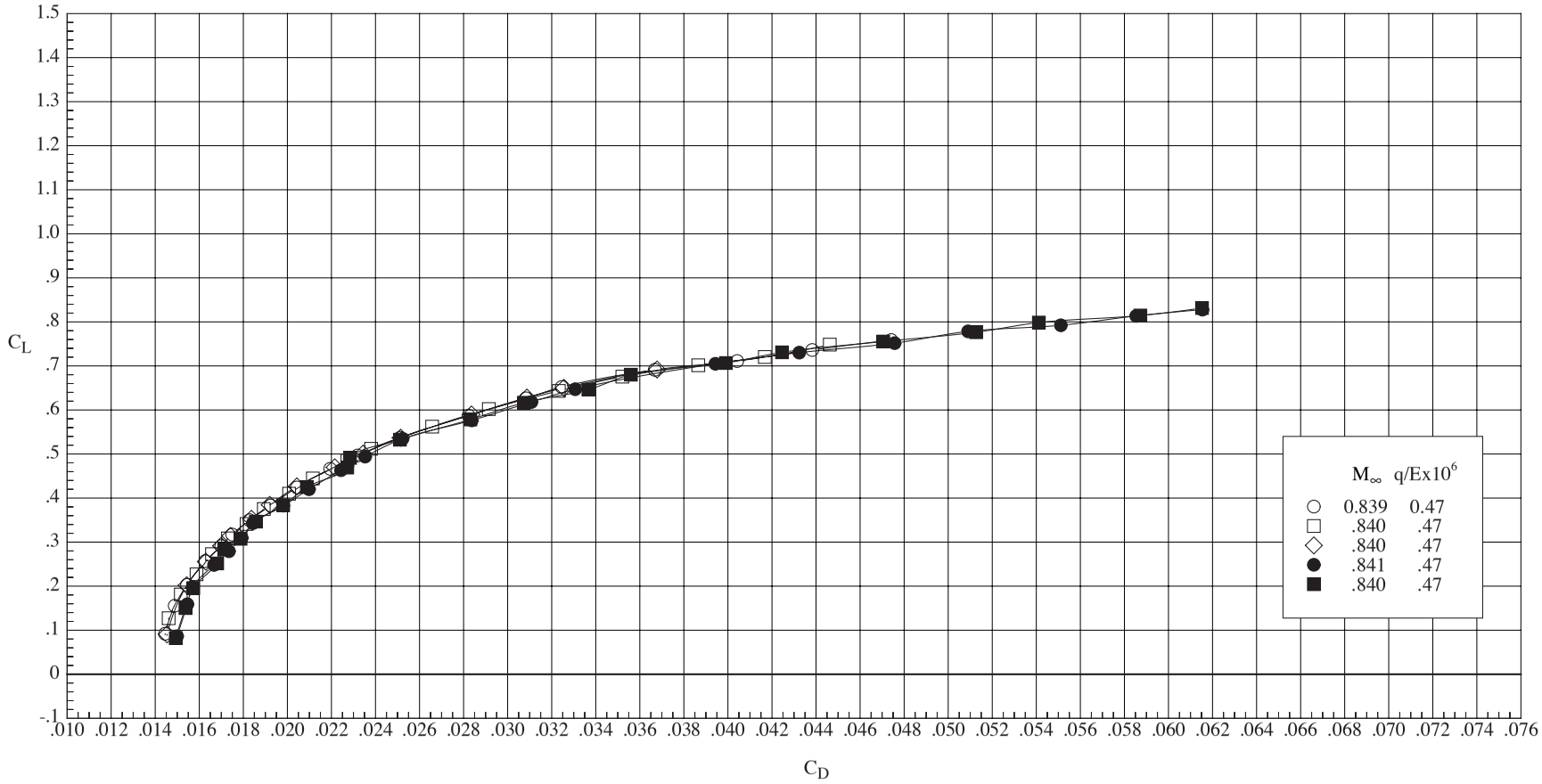

(b) Drag coefficient.

Figure 7. Concluded.

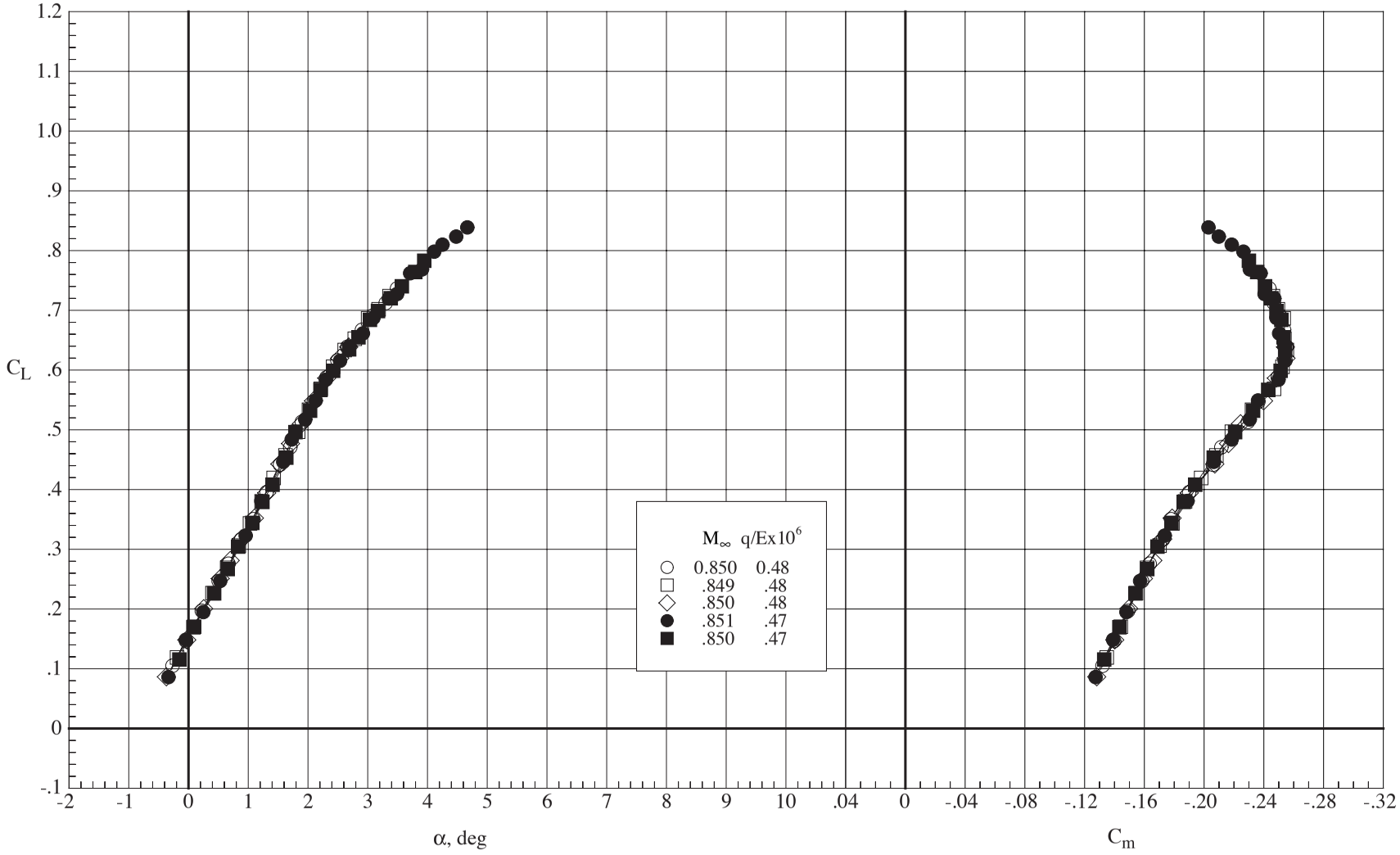

(a) Lift and pitching moment coefficients.

Figure 8. Longitudinal aerodynamic characteristics of the basic configuration with and without pressure tubes and wires crossing from the model to the sting. Reynolds number of 25.0 x 10^6 for Mach number 0.85. Solid symbols indicate instrumentation crossing from model to sting.

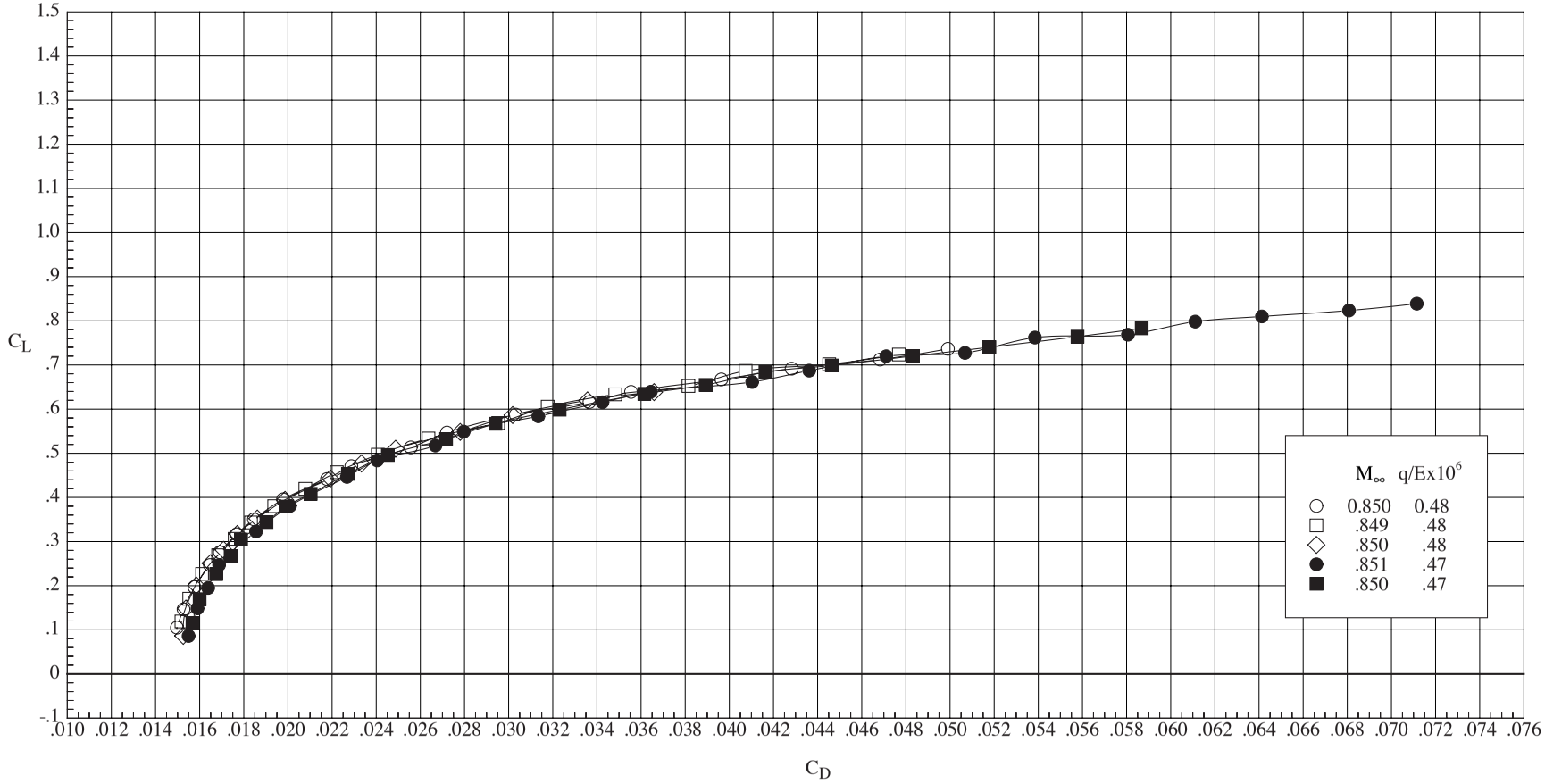

(b) Drag coefficient.

Figure 8. Concluded.

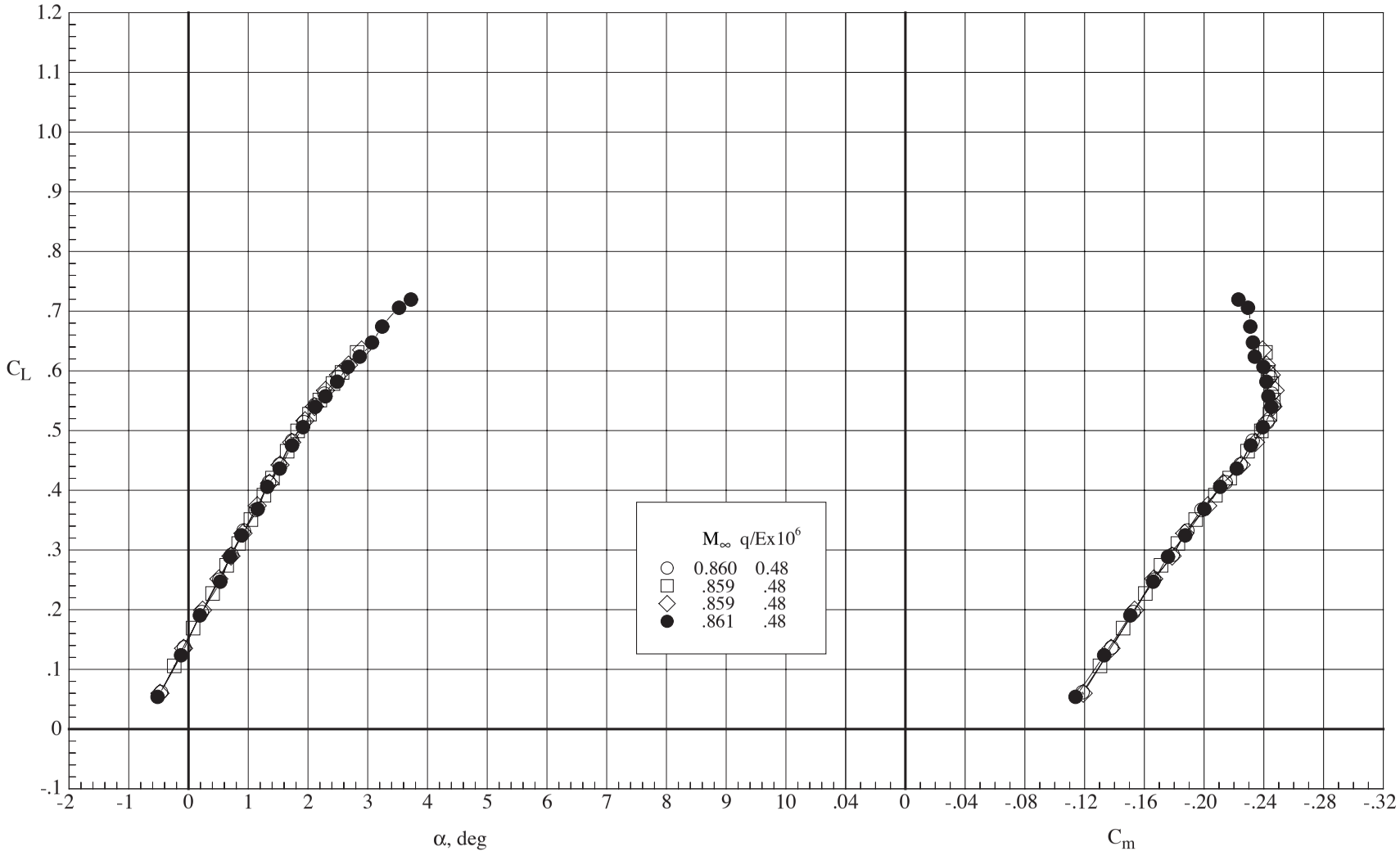

(a) Lift and pitching moment coefficients.

Figure 9. Longitudinal aerodynamic characteristics of the basic configuration with and without pressure tubes and wires crossing from the model to the sting. Reynolds number of 25.0 x 10^6 for Mach number 0.86. Solid symbols indicate instrumentation crossing from model to sting.

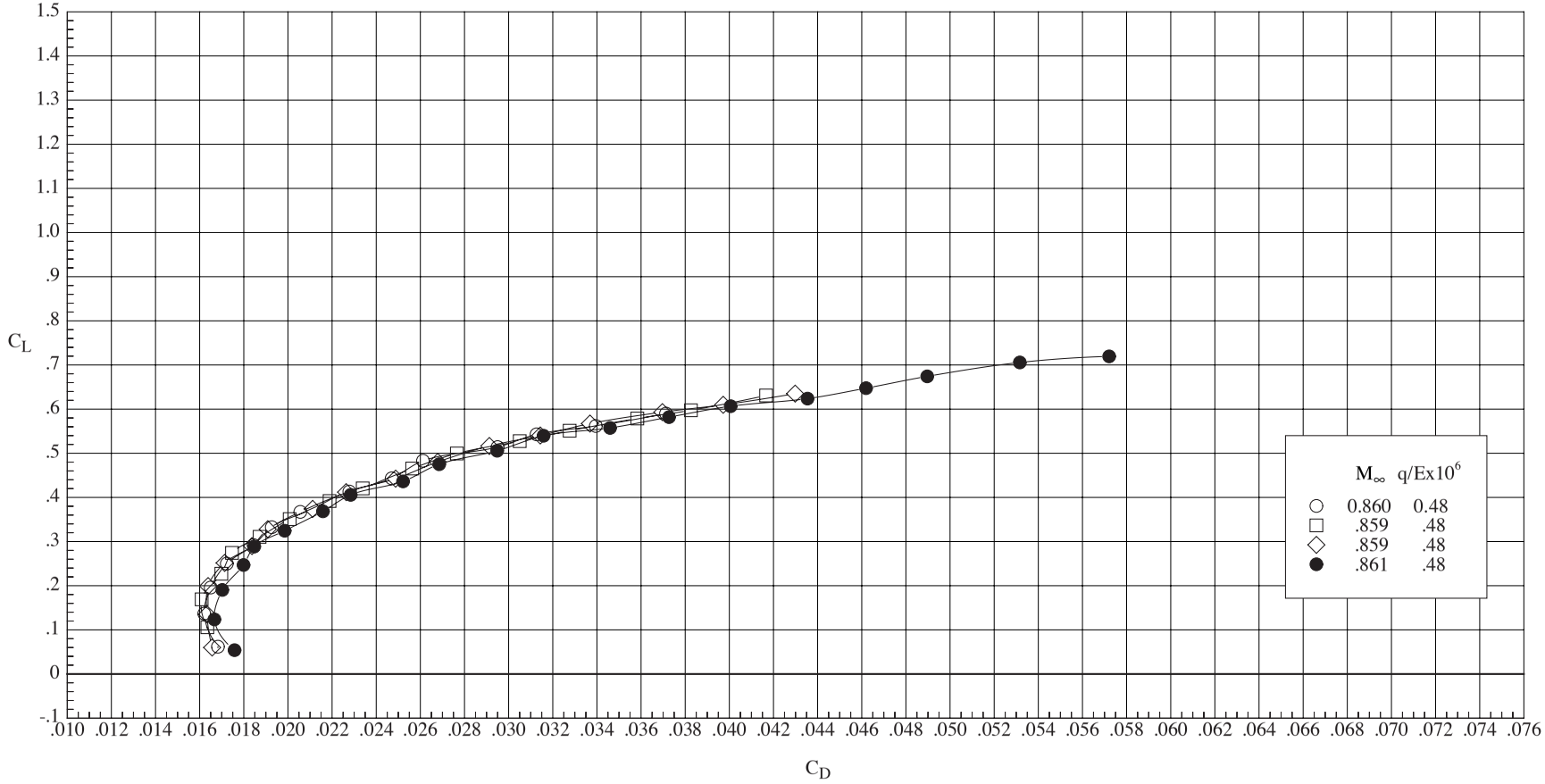

(b) Drag coefficient.

Figure 9. Concluded.

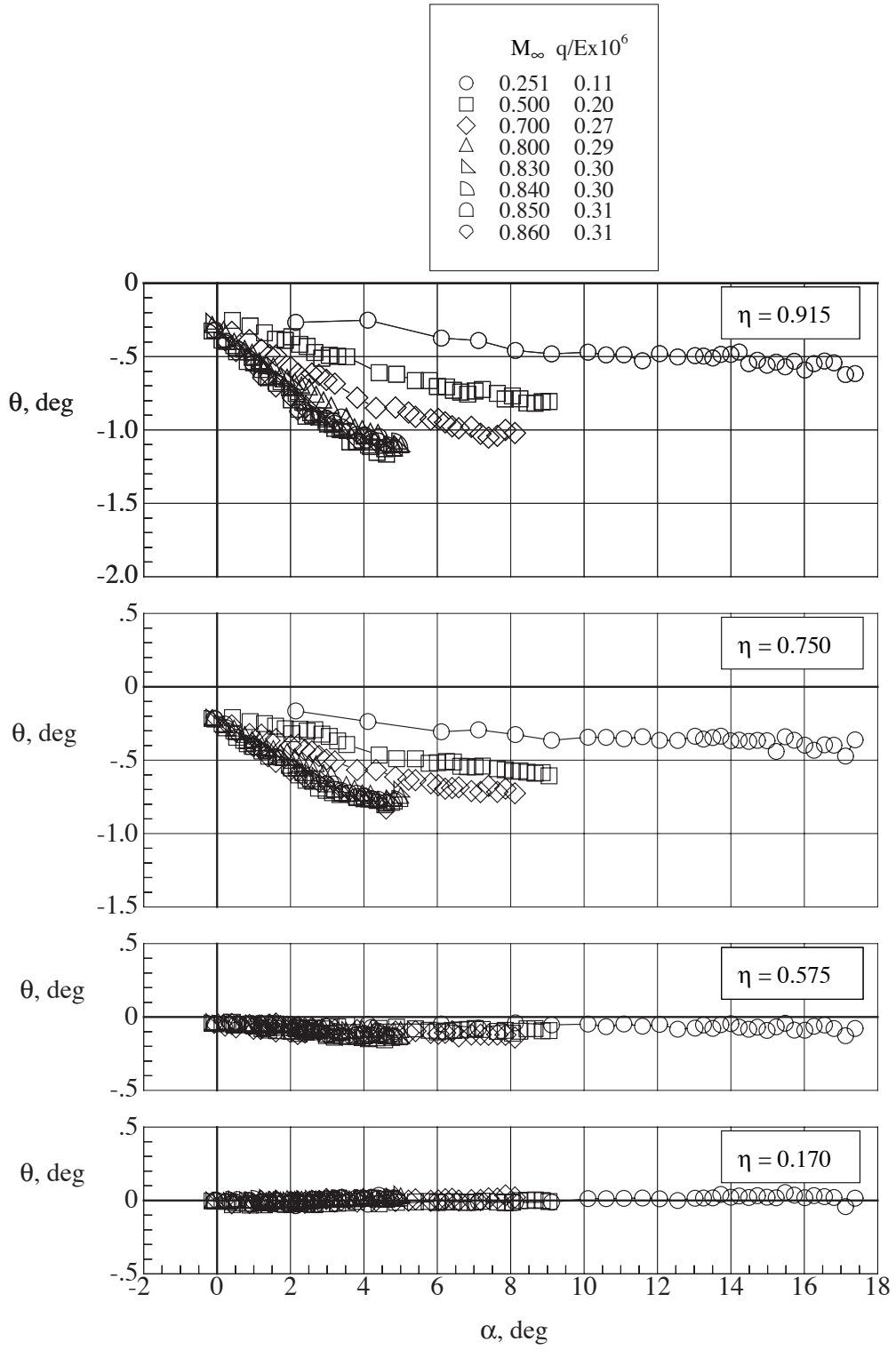

Figure 10. Measured wing twist at four spanwise stations on the basic configuration for a Reynolds number of 3.5 x 10^6.

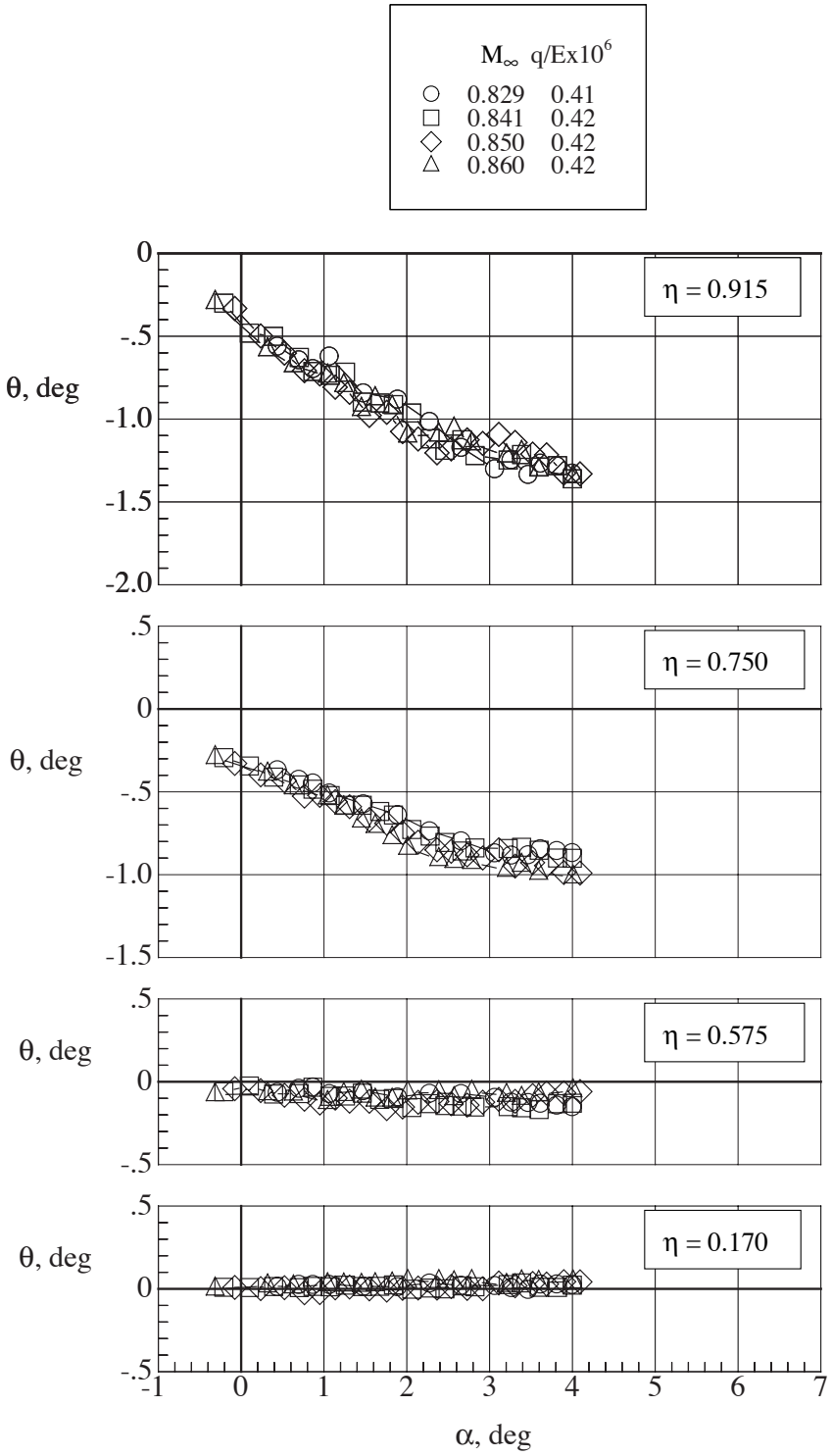

Figure 11. Measured wing twist at four spanwise stations on the basic configuration for a Reynolds number of 12.3 x 10^6.

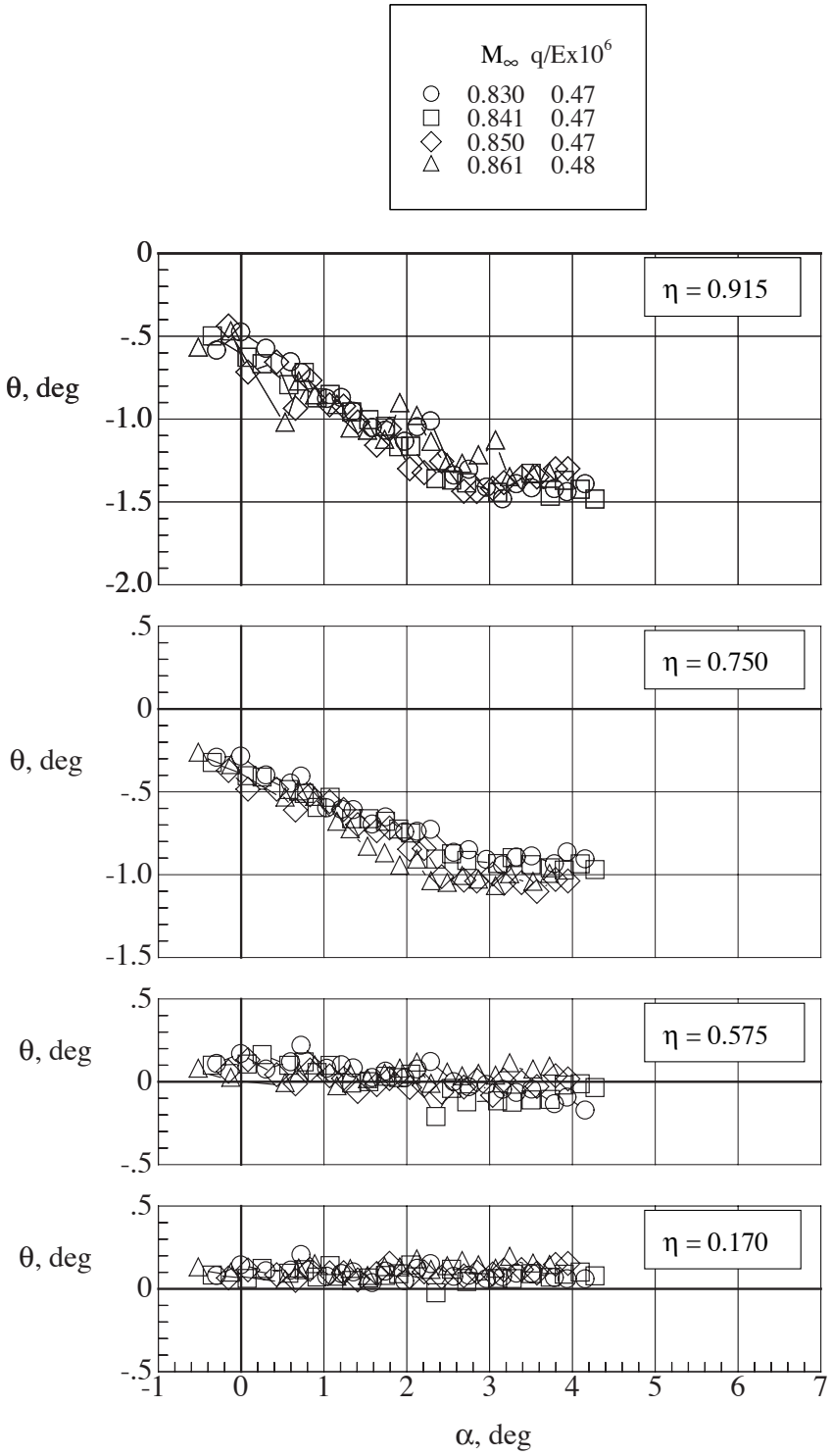

Figure 12. Measured wing twist at four spanwise stations on the basic configuration for a Reynolds number of 25.0 x 10^6.

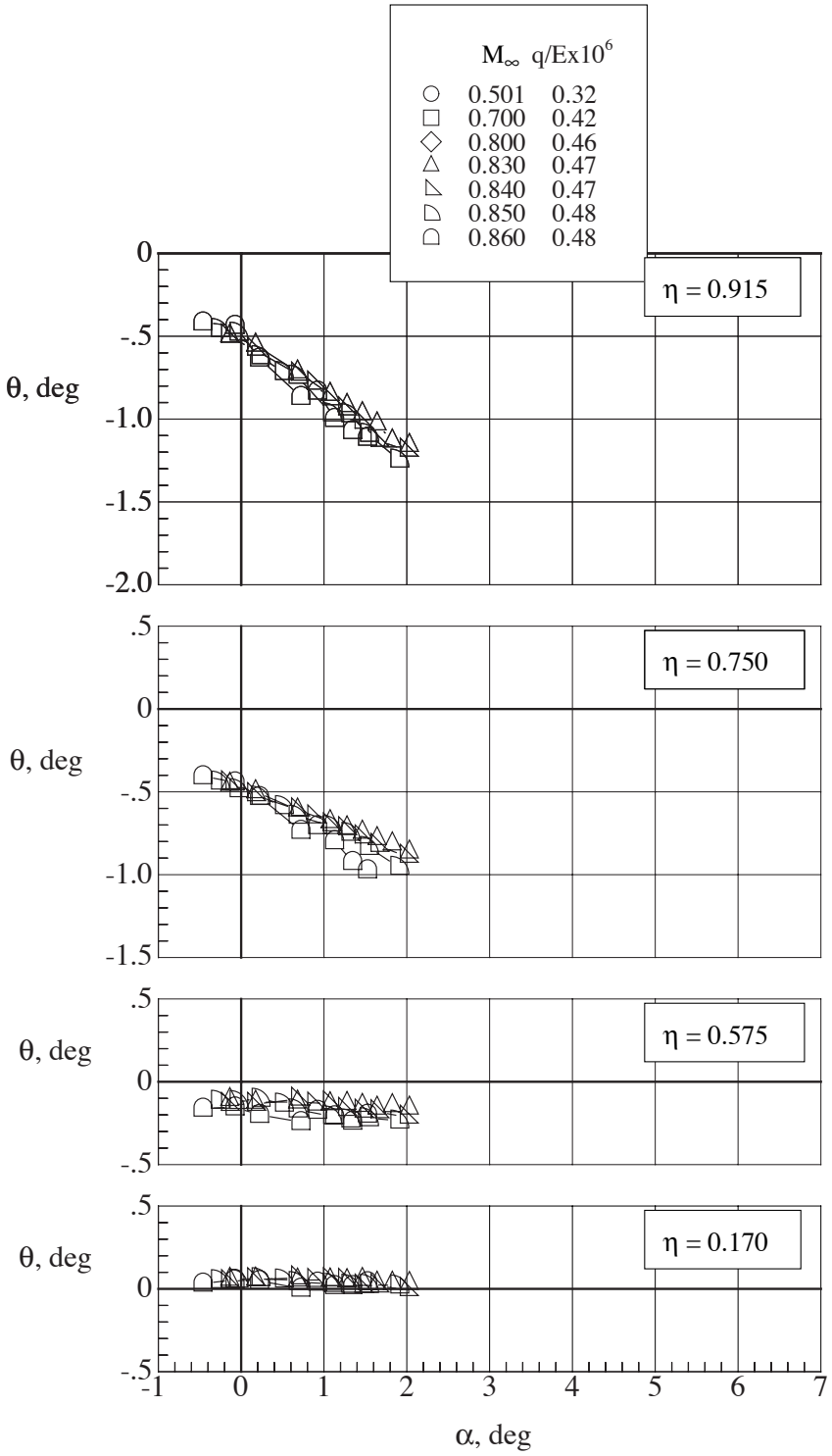

Figure 13. Measured wing twist at four spanwise stations on the basic configuration for a Reynolds number of 25.0 x 10^6. Tubes and wires disconnected.

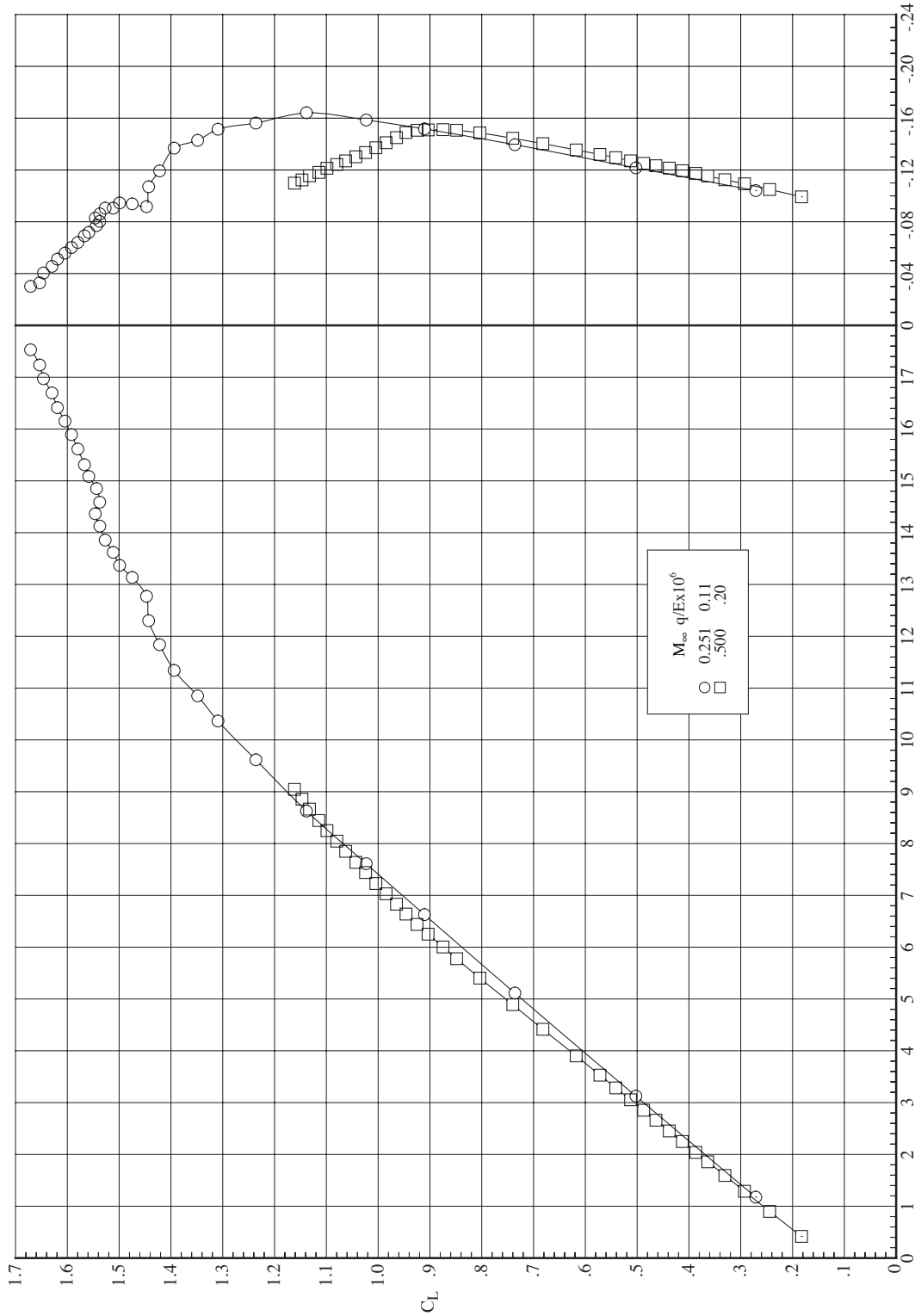

(a) Lift and pitching moment coefficients.

Figure 14. Longitudinal aerodynamic characteristics of the basic configuration at a Reynolds number of 3.5 x 10^6 for Mach numbers of 0.25 and 0.50. Fixed transition.

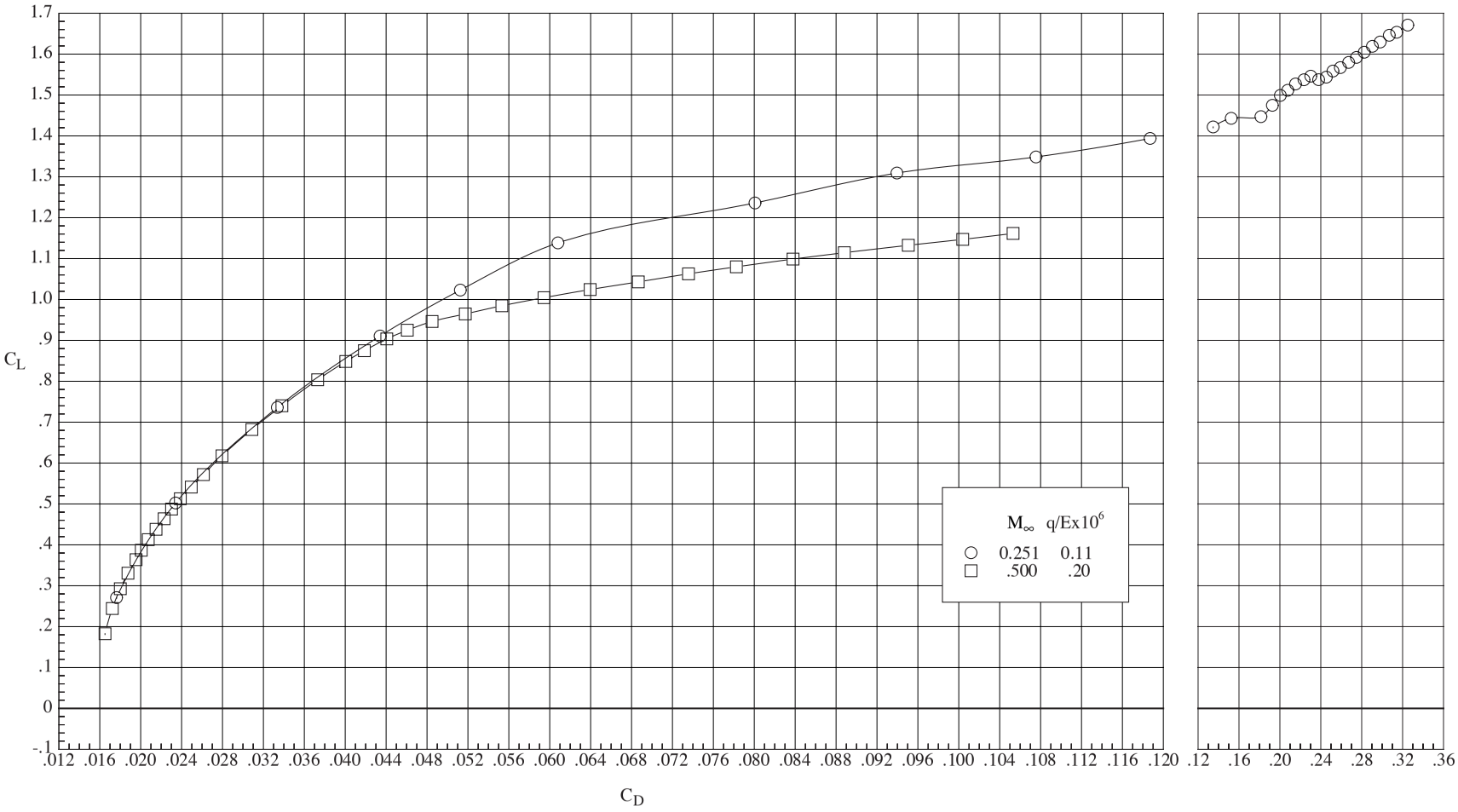

(b) Drag coefficient.

Figure 14. Concluded.

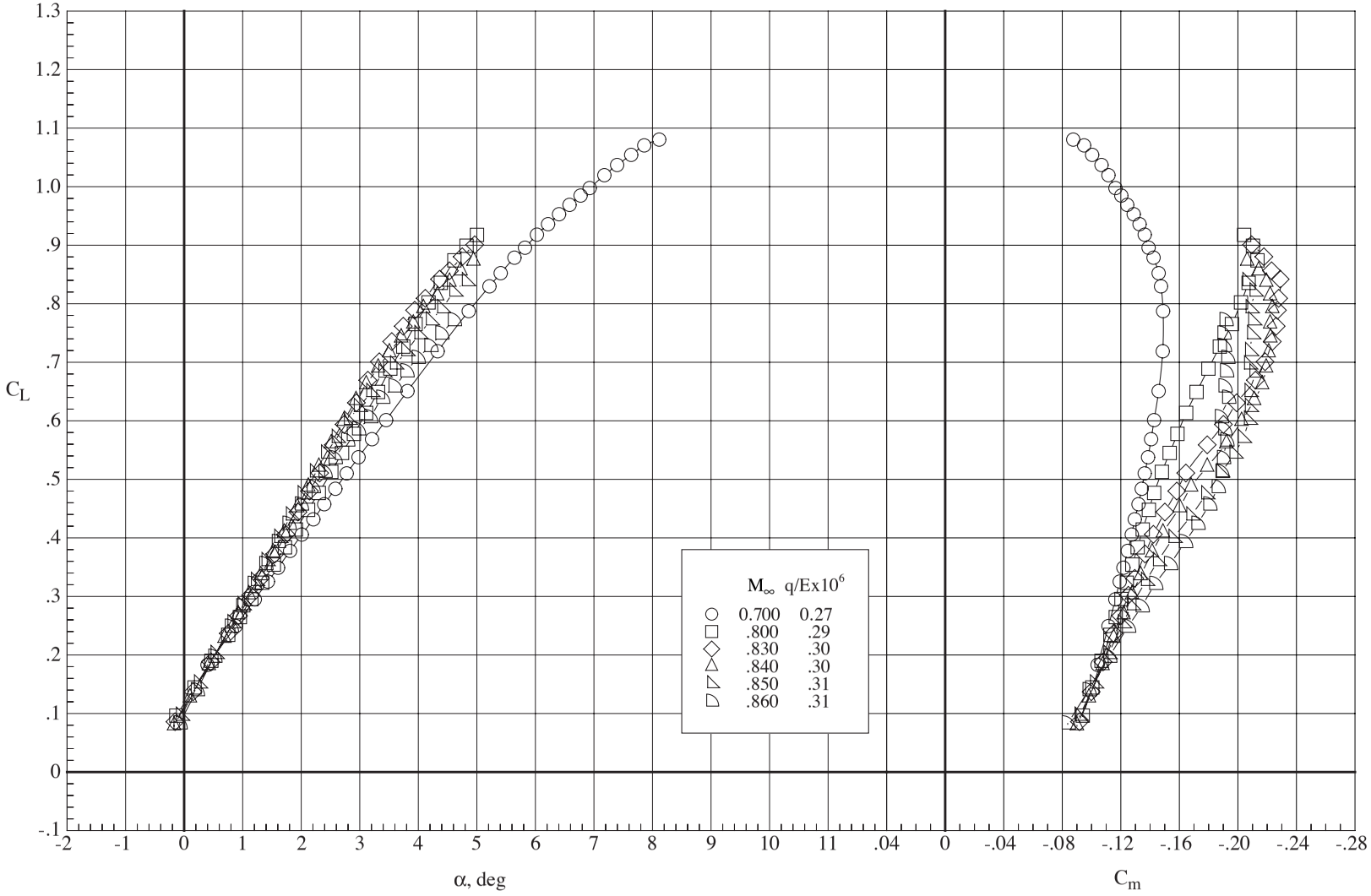

(a) Lift and pitching moment coefficients.

Figure 15. Longitudinal aerodynamic characteristics of the basic configuration at a Reynolds number of 3.5 x 10^6 for Mach numbers from 0.70 to 0.86. Fixed transition.

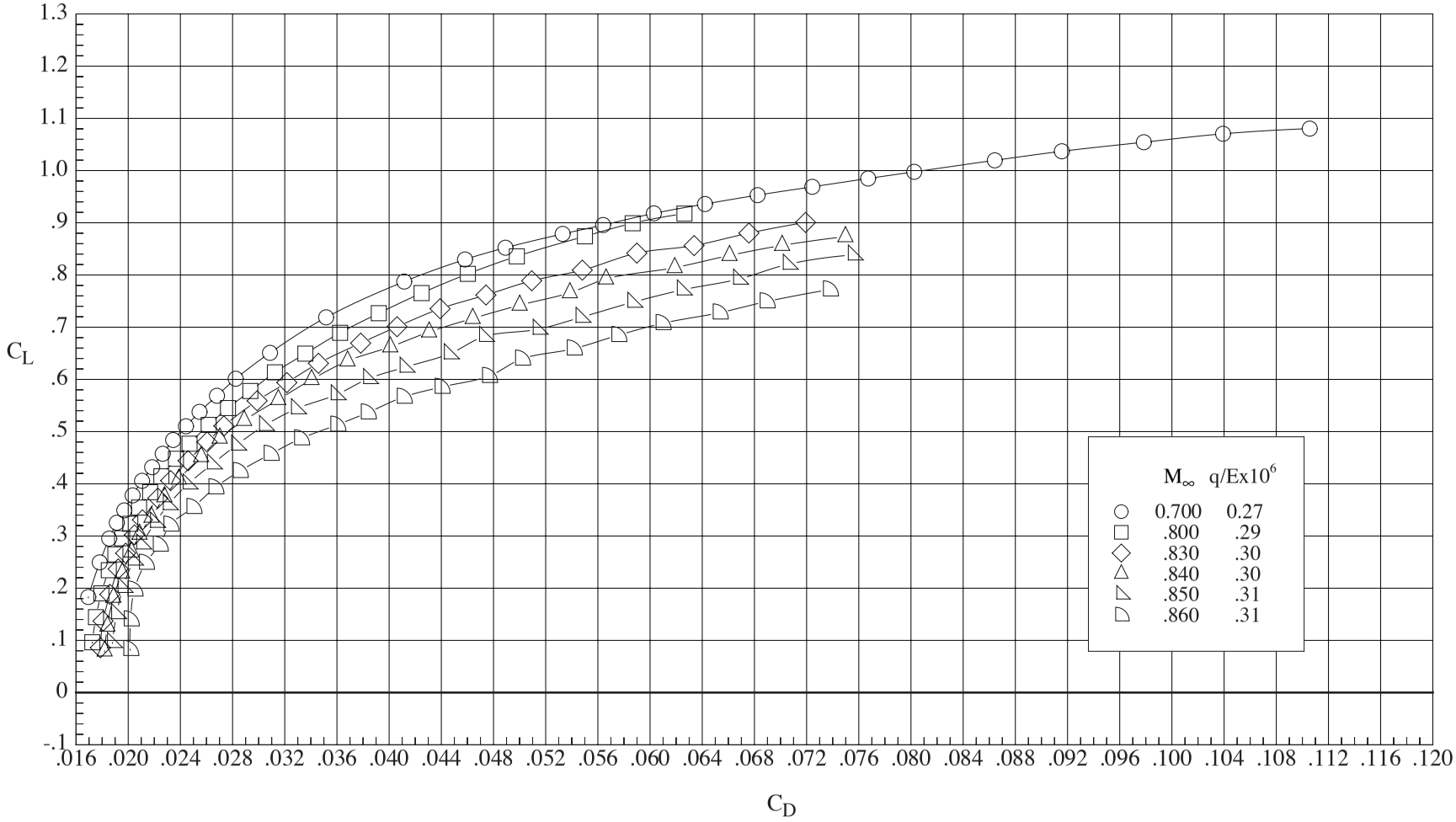

(b) Drag coefficient.

Figure 15. Concluded.

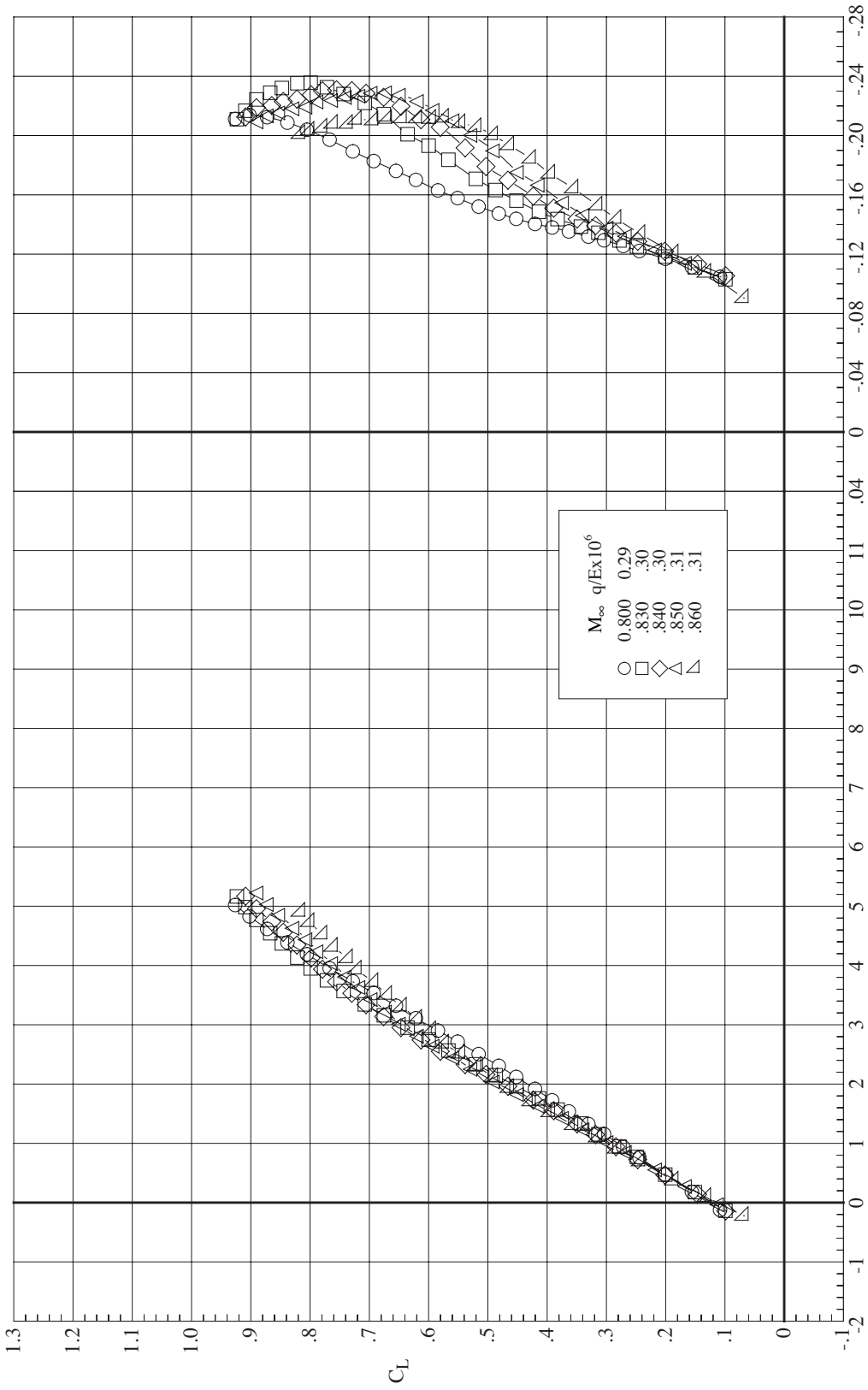

(a) Lift and pitching moment coefficients.

Figure 16. Longitudinal aerodynamic characteristics of the basic configuration at a Reynolds number of 3.5 x 10^6 for Mach numbers from 0.80 to 0.86. Free transition.

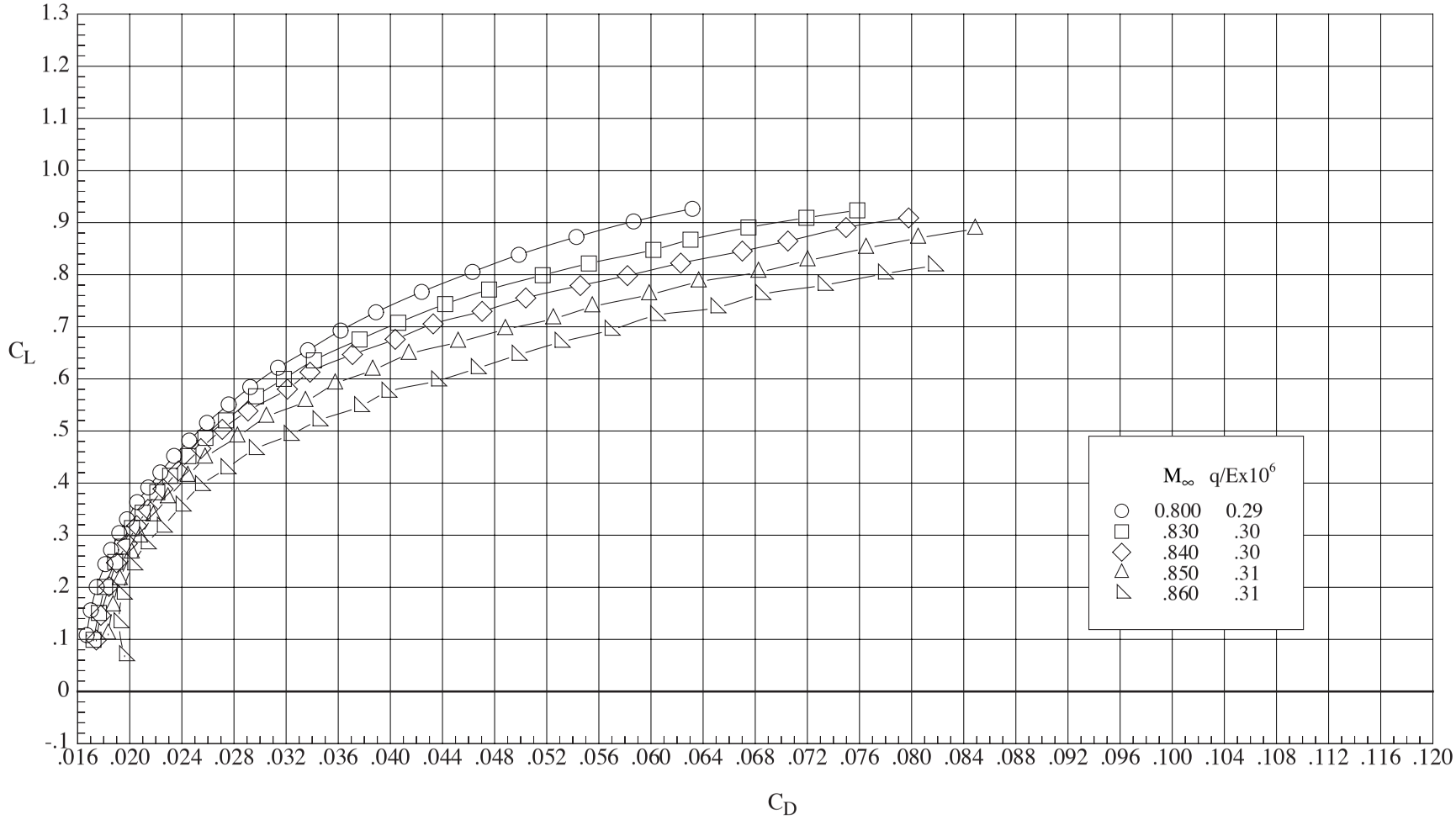

(b) Drag coefficient.

Figure 16. Concluded.

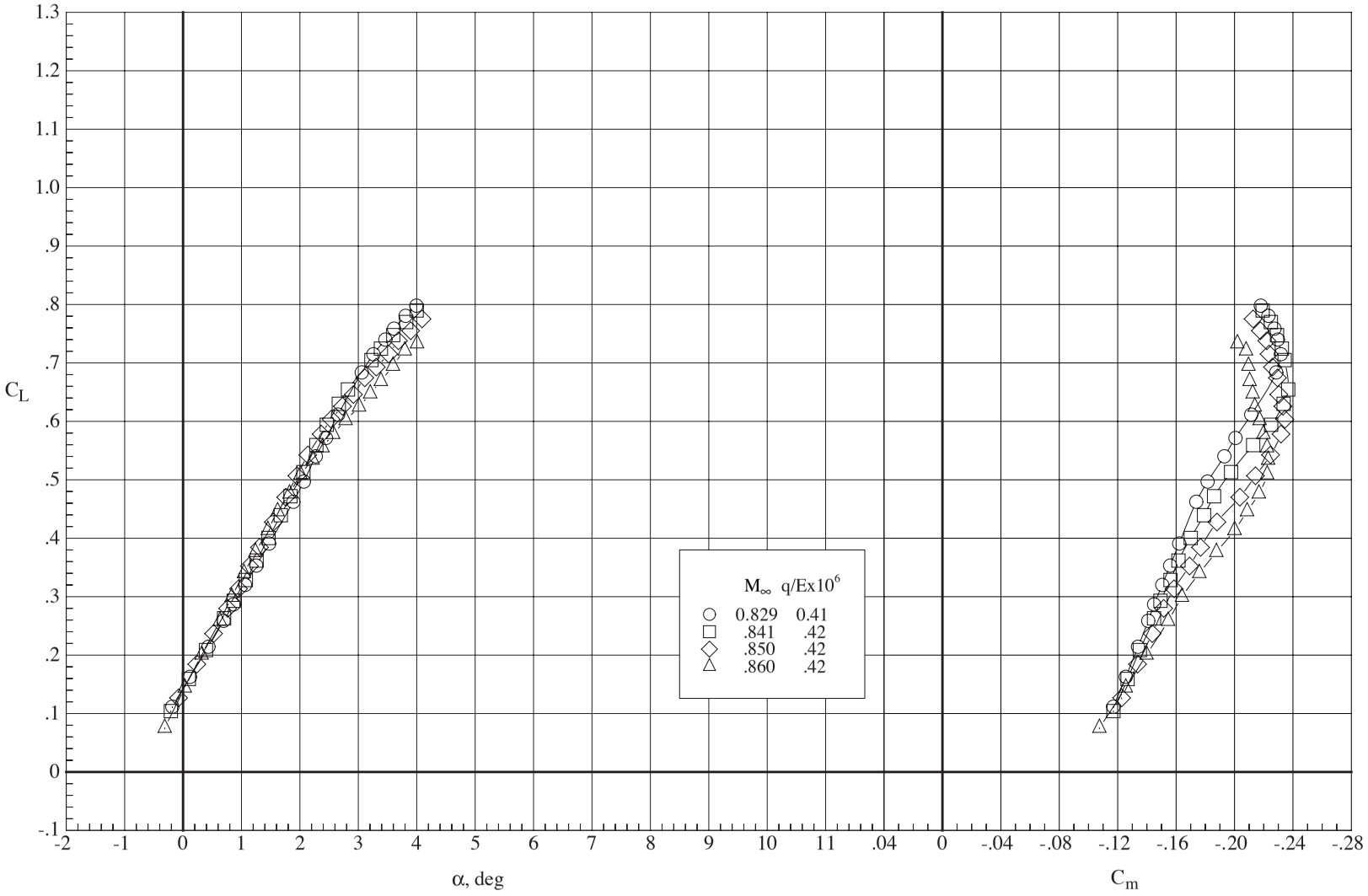

(a) Lift and pitching moment coefficients.

Figure 17. Longitudinal aerodynamic characteristics of the basic configuration at a Reynolds number of 12.3 x 10^6 for Mach numbers from 0.83 to 0.86.

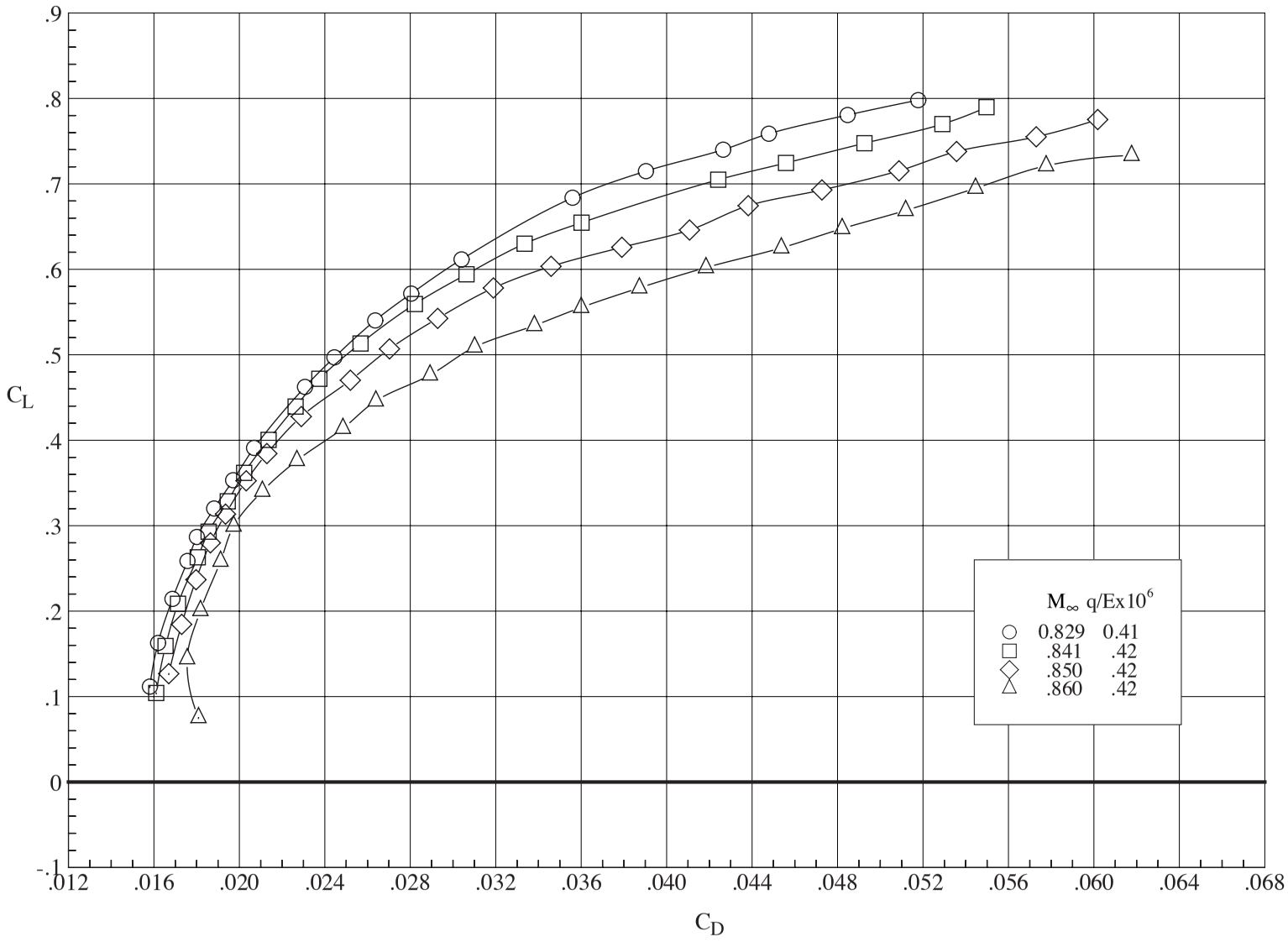

(b) Drag coefficient.

Figure 17. Concluded.

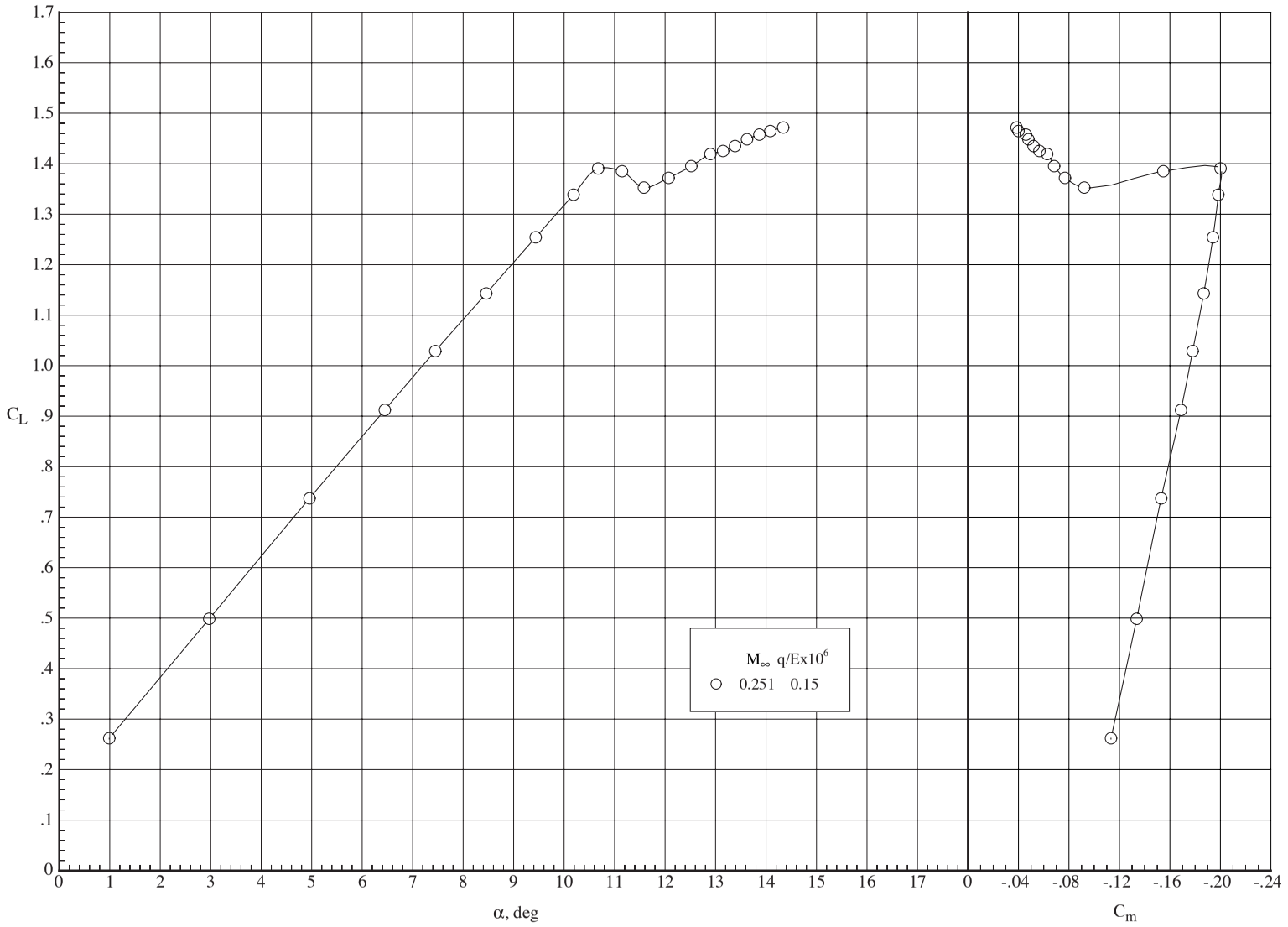

(a) Lift and pitching moment coefficients.

Figure 18. Longitudinal aerodynamic characteristics of the basic configuration at a Reynolds number of 21.5 x 10^6 for a Mach number of 0.25.

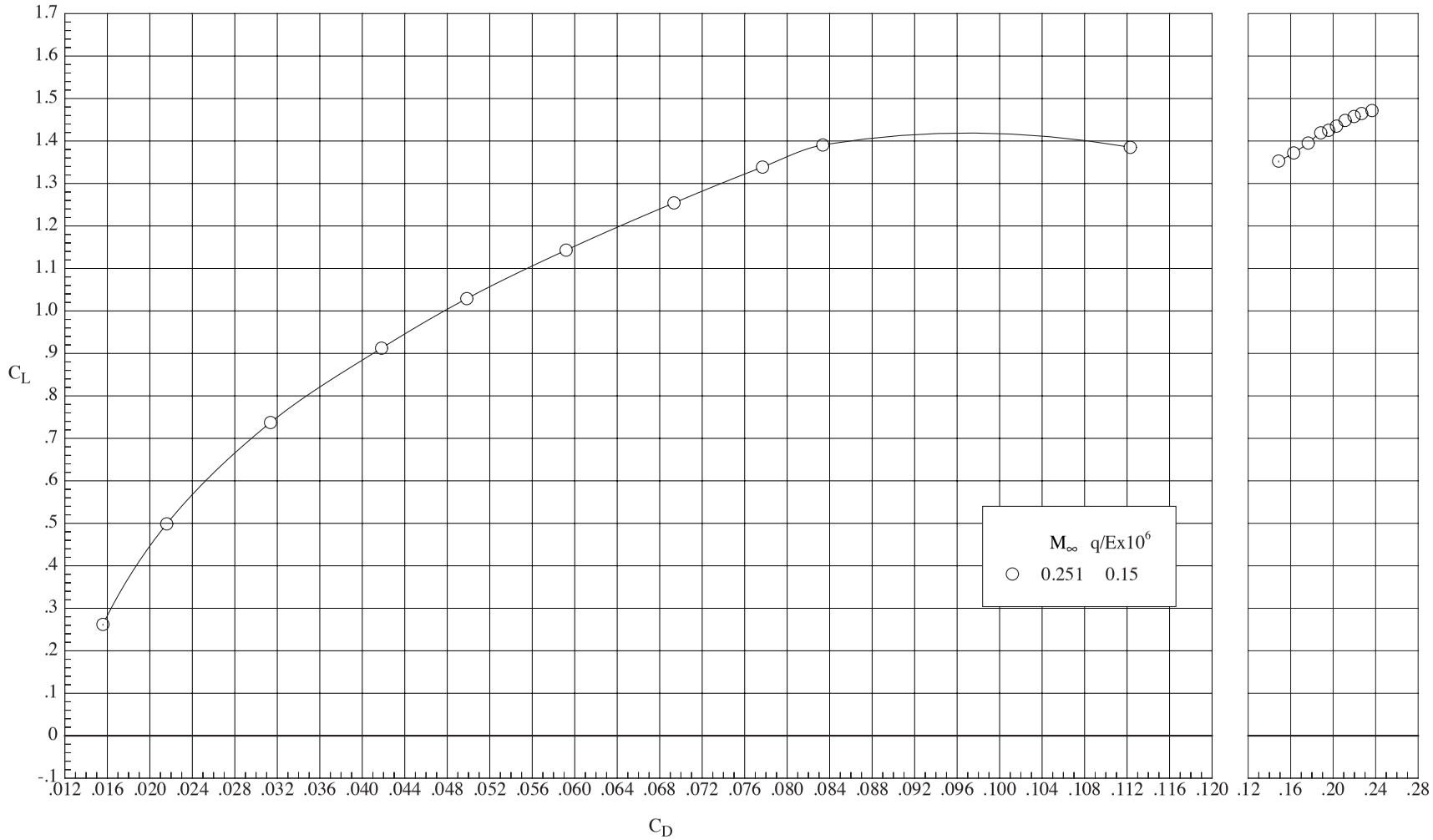

(b) Drag coefficient.

Figure 18. Concluded.

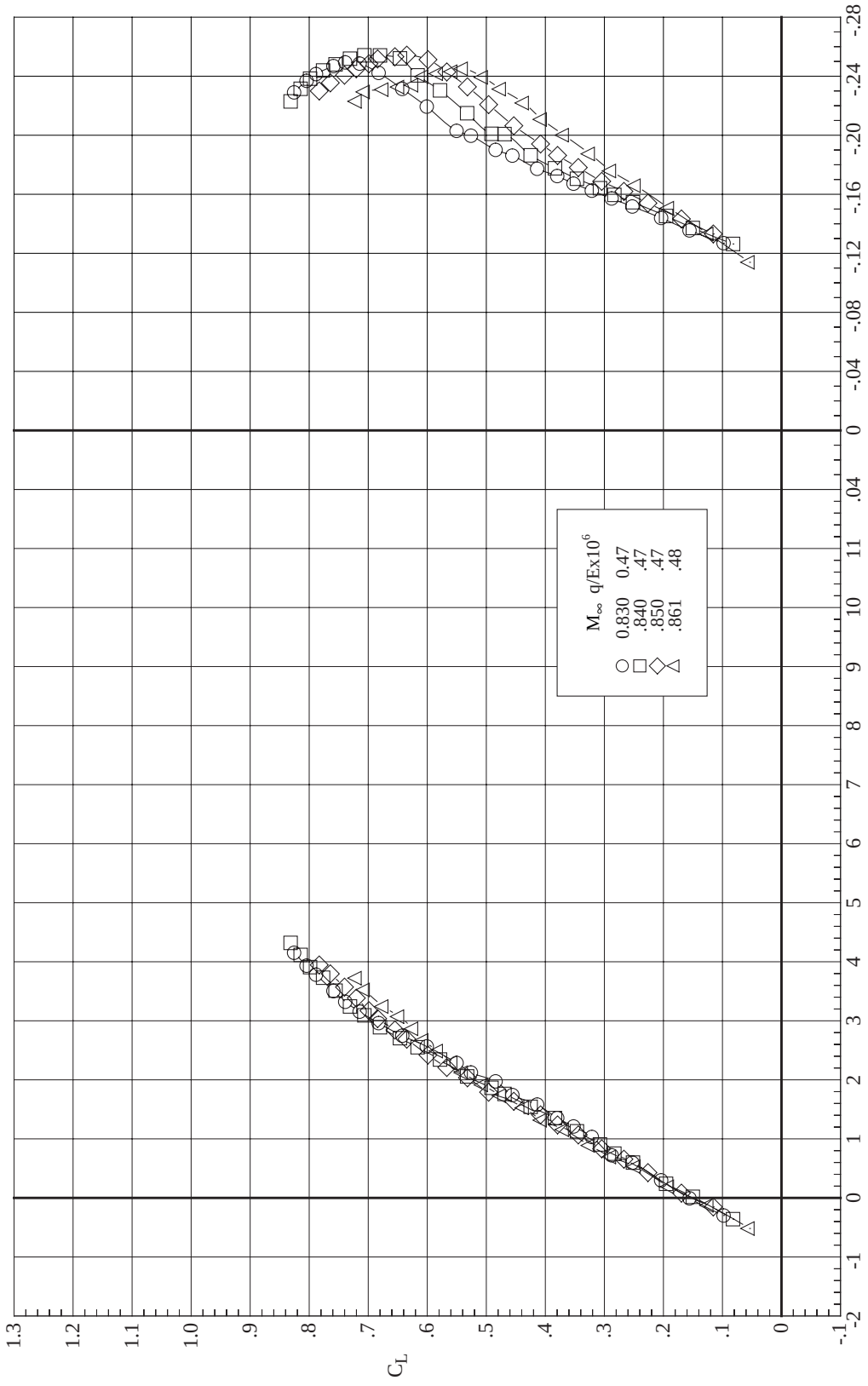

(a) Lift and pitching moment coefficients.

Figure 19. Longitudinal aerodynamic characteristics of the basic configuration at a Reynolds number of 25.0 x 10^6 for Mach numbers from 0.83 to 0.86.

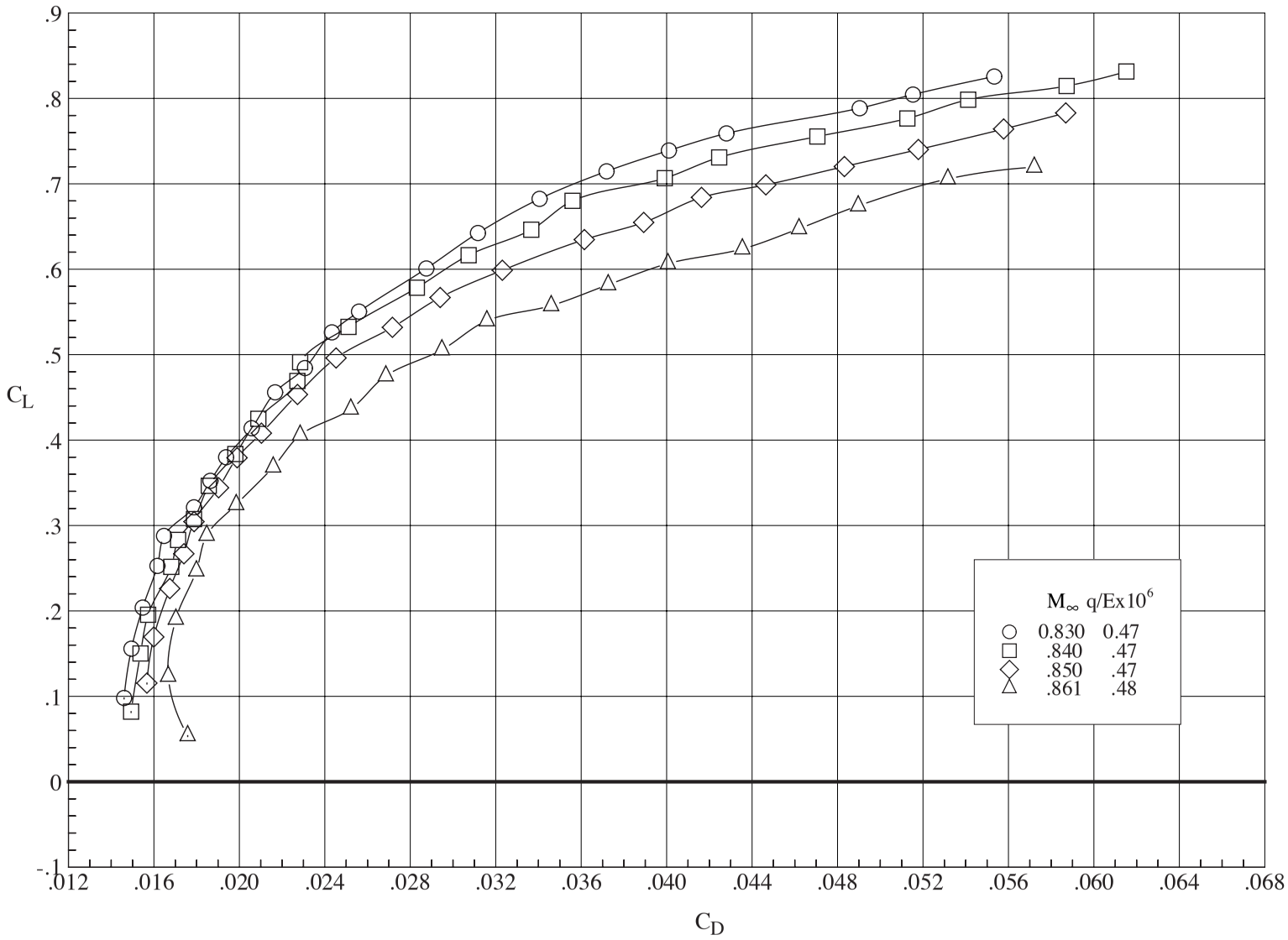

(b) Drag coefficient.

Figure 19. Concluded.

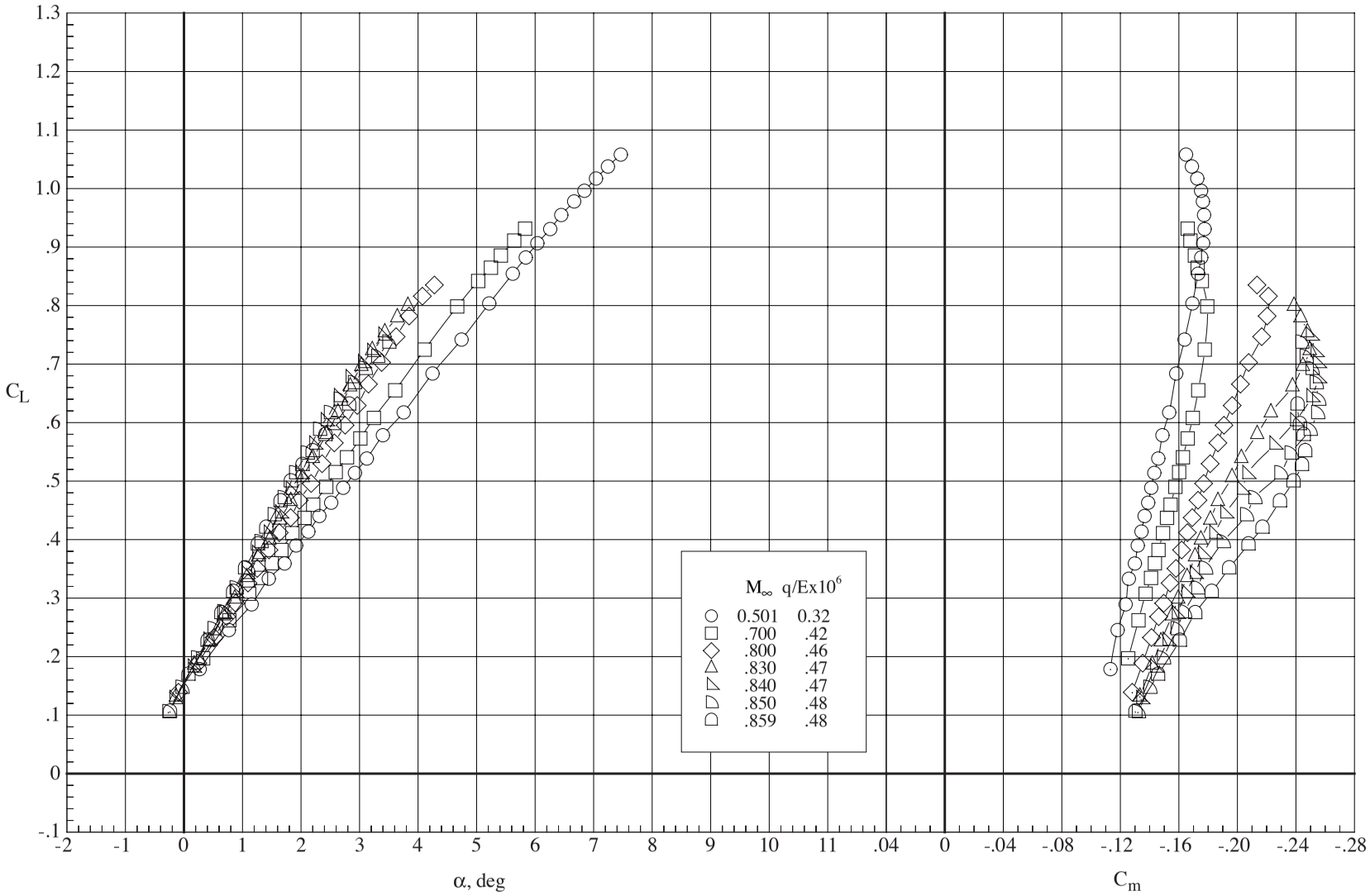

(a) Lift and pitching moment coefficients.

Figure 20. Longitudinal aerodynamic characteristics of the basic configuration at a Reynolds number of 25.0 x 10^6 for Mach numbers from 0.50 to 0.86. Tubes and wires disconnected.

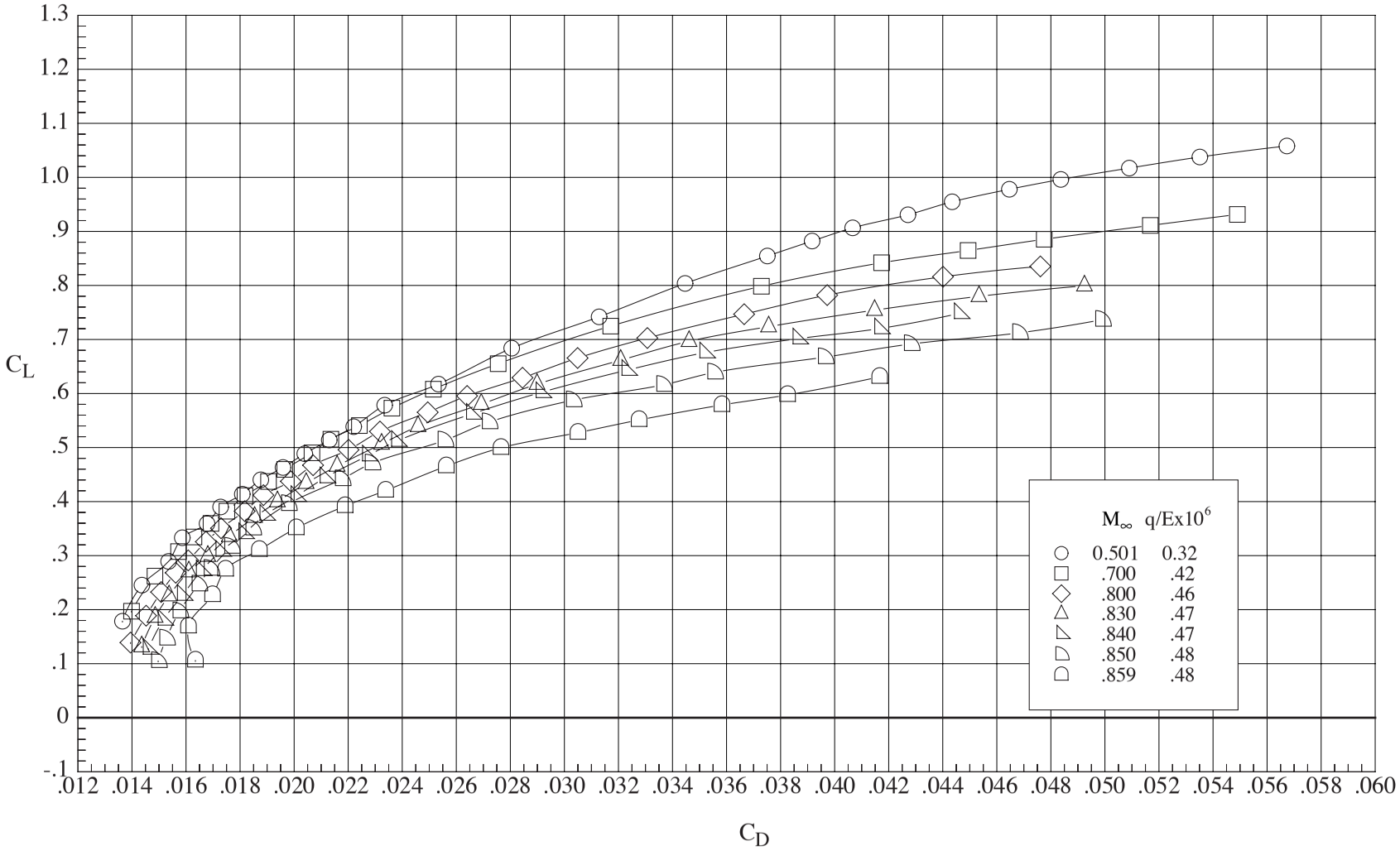

(b) Drag coefficient.

Figure 20. Concluded.

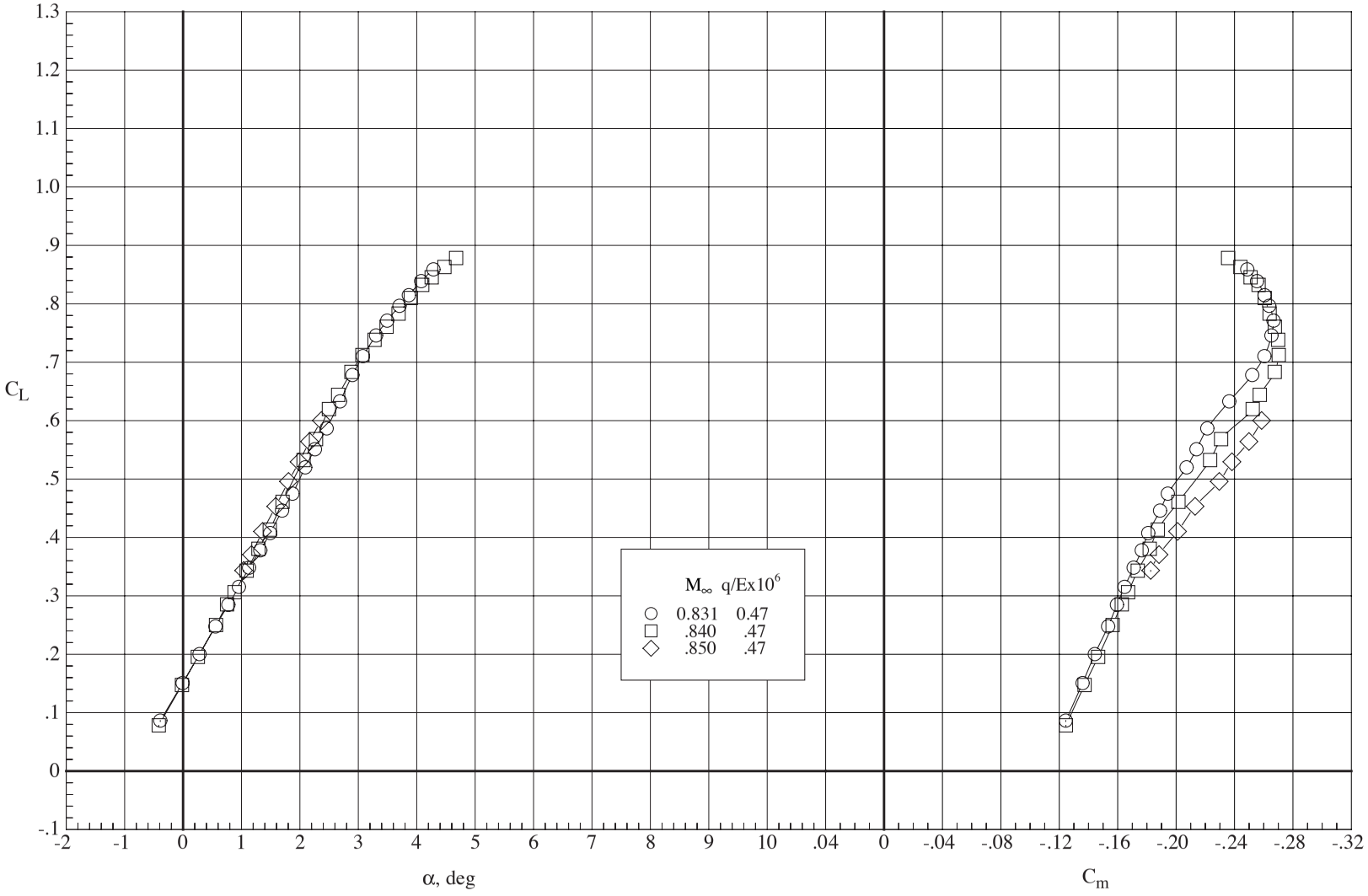

(a) Lift and pitching moment coefficients.

Figure 21. Longitudinal aerodynamic characteristics of the configuration with winglets at a Reynolds number of 25.0 x 10^6 for Mach numbers from 0.83 to 0.85.

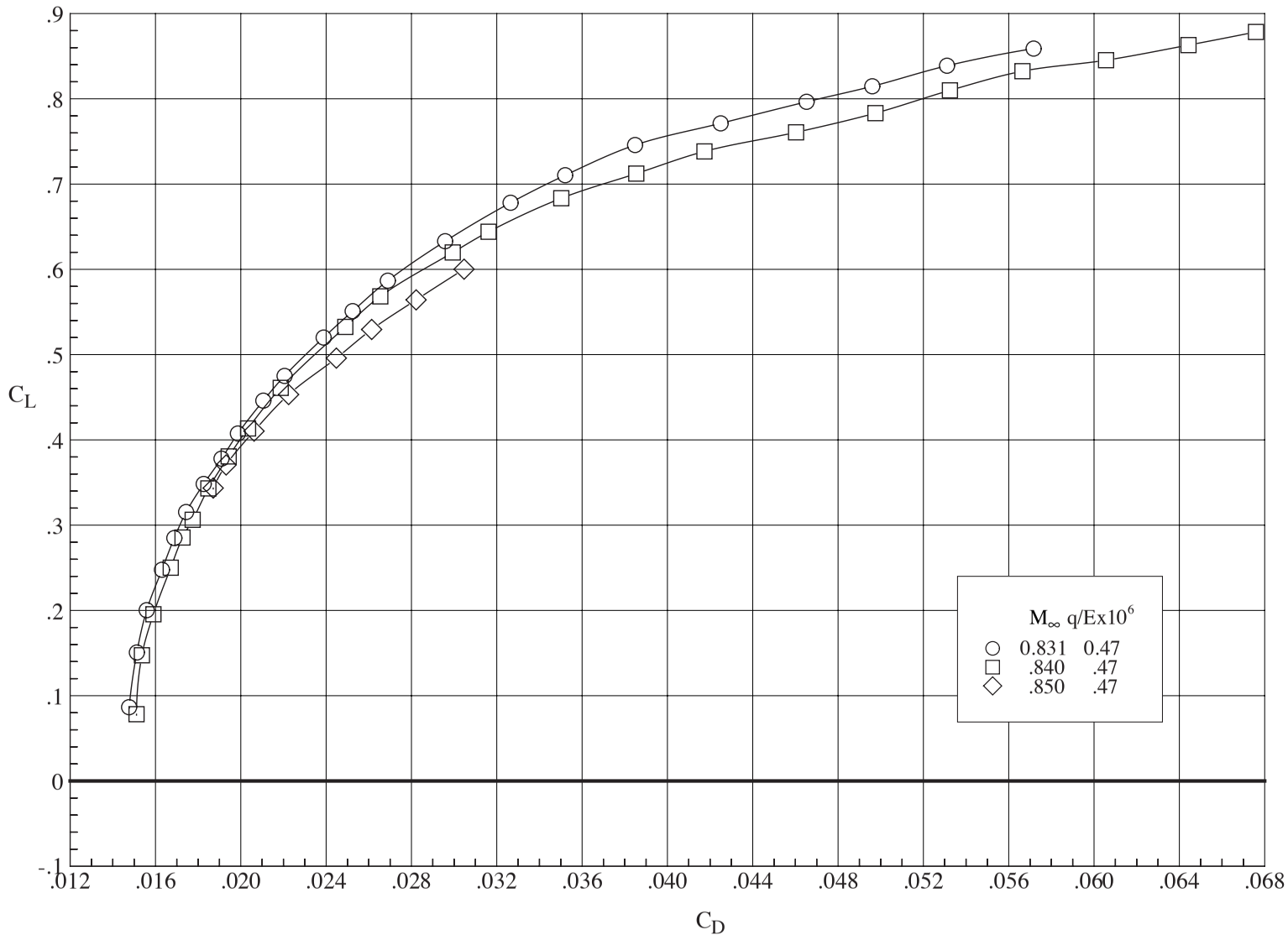

(b) Drag coefficient.

Figure 21. Concluded.

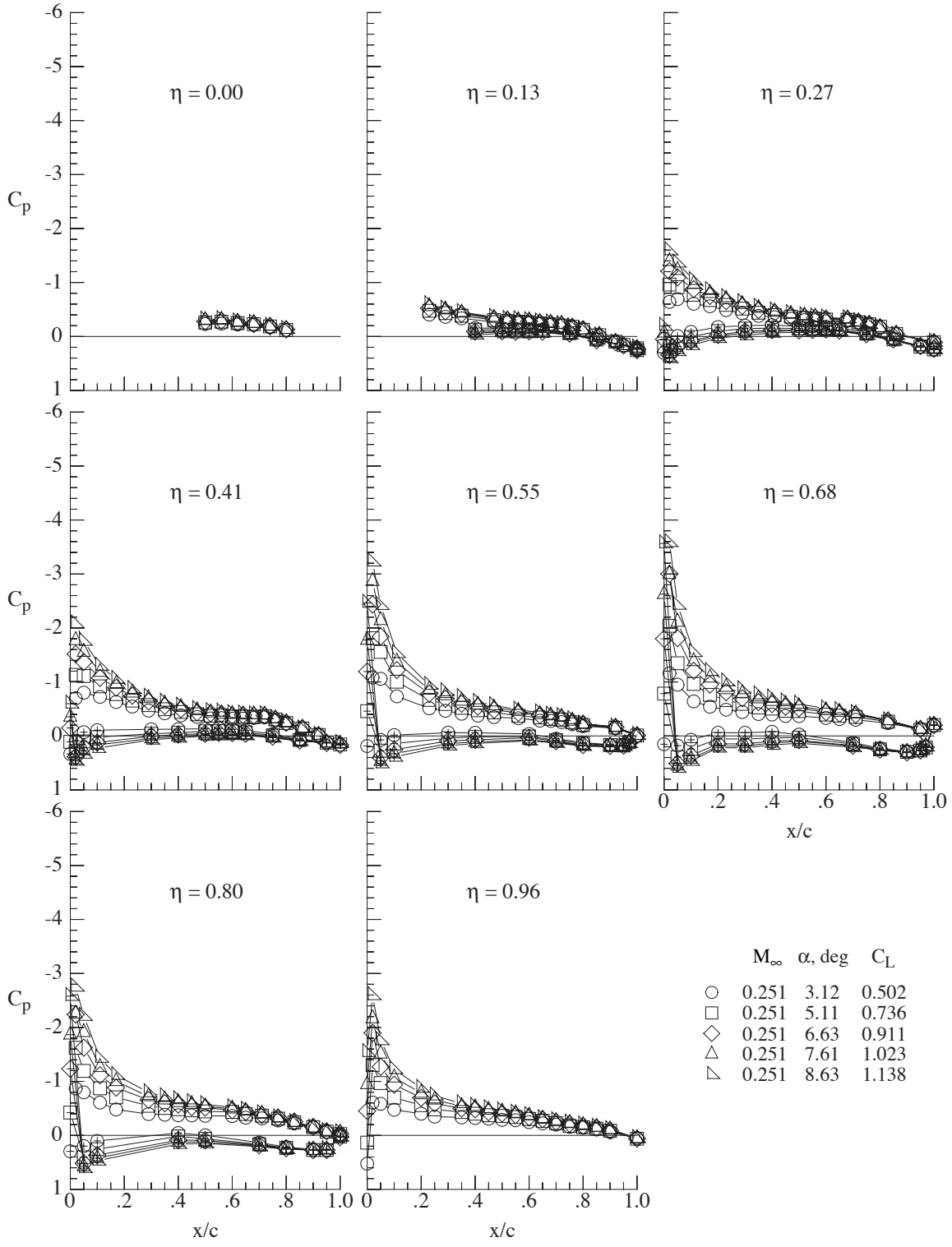

(a) Angles of attack from 3.12° to 8.63°.

Figure 22. Wing chordwise pressure coefficient variation at various angles of attack for the basic configuration at a Mach number of 0.25 and a Reynolds number of 3.5 x 10^6. Symbols with + indicate wing lower surface. Transition fixed.

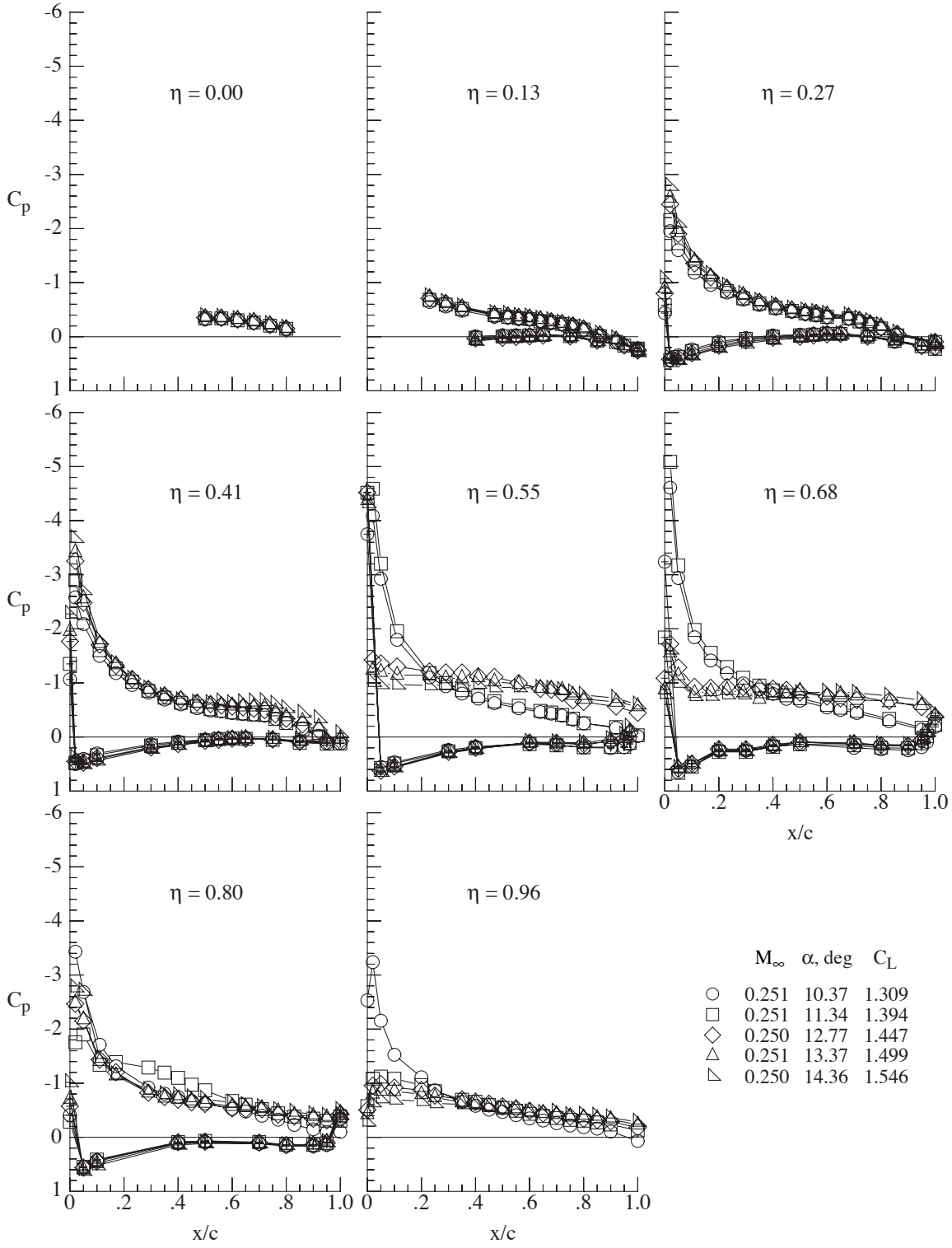

(b) Angles of attack from 10.37° to 14.36°.

Figure 22. Concluded.

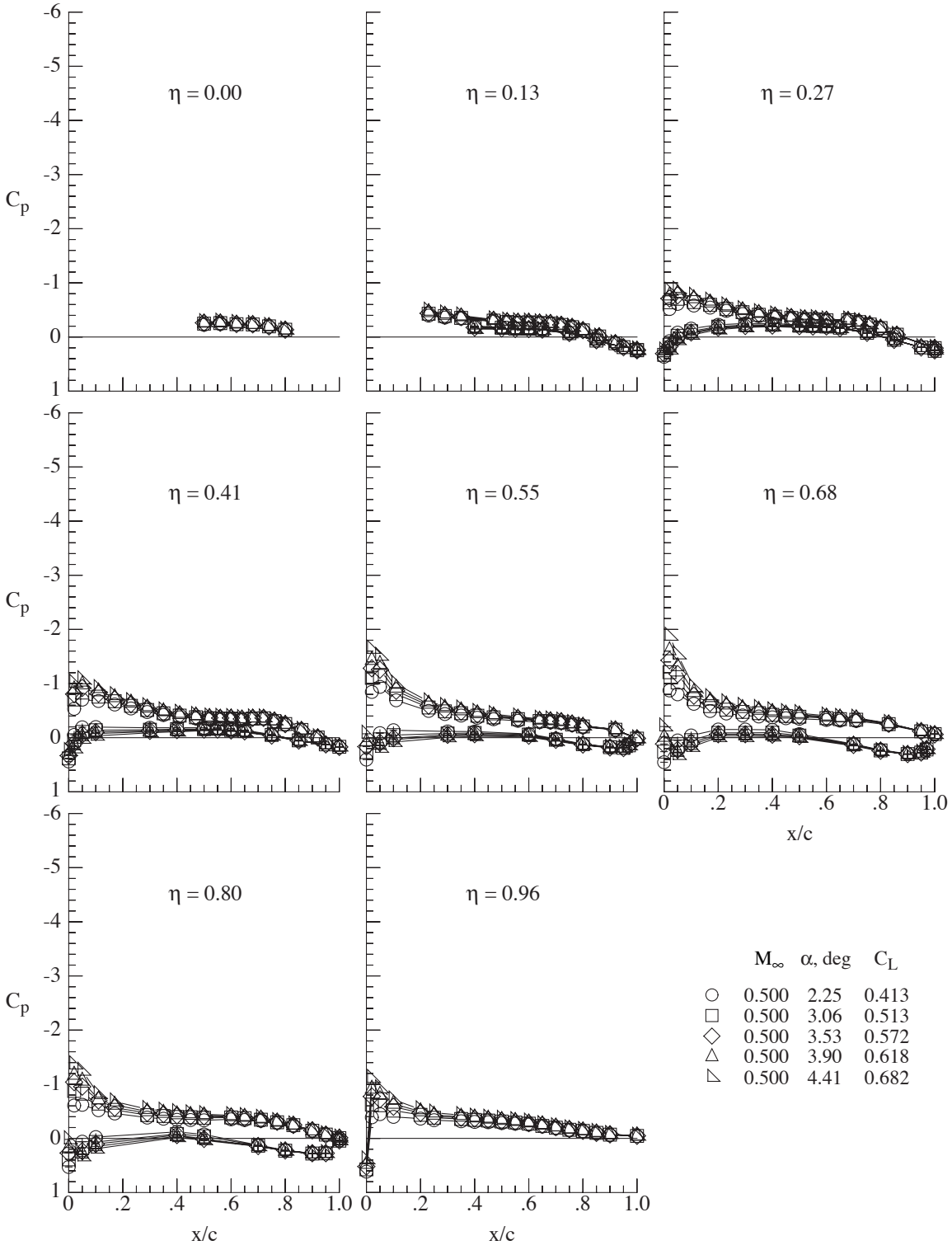

(a) Angles of attack from 2.25° to 4.41°.

Figure 23. Wing chordwise pressure coefficient variation at various angles of attack for the basic configuration at a Mach number of 0.50 and a Reynolds number of 3.5 x 10^6. Symbols with + indicate wing lower surface. Transition fixed.

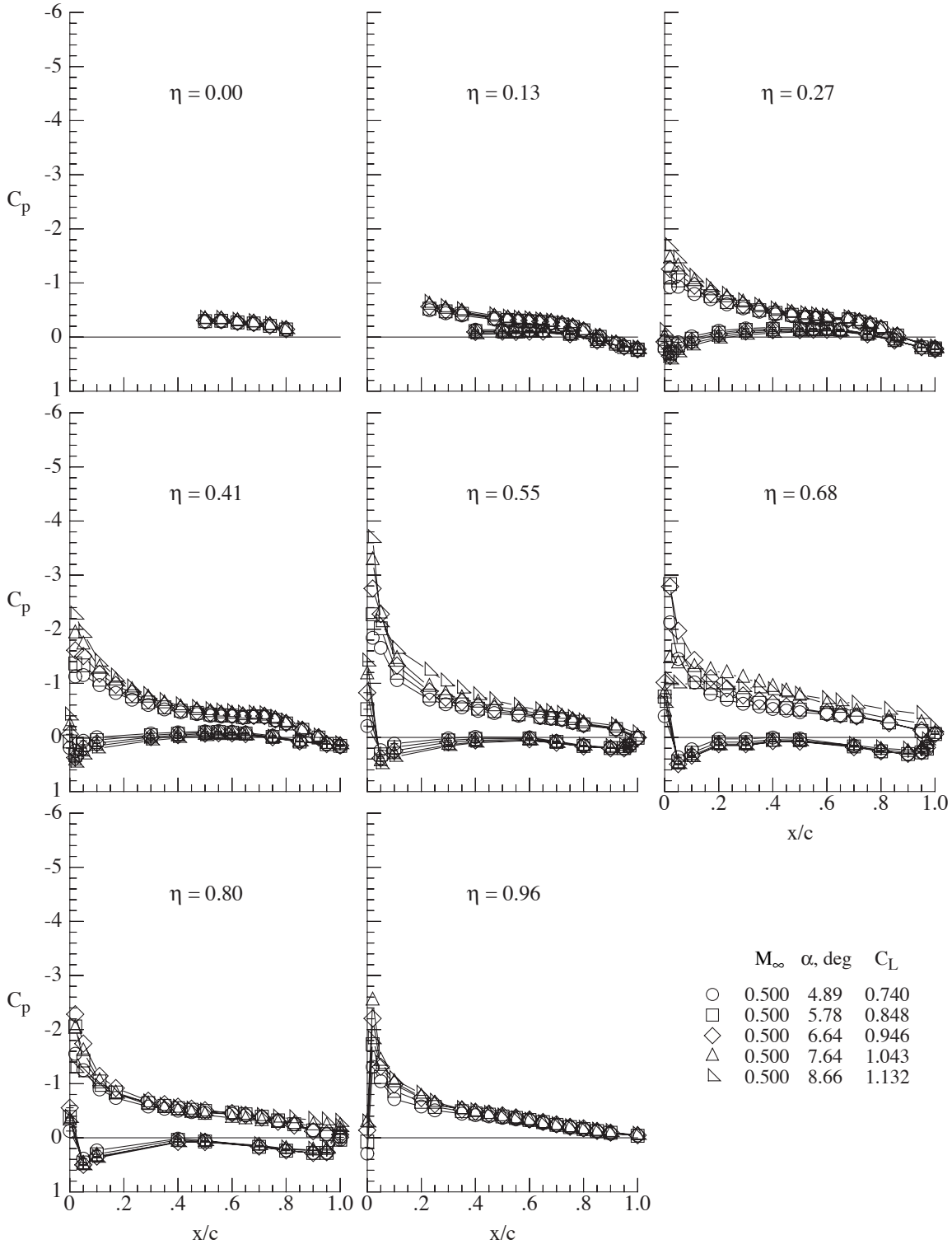

(b) Angles of attack from 4.89° to 8.66°.

Figure 23. Concluded.

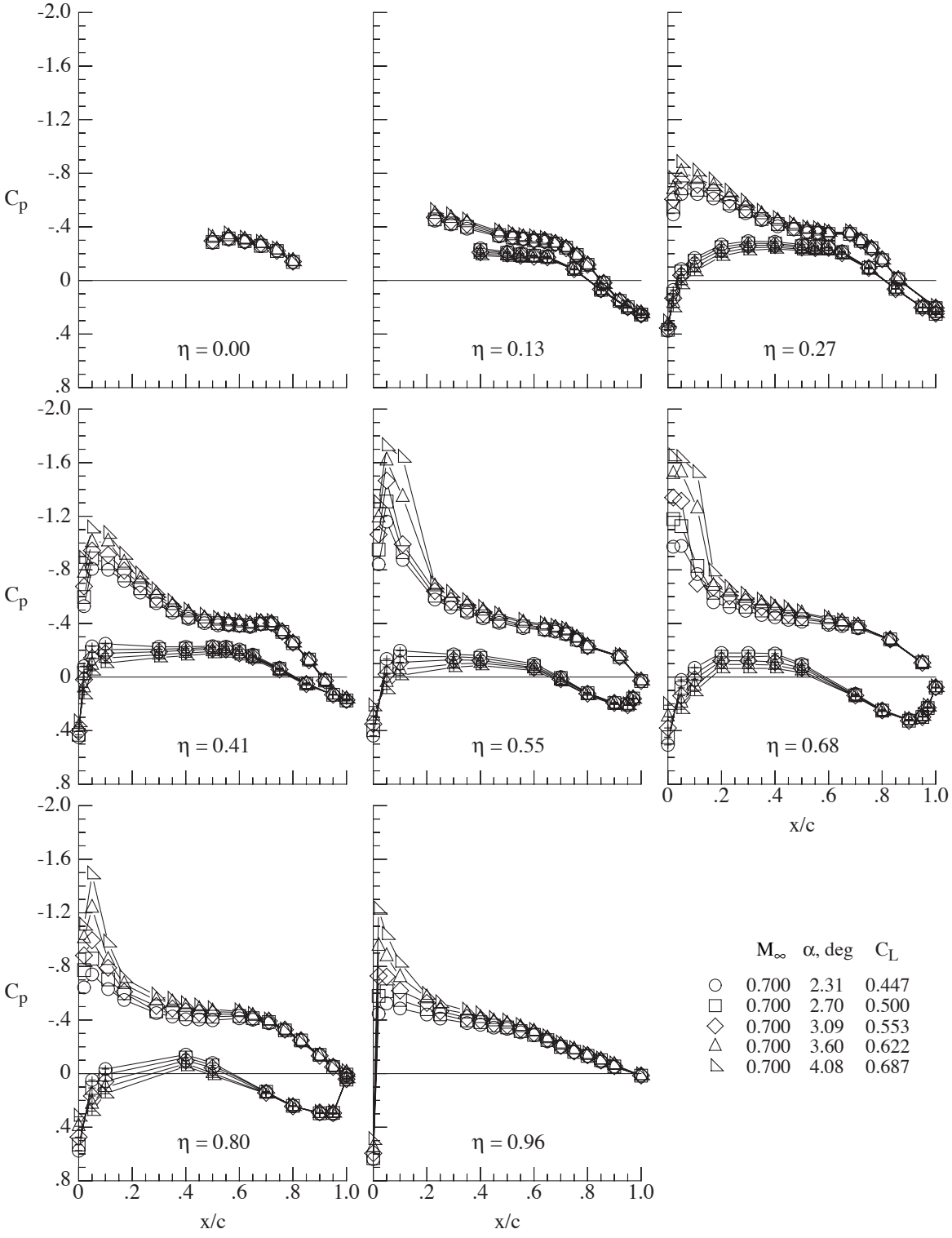

(a) Angle of attack from 2.31° to 4.08°.

Figure 24. Wing chordwise pressure coefficient variation at various angles of attack for the basic configuration at a Mach number of 0.70 and a Reynolds number of 3.5 x 10^6. Symbols with + indicate wing lower surface. Transition fixed.

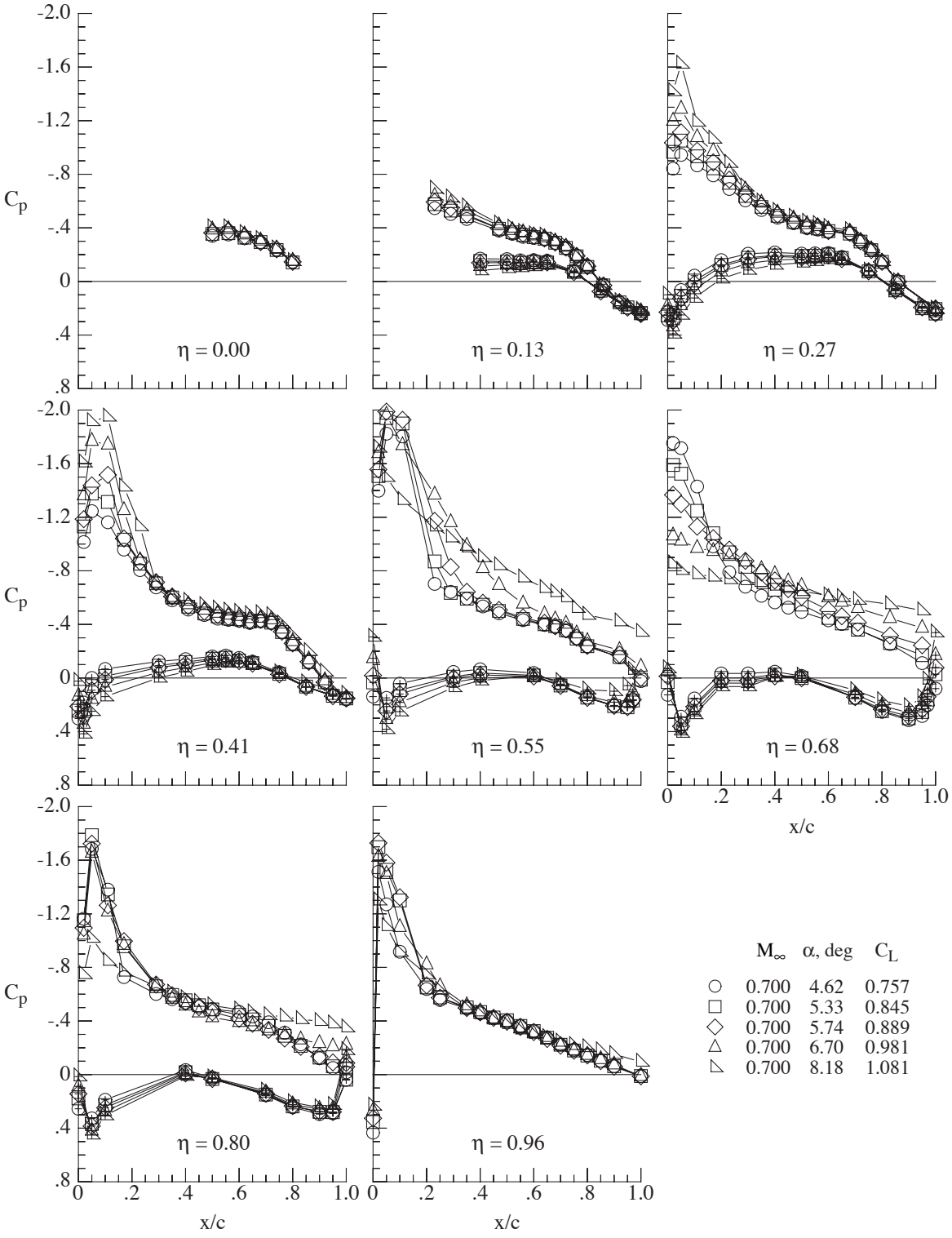

(b) Angle of attack from 4.62° to 8.18°.

Figure 24. Concluded.

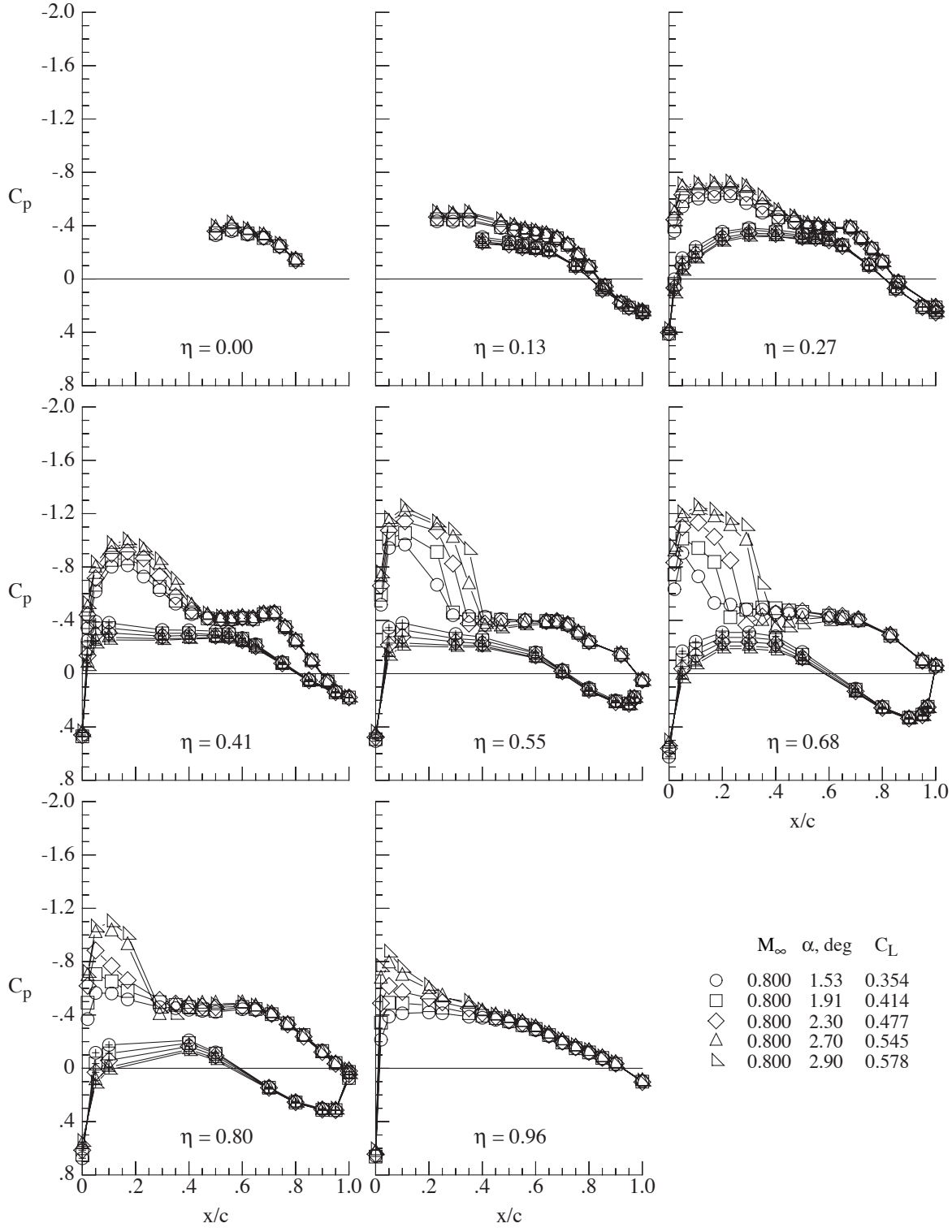

(a) Angle of attack from 1.53° to 2.90°.

Figure 25. Wing chordwise pressure coefficient variation at various angles of attack for the basic configuration at a Mach number of 0.80 and a Reynolds number of 3.5 x 10^6. Symbols with + indicate wing lower surface. Transition fixed.

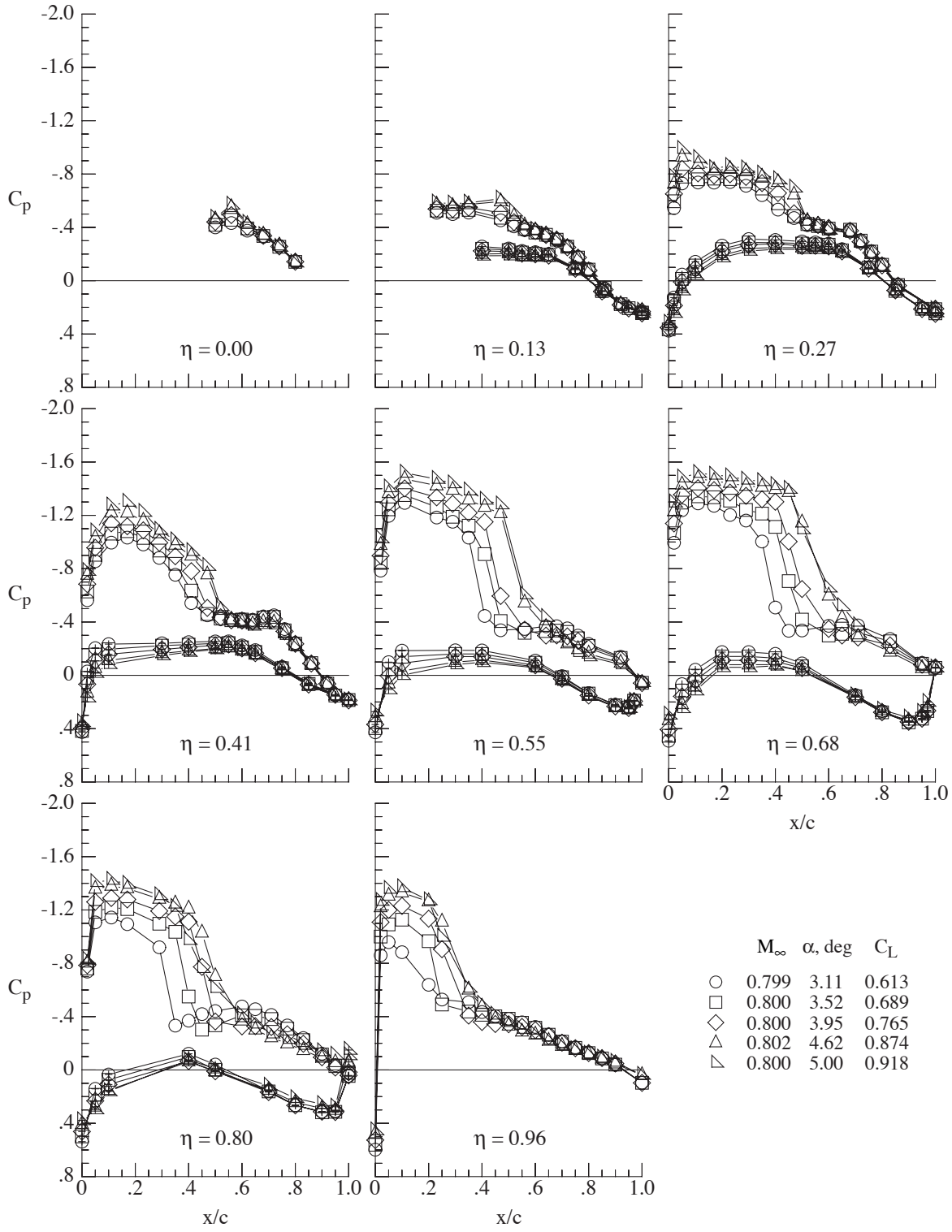

(b) Angle of attack from 3.11° to 5.00°.

Figure 25. Concluded.

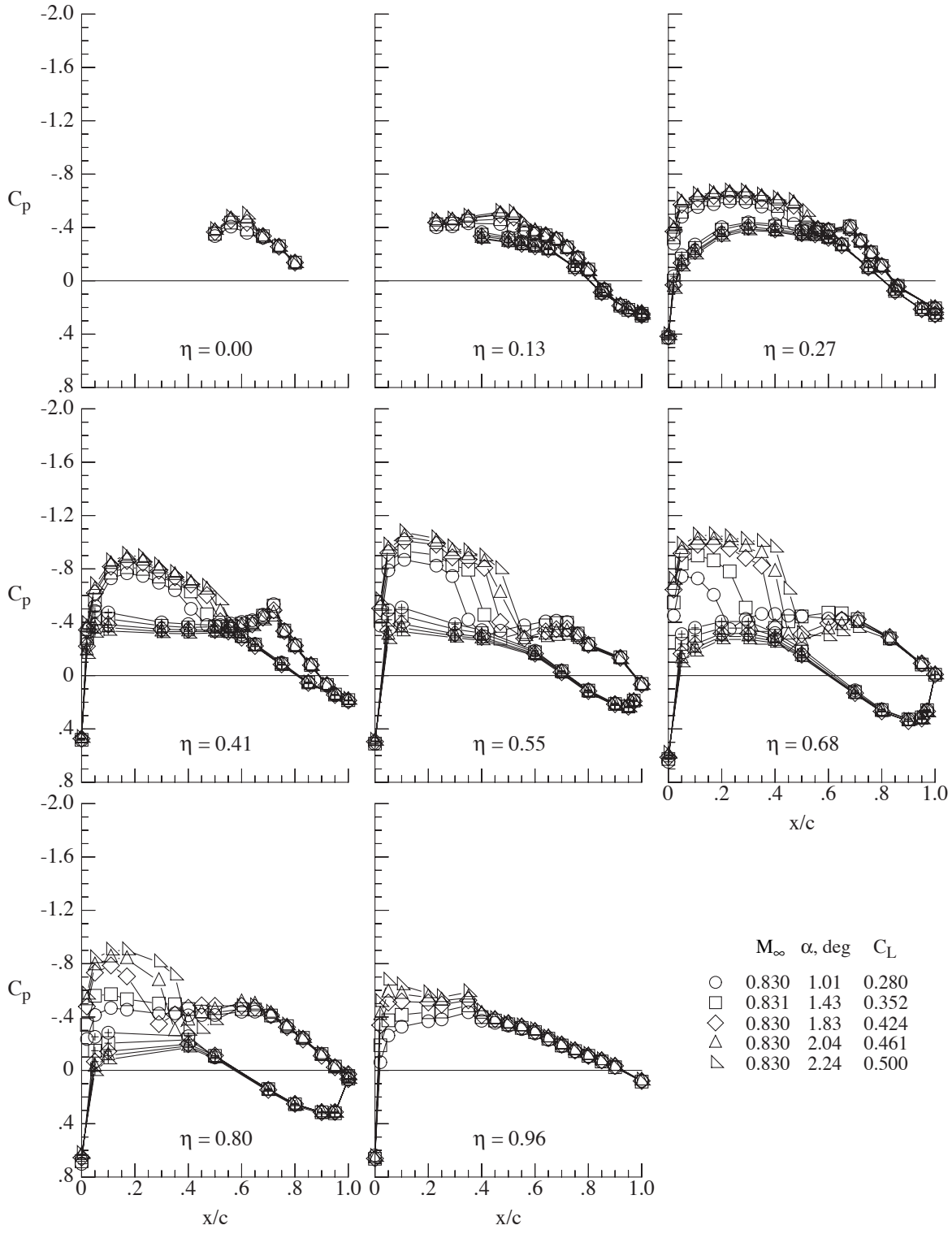

(a) Angle of attack from 1.01° to 2.24°.

Figure 26. Wing chordwise pressure coefficient variation at various angles of attack for the basic configuration at a Mach number of 0.83 and a Reynolds number of 3.5 x 10^6. Symbols with + indicate wing lower surface. Transition fixed.

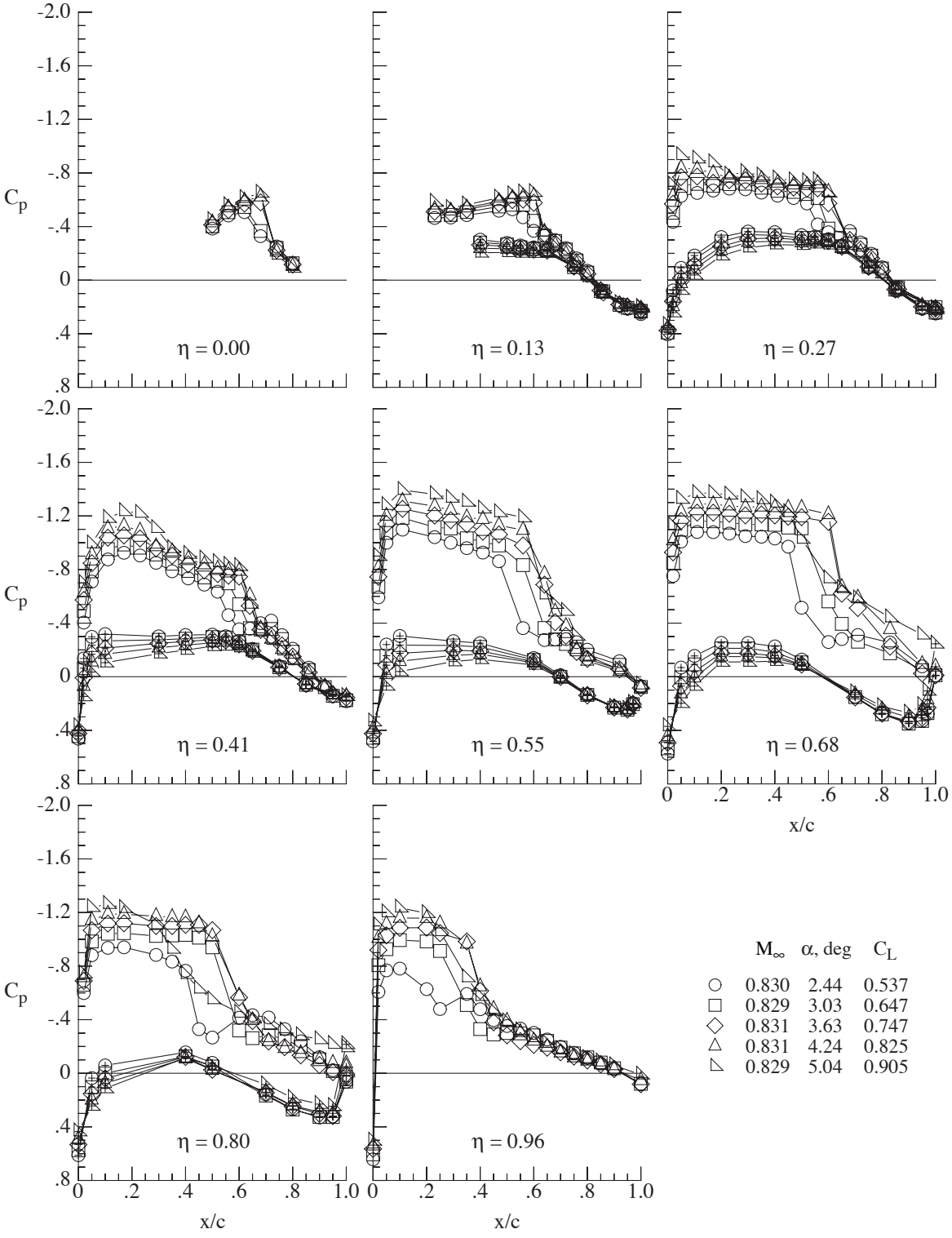

(b) Angle of attack from 2.44° to 5.04°.

Figure 26. Concluded.

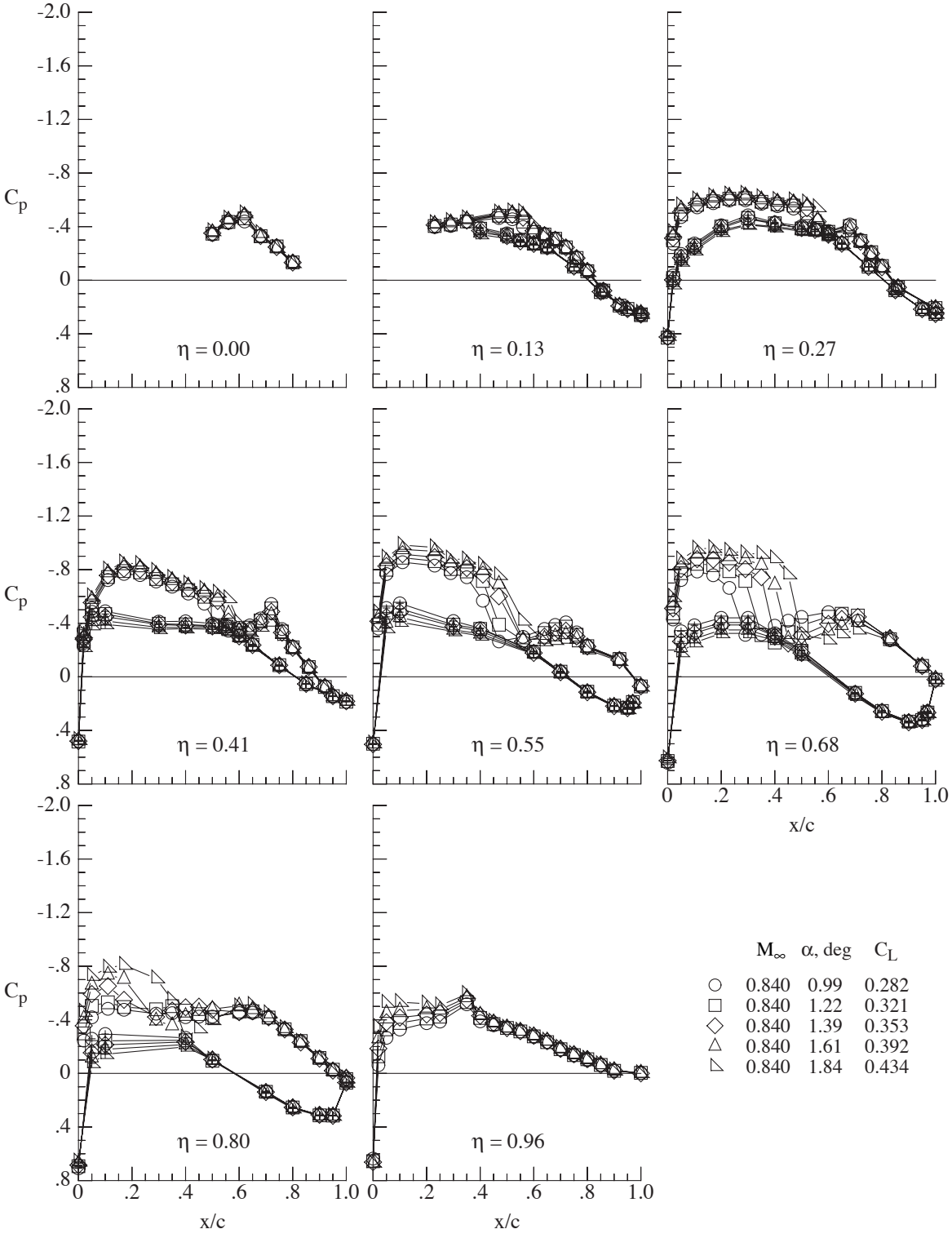

(a) Angle of attack from 0.99° to 1.84°.

Figure 27. Wing chordwise pressure coefficient variation at various angles of attack for the basic configuration at a Mach number of 0.84 and a Reynolds number of 3.5 x 10^6. Symbols with + indicate wing lower surface. Transition fixed.

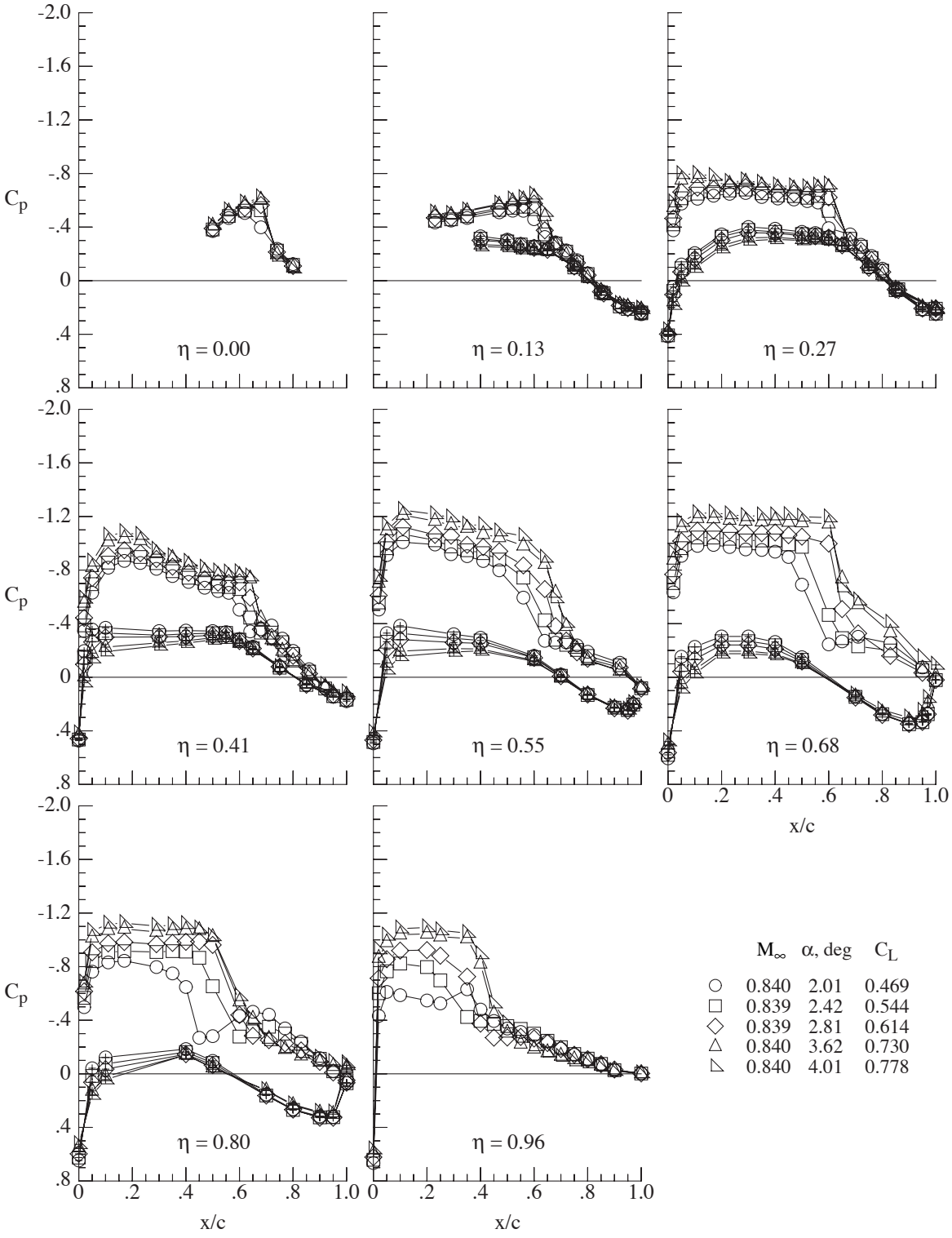

(b) Angle of attack from 2.01° to 4.01°.

Figure 27. Concluded.

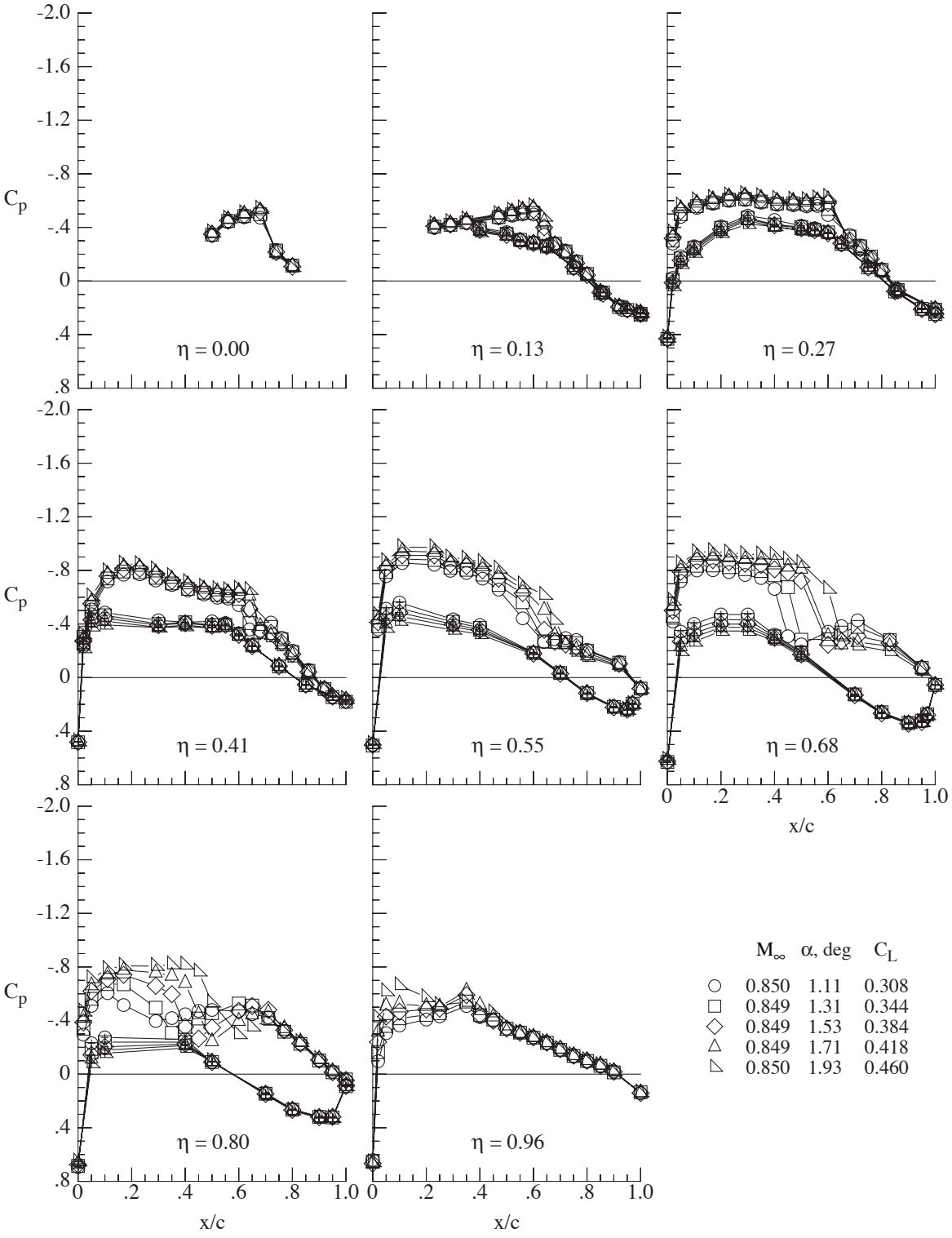

(a) Angle of attack from 1.11° to 1.93°.

Figure 28. Wing chordwise pressure coefficient variation at various angles of attack for the basic configuration at a Mach number of 0.85 and a Reynolds number of 3.5 x 10^6. Symbols with + indicate wing lower surface. Transition fixed.

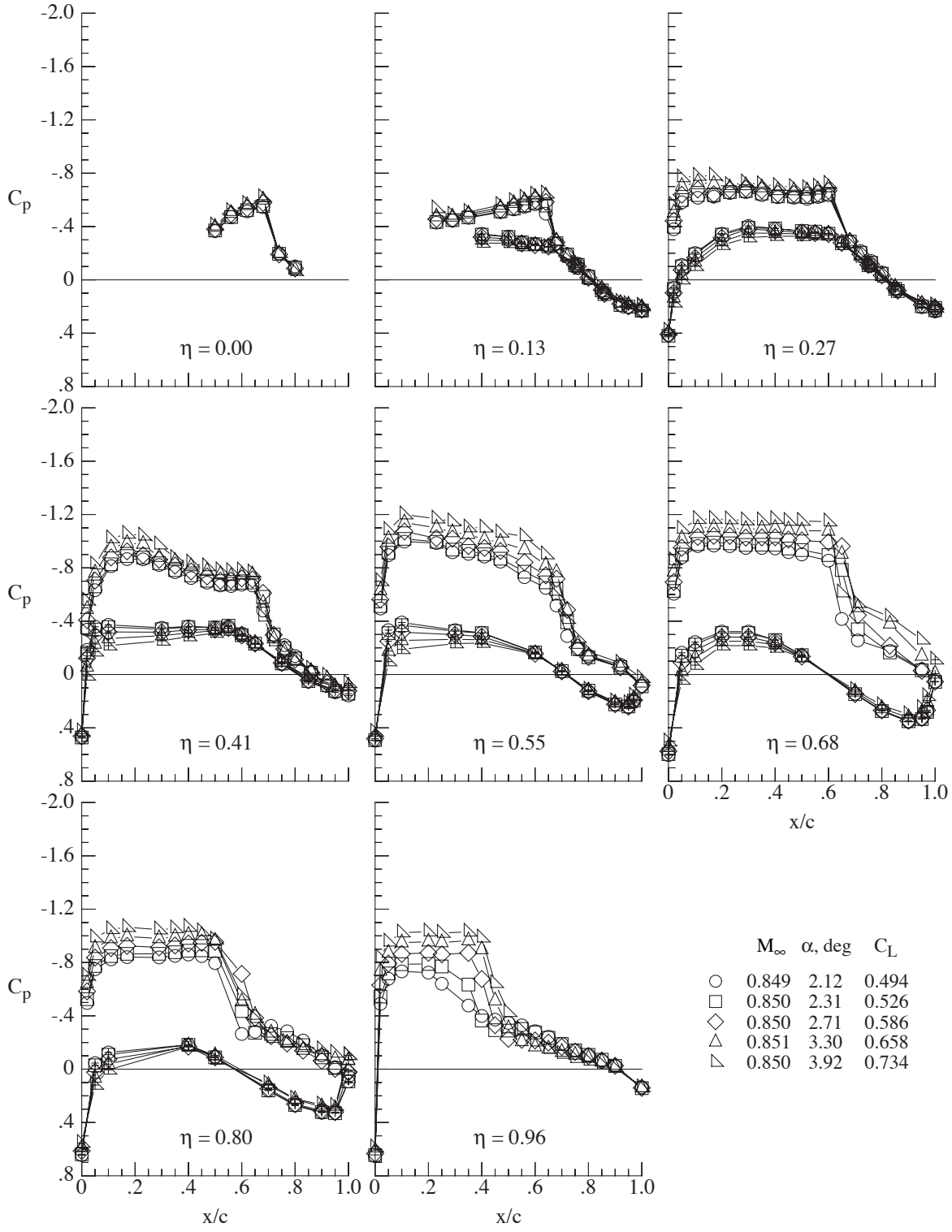

(b) Angle of attack from 2.12° to 3.92°.

Figure 28. Concluded.

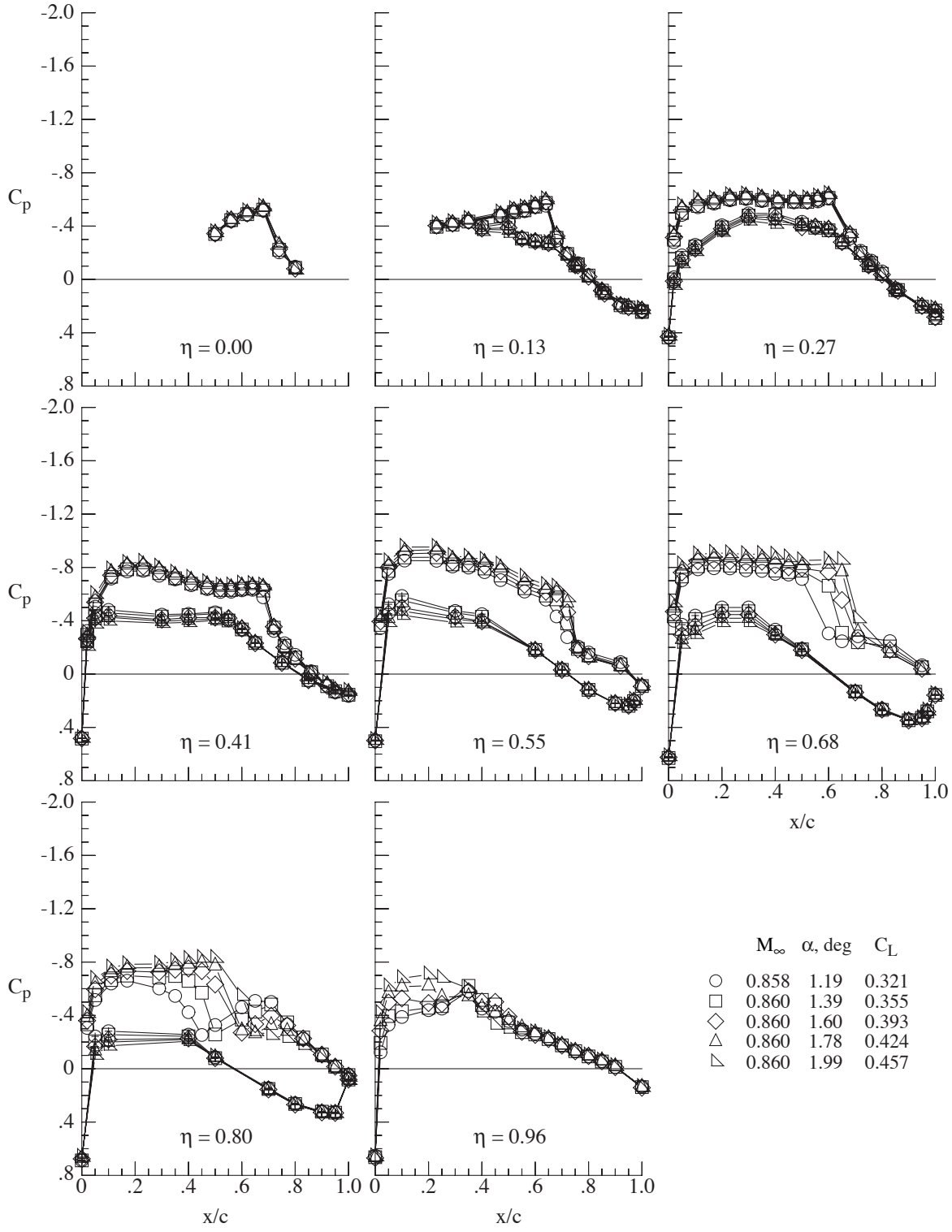

(a) Angle of attack from 1.19° to 1.99°.

Figure 29. Wing chordwise pressure coefficient variation at various angles of attack for the basic configuration at a Mach number of 0.86 and a Reynolds number of 3.5 x 10^6. Symbols with + indicate wing lower surface. Transition fixed.

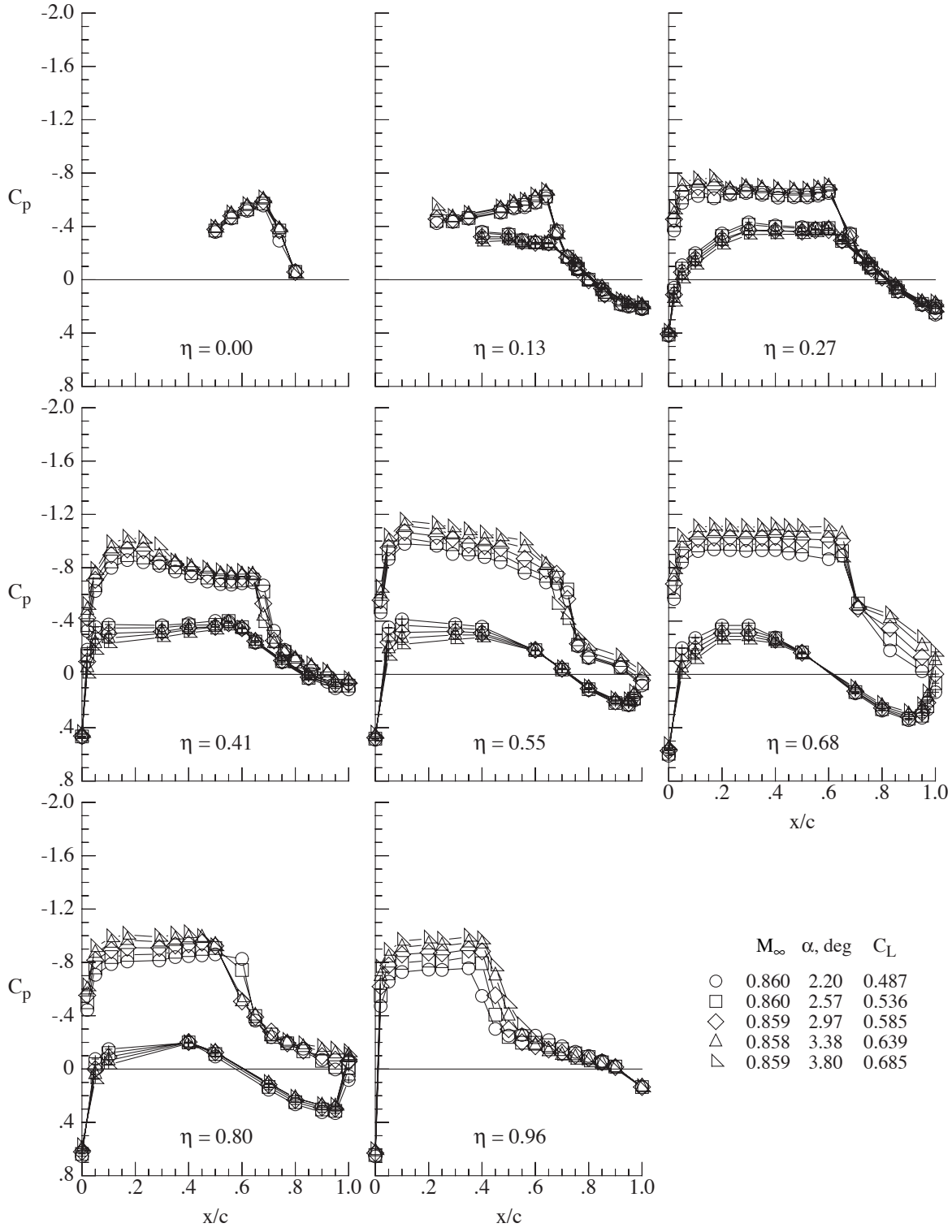

(b) Angle of attack from 2.20° to 3.80°.

Figure 29. Concluded.

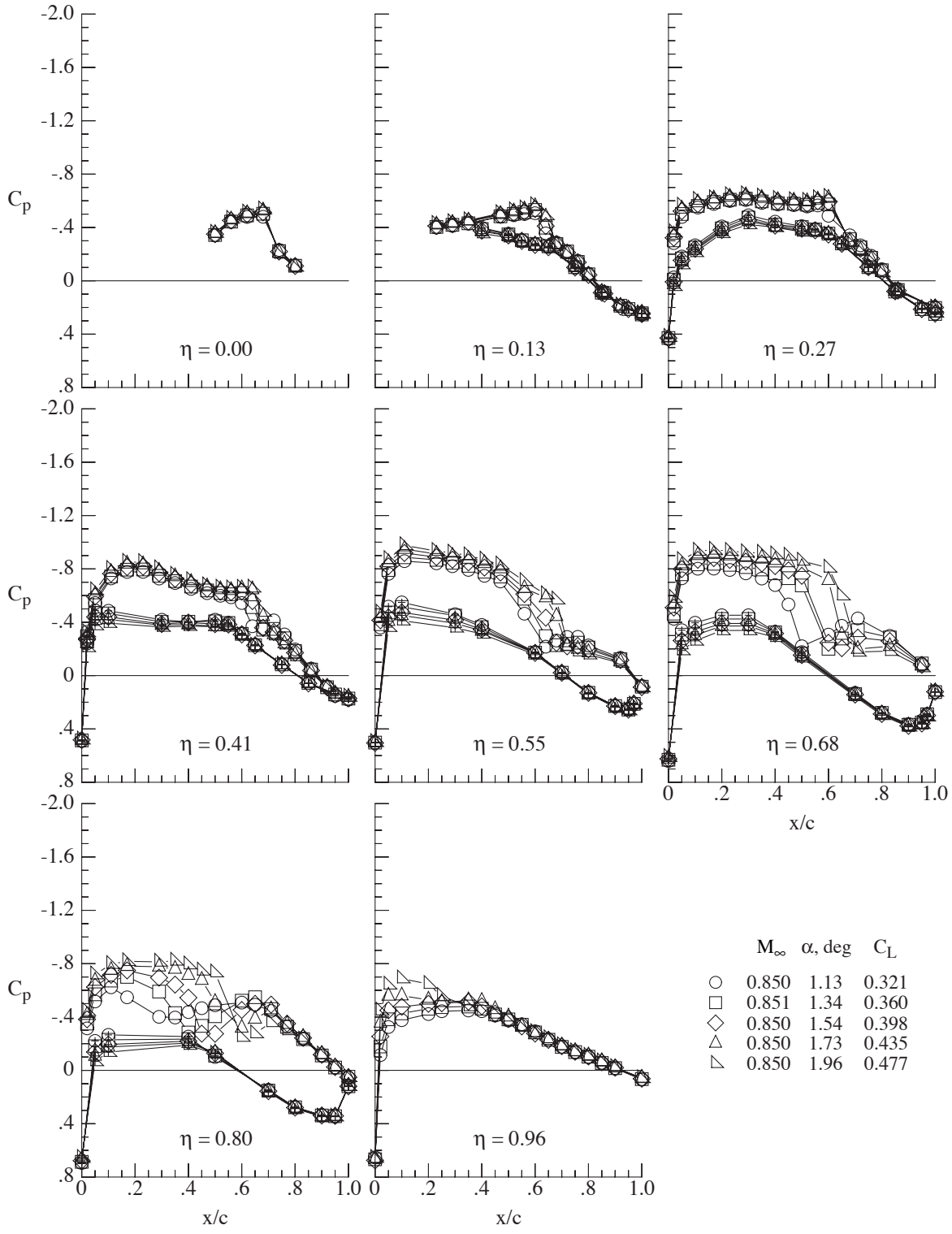

(a) Angle of attack from 1.13° to 1.96°.

Figure 30. Wing chordwise pressure coefficient variation at various angles of attack for the basic configuration at a Mach number of 0.85 and a Reynolds number of 3.5 x 10^6. Symbols with + indicate wing lower surface. Transition free.

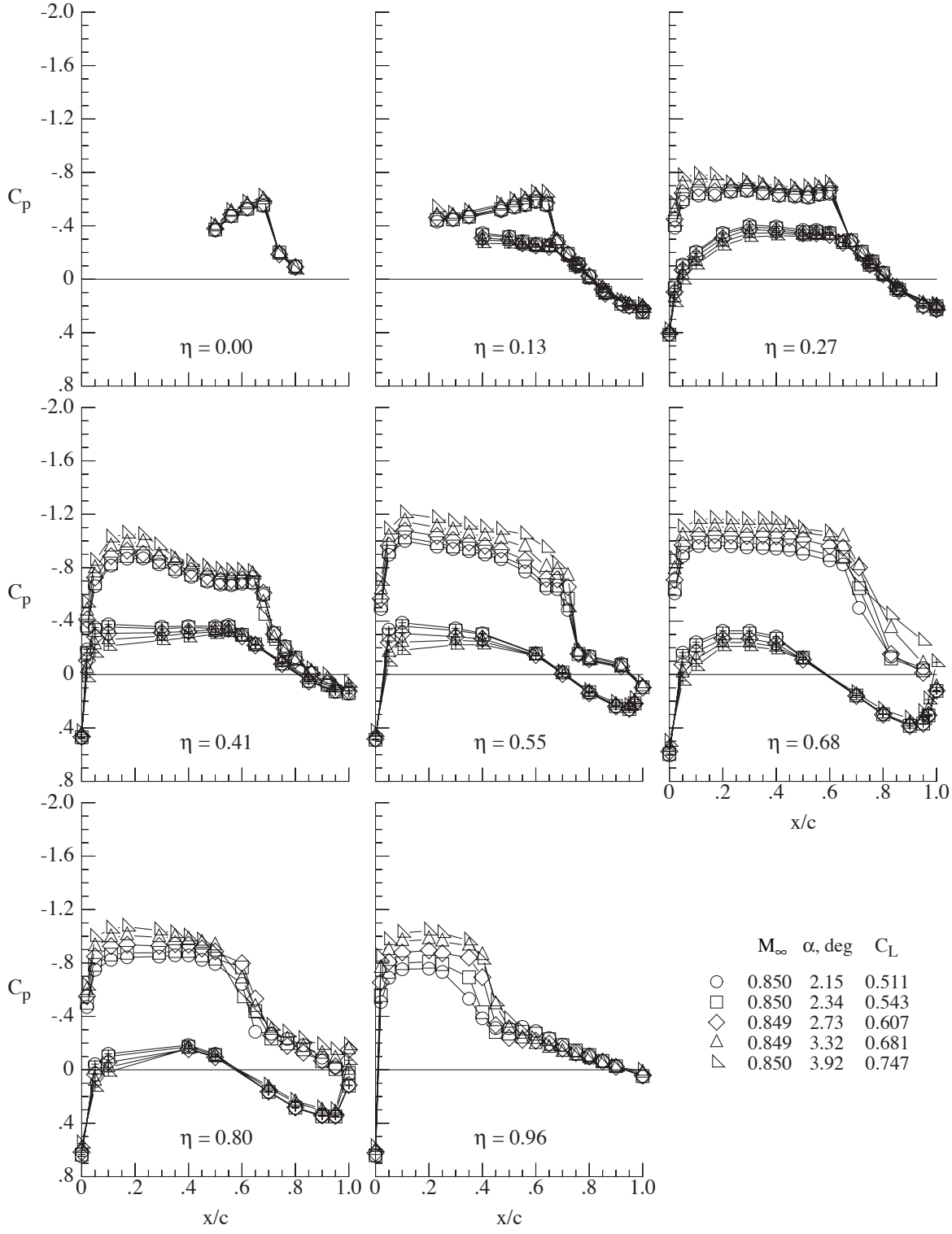

(b) Angle of attack from 2.15° to 3.92°.

Figure 30. Concluded.

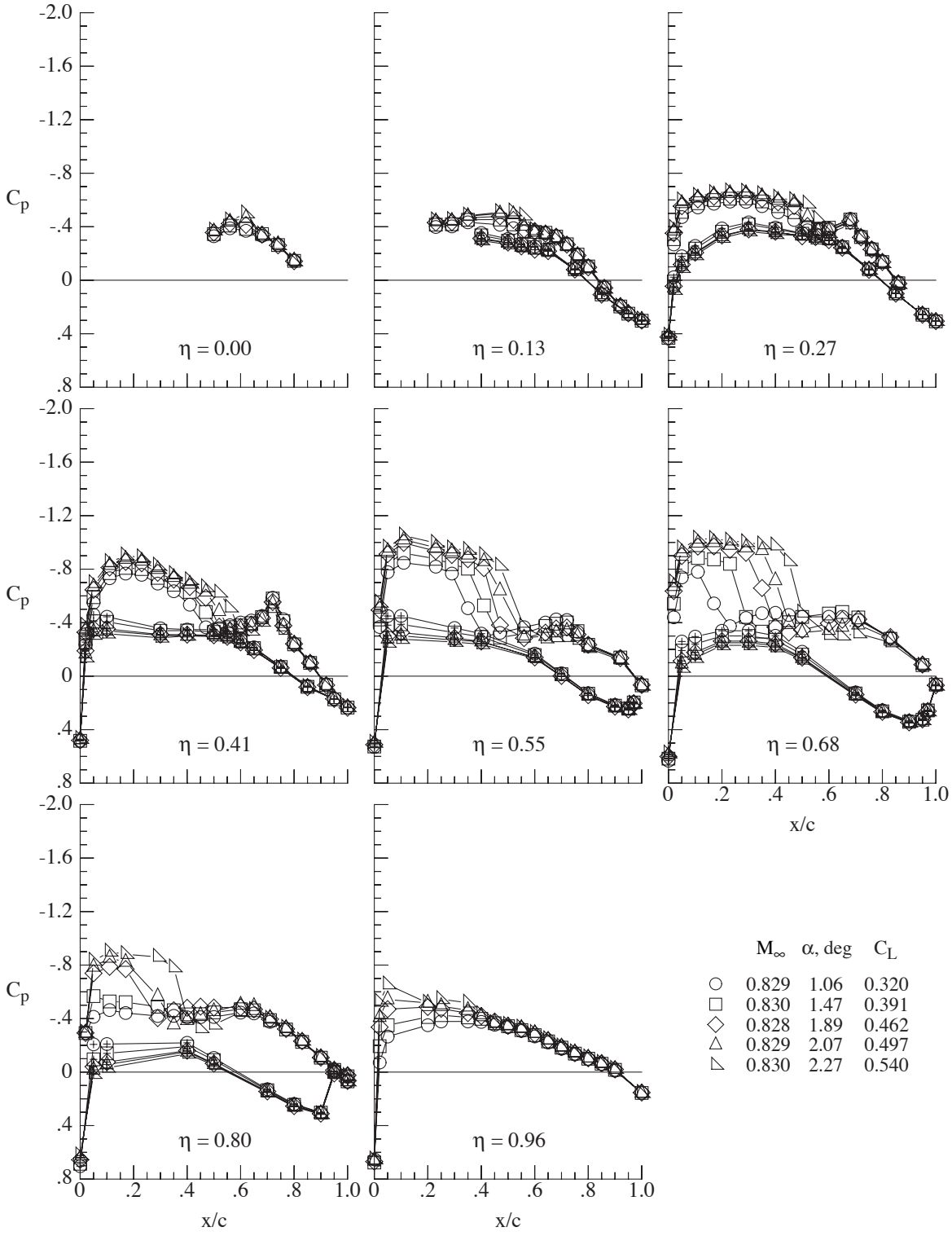

(a) Angle of attack from 1.06° to 2.27°.

Figure 31. Wing chordwise pressure coefficient variation at various angles of attack for the basic configuration at a Mach number of 0.83 and a Reynolds number of 12.3 x 10^6. Symbols with + indicate wing lower surface.

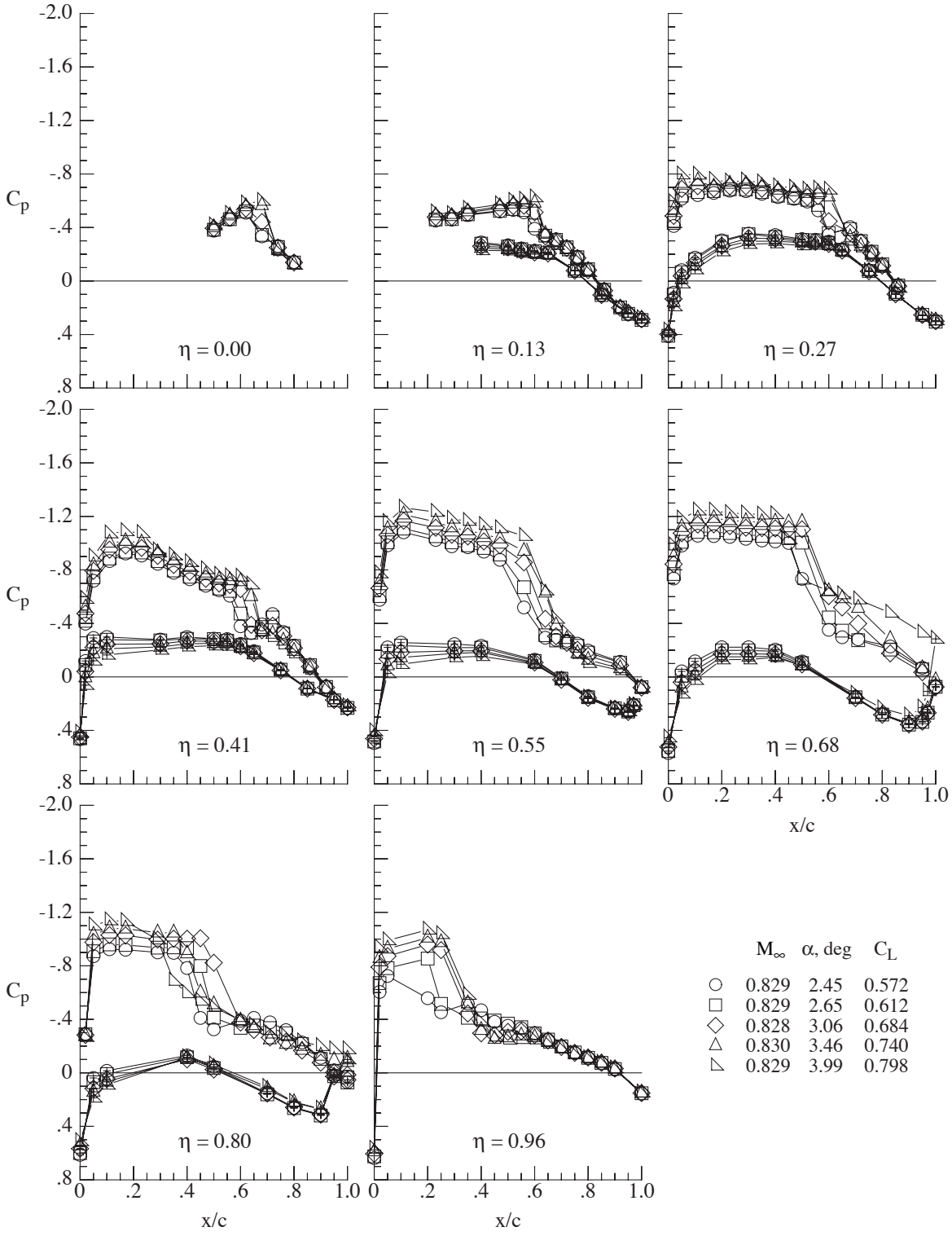

(b) Angle of attack from 2.45° to 3.99°.

Figure 31. Concluded.

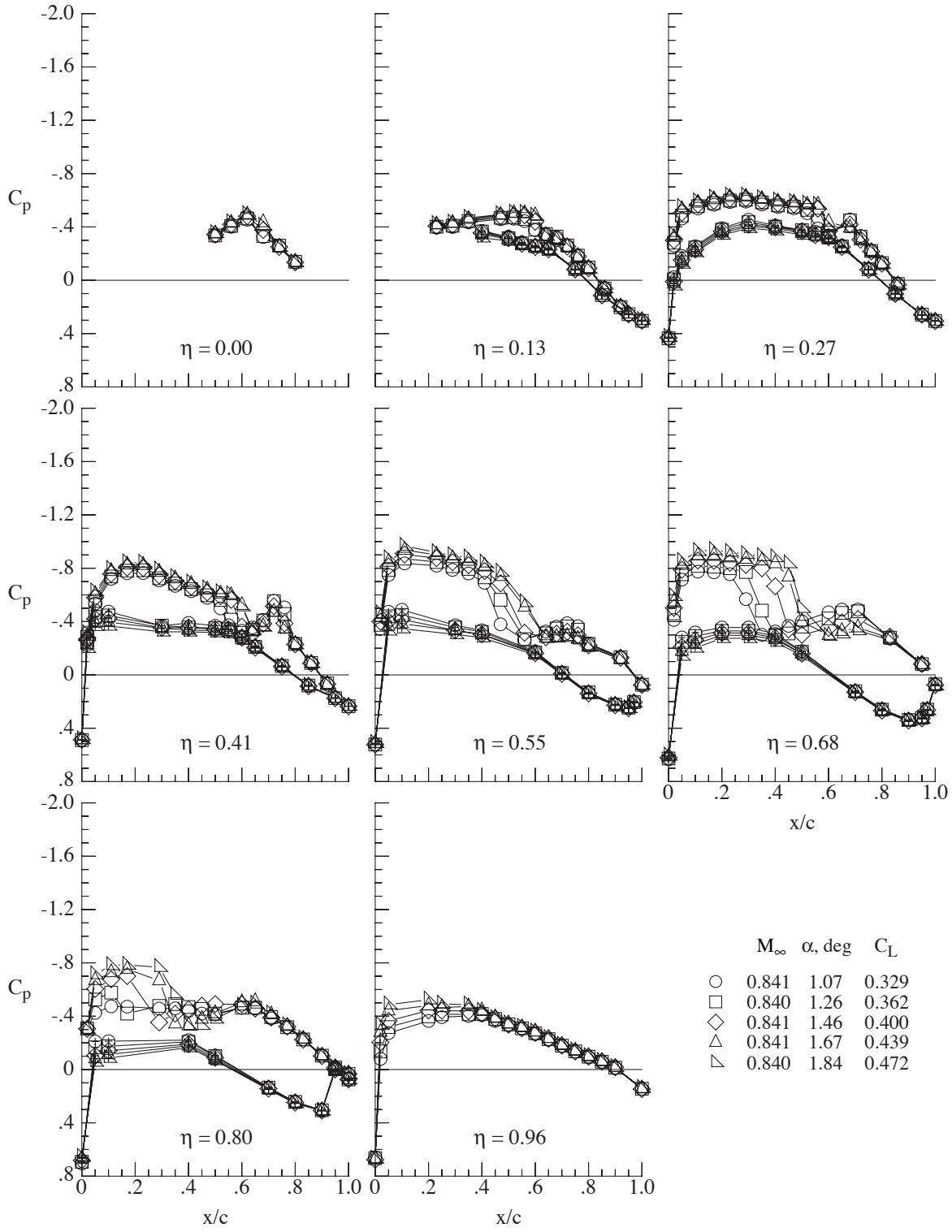

(a) Angle of attack from 1.07° to 1.84°.

Figure 32. Wing chordwise pressure coefficient variation at various angles of attack for the basic configuration at a Mach number of 0.84 and a Reynolds number of 12.3 x 10^6. Symbols with + indicate wing lower surface.

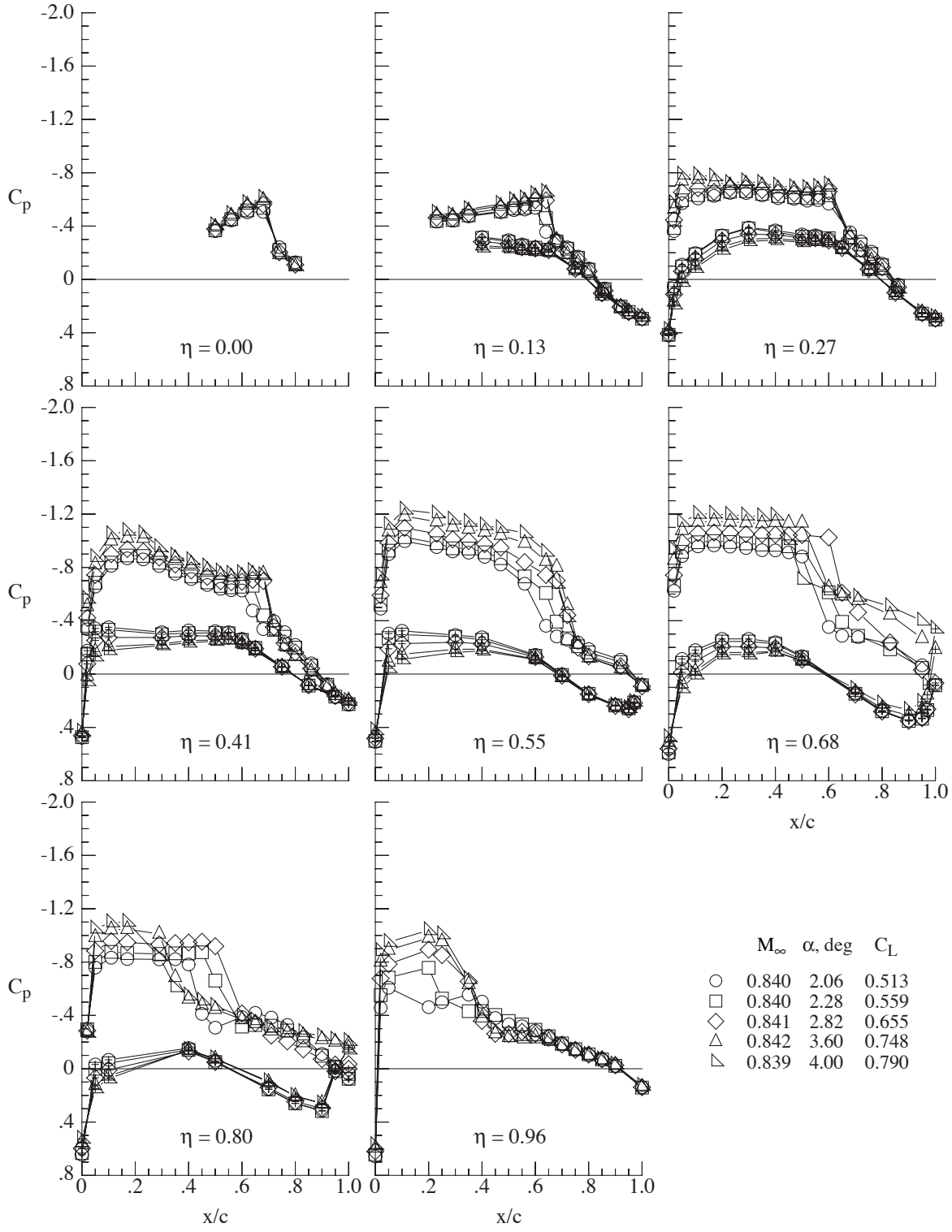

(b) Angle of attack from 2.06° to 4.00°.

Figure 32. Concluded.

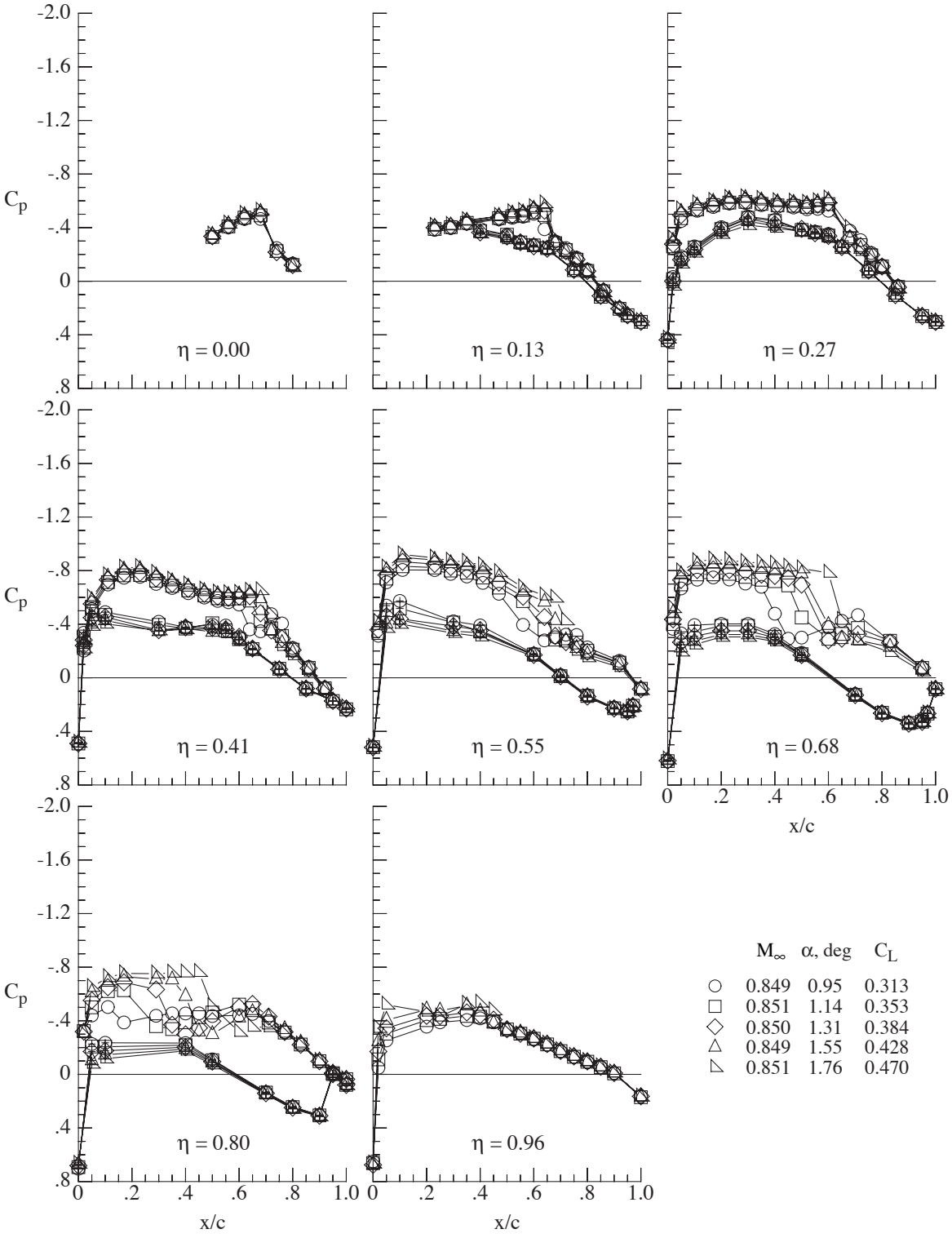

(a) Angle of attack from 0.95° to 1.76°.

Figure 33. Wing chordwise pressure coefficient variation at various angles of attack for the basic configuration at a Mach number of 0.85 and a Reynolds number of 12.3 x 10^6. Symbols with + indicate wing lower surface.

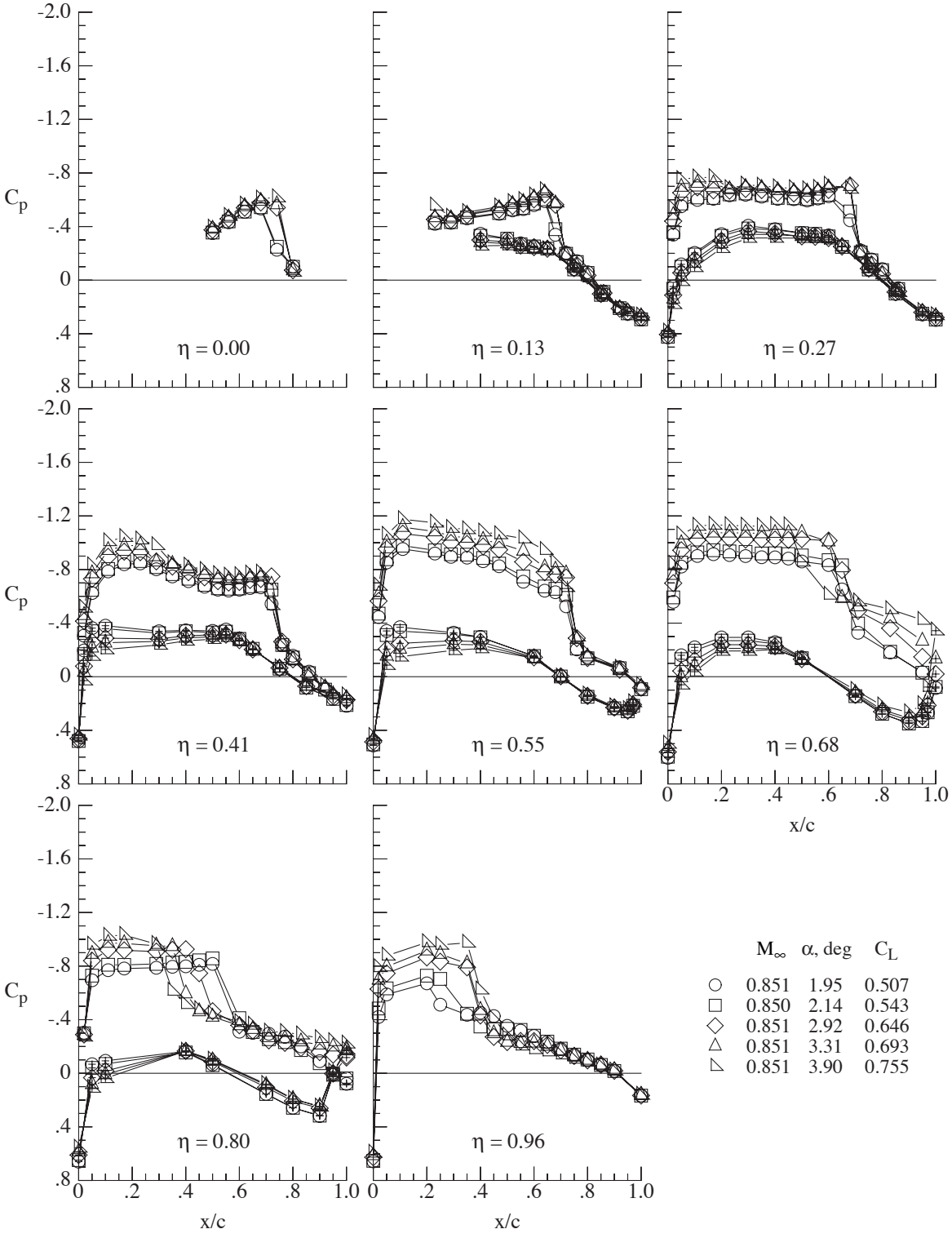

(b) Angle of attack from 1.95° to 3.90°.

Figure 33. Concluded.

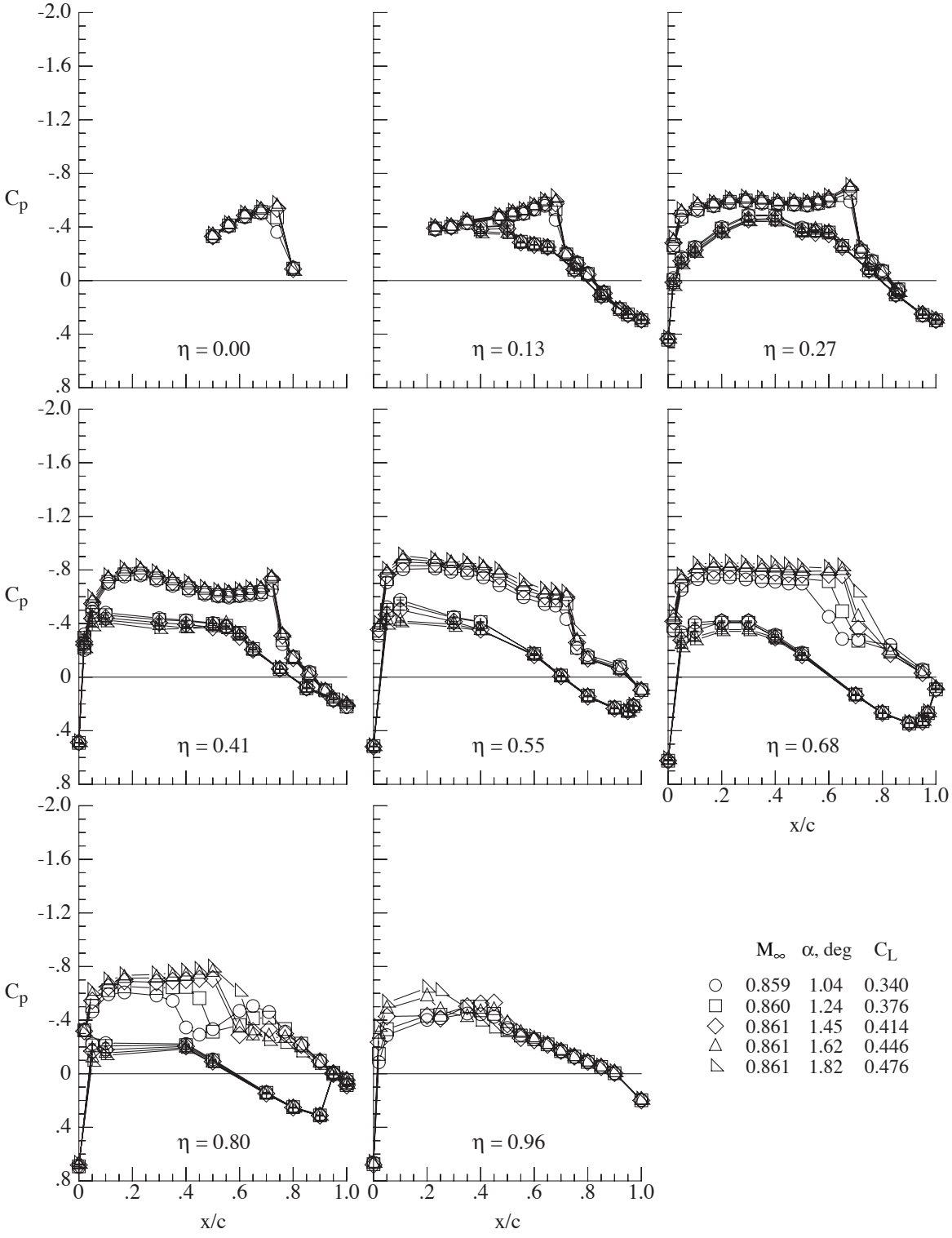

(a) Angle of attack from 1.04° to 1.82°.

Figure 34. Wing chordwise pressure coefficient variation at various angles of attack for the basic configuration at a Mach number of 0.86 and a Reynolds number of 12.3 x 10^6. Symbols with + indicate wing lower surface.

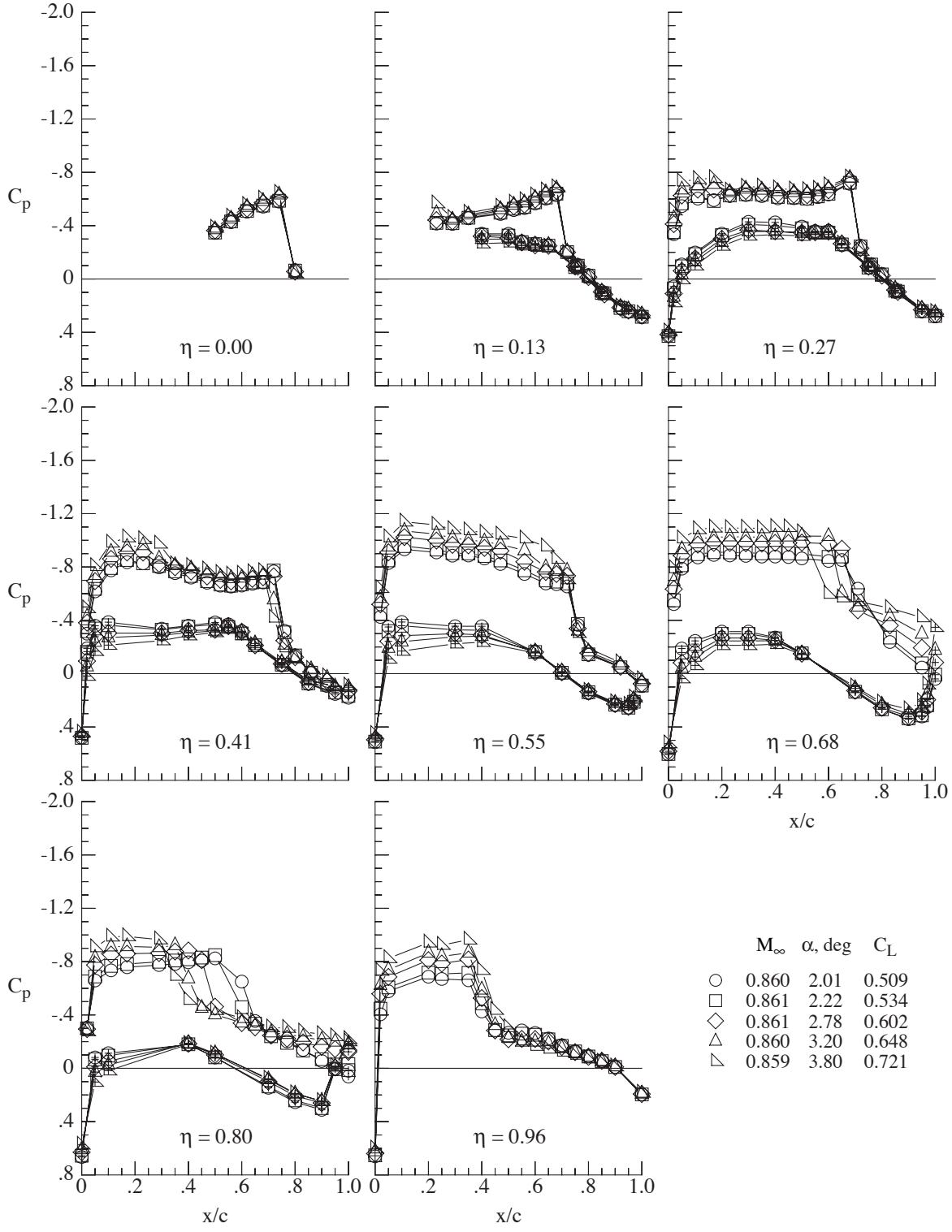

(b) Angle of attack from 2.01° to 3.80°.

Figure 34. Concluded.

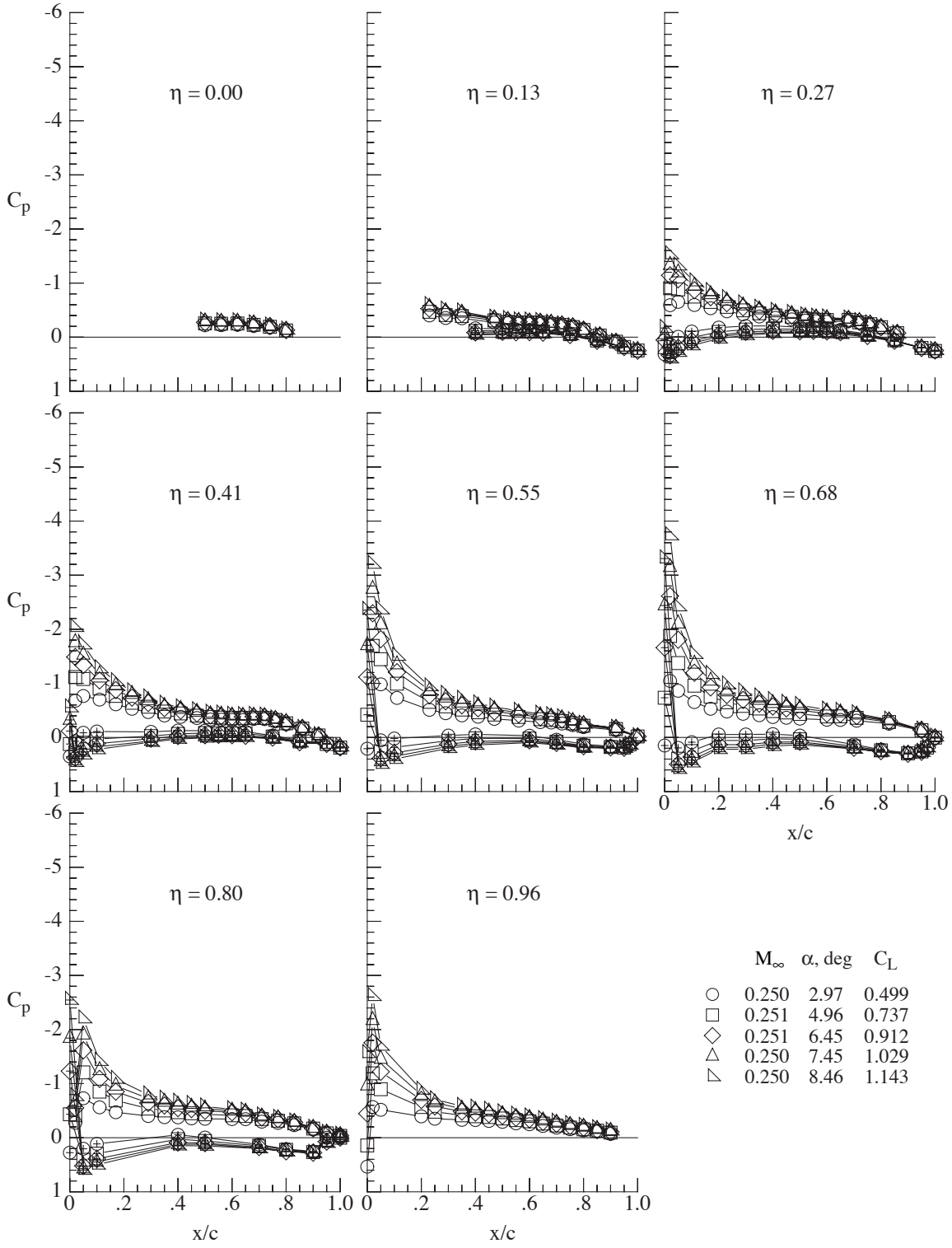

(a) Angles of attack from 2.97° to 8.46°.

Figure 35. Wing chordwise pressure coefficient variation at various angles of attack for the basic configuration at a Mach number of 0.25 and a Reynolds number of 21.5 x 10^6. Symbols with + indicate wing lower surface.

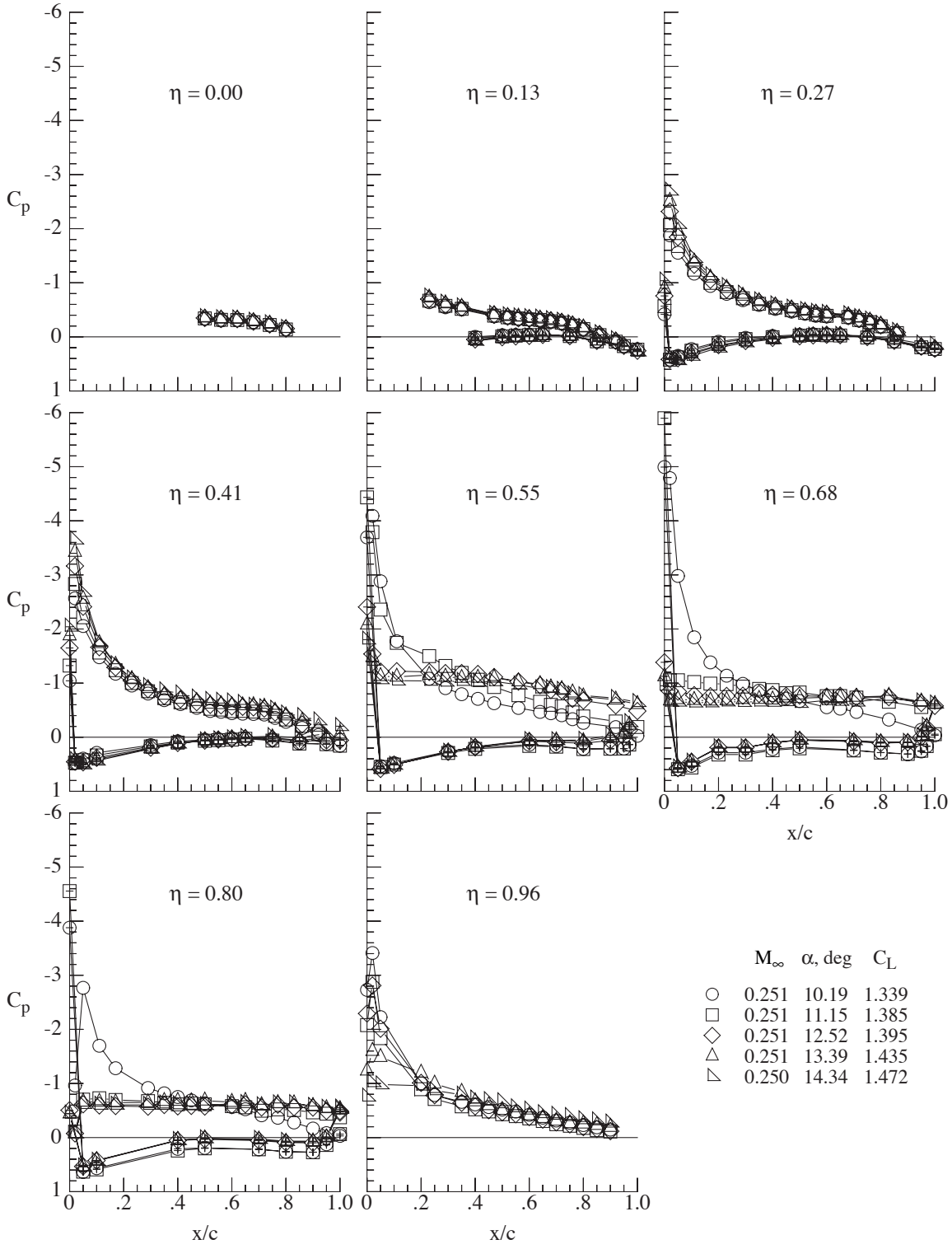

(b) Angles of attack from 10.19° to 14.34°.

Figure 35. Concluded.

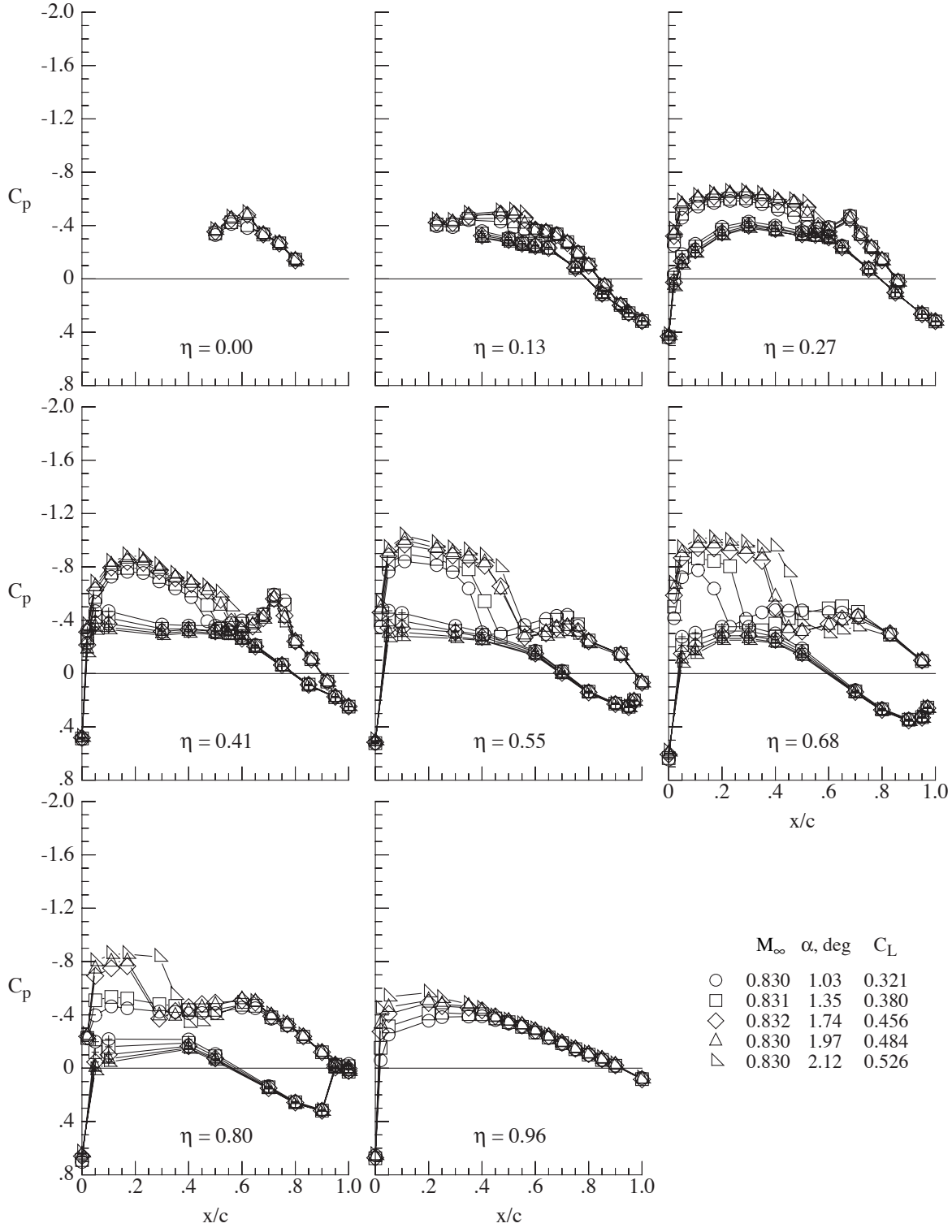

(a) Angle of attack from 1.03° to 2.12°.

Figure 36. Wing chordwise pressure coefficient variation at various angles of attack for the basic configuration at a Mach number of 0.83 and a Reynolds number of 25.0 x 10^6. Symbols with + indicate wing lower surface.

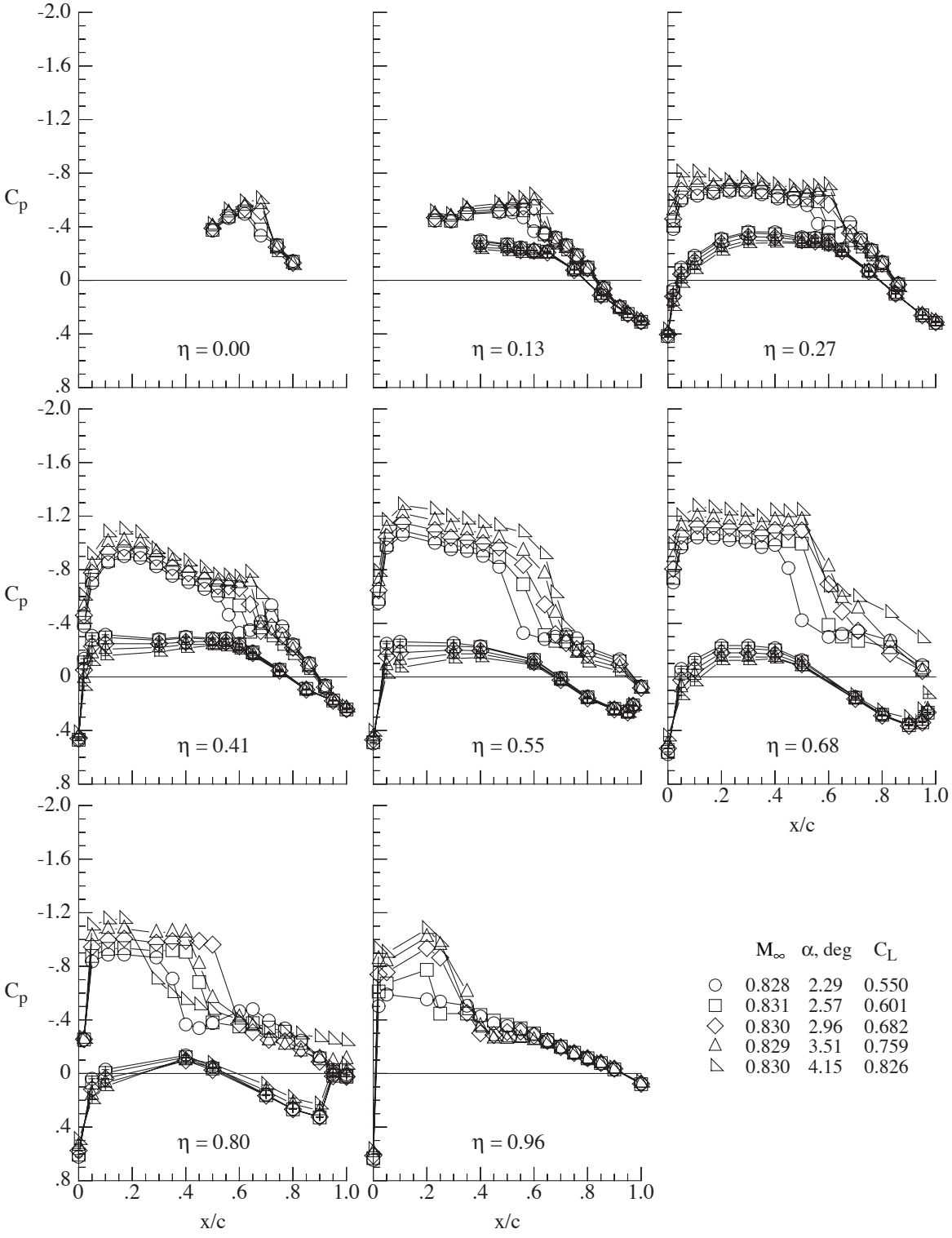

(b) Angle of attack from 2.29° to 4.15°.

Figure 36. Concluded.

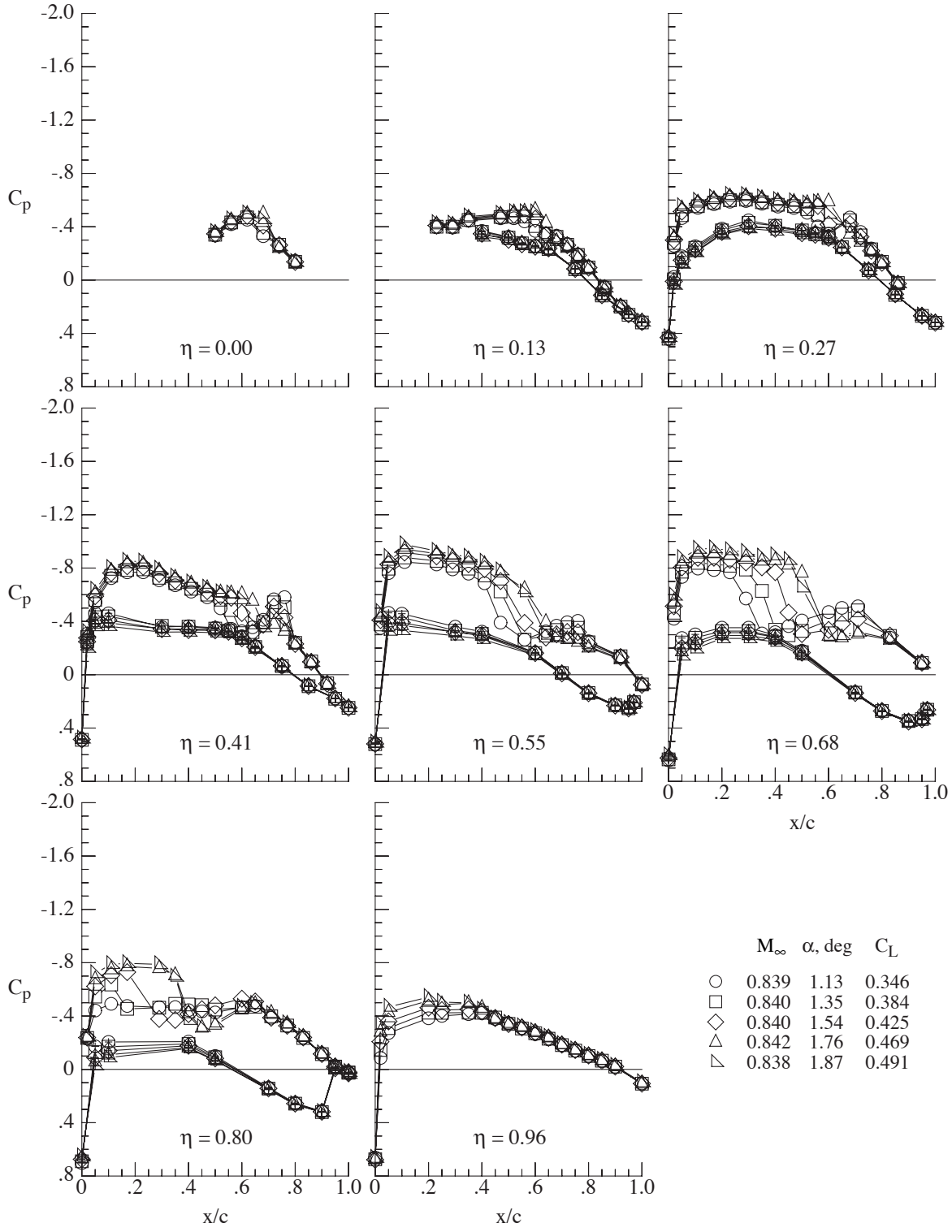

(a) Angle of attack from 1.13° to 1.87°.

Figure 37. Wing chordwise pressure coefficient variation at various angles of attack for the basic configuration at a Mach number of 0.84 and a Reynolds number of 25.0 x 10^6. Symbols with + indicate wing lower surface.

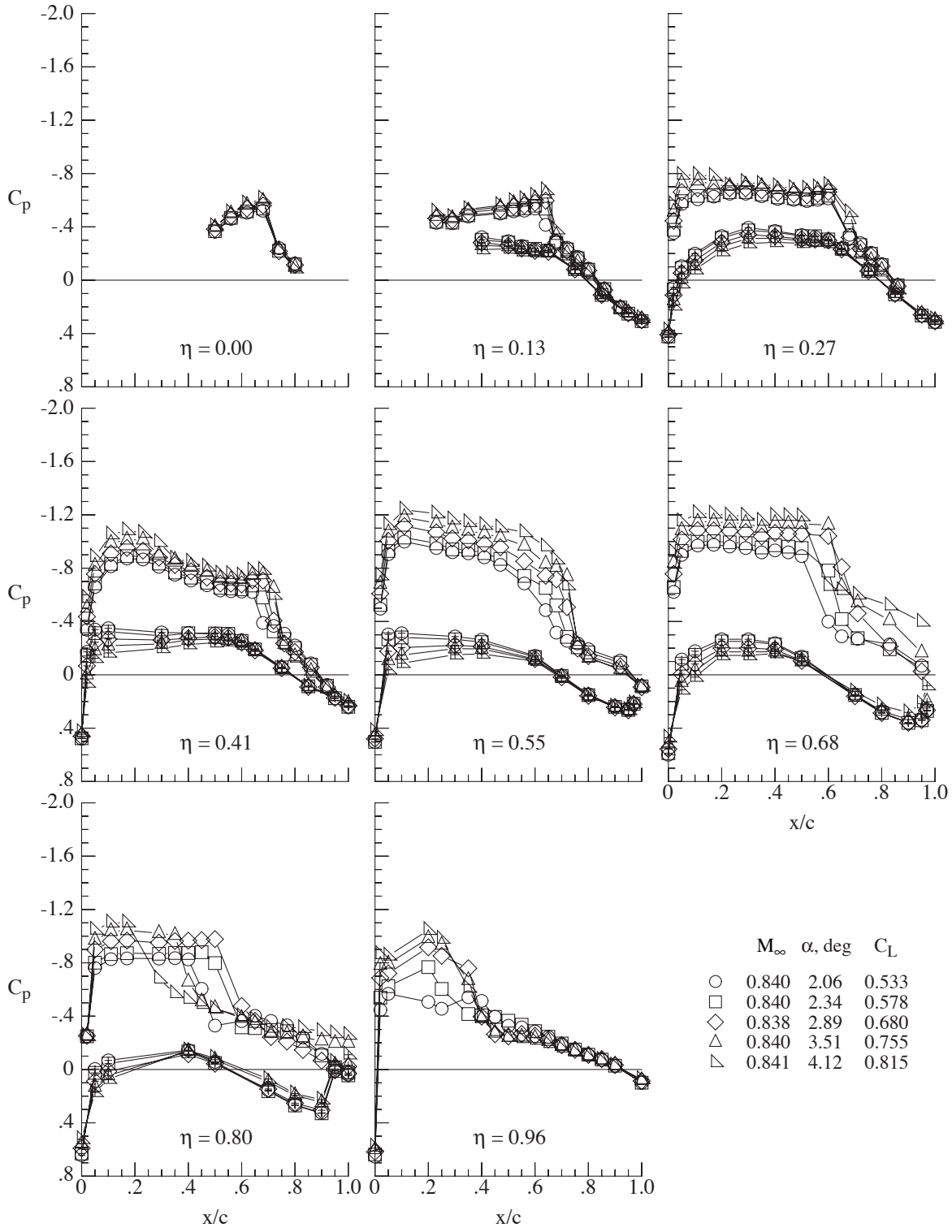

(b) Angle of attack from 2.06° to 4.12°.

Figure 37. Concluded.

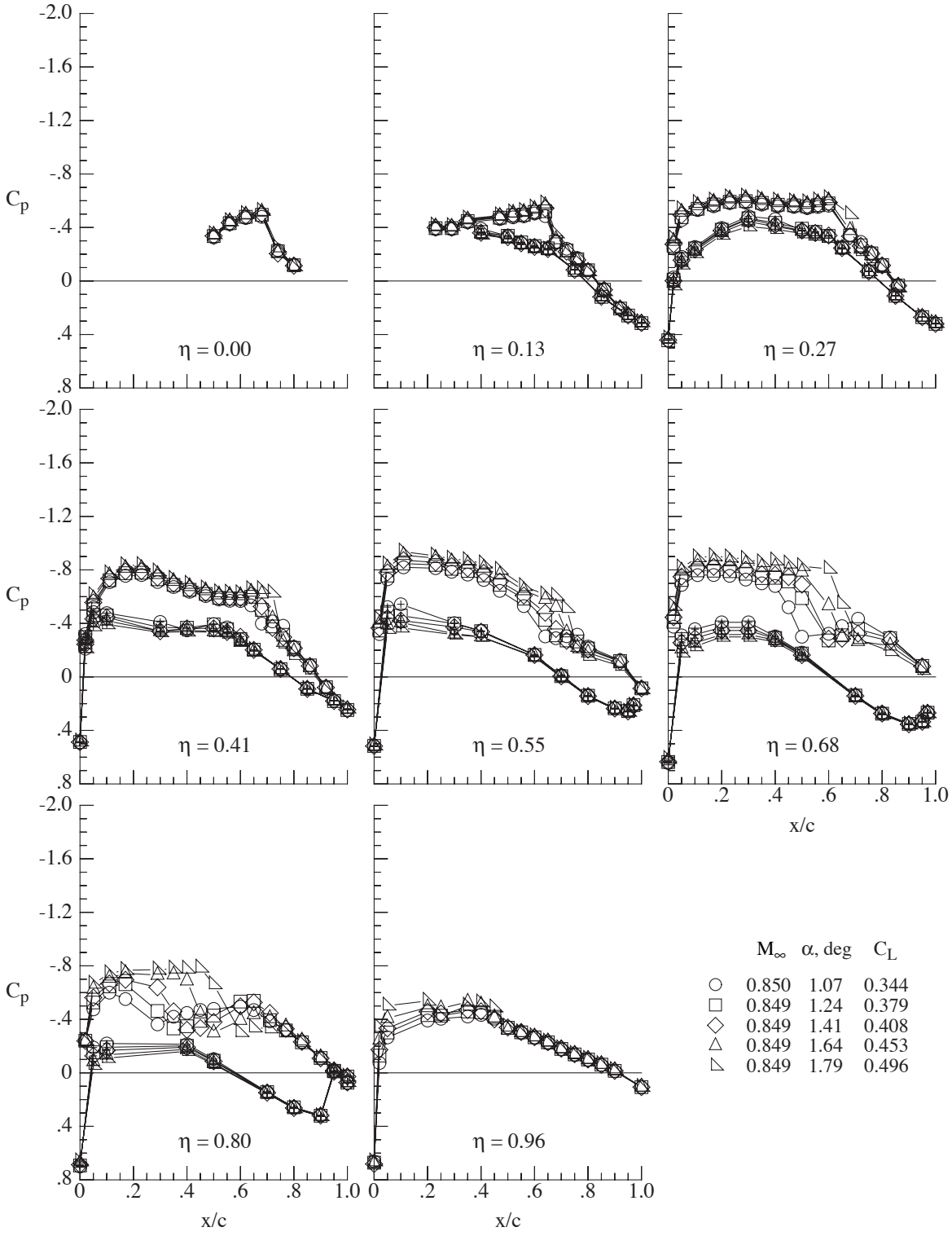

(a) Angle of attack from 1.07° to 1.79°.

Figure 38. Wing chordwise pressure coefficient variation at various angles of attack for the basic configuration at a Mach number of 0.85 and a Reynolds number of 25.0 x 10^6. Symbols with + indicate wing lower surface.

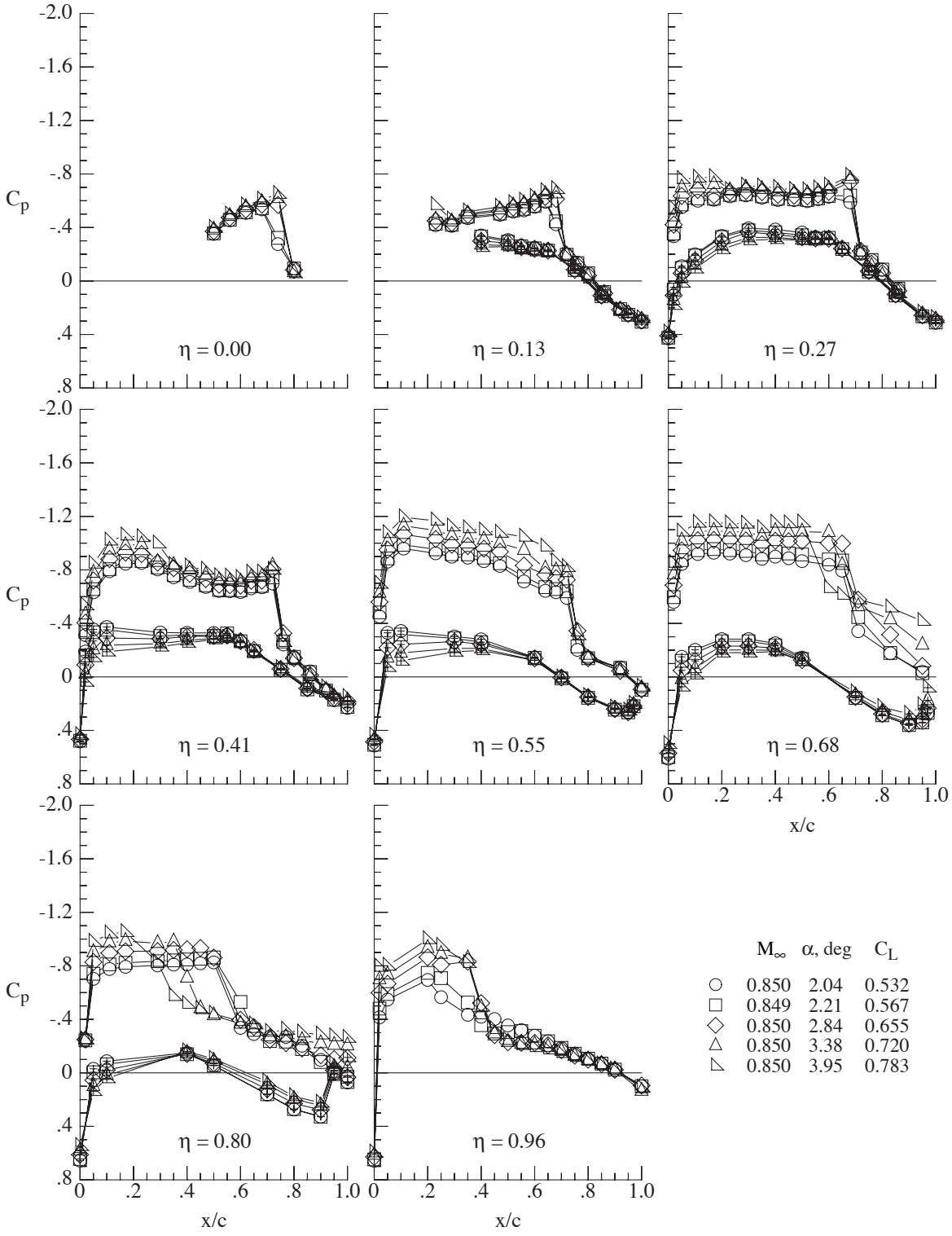

(b) Angle of attack from 2.04° to 3.95°.

Figure 38. Concluded.

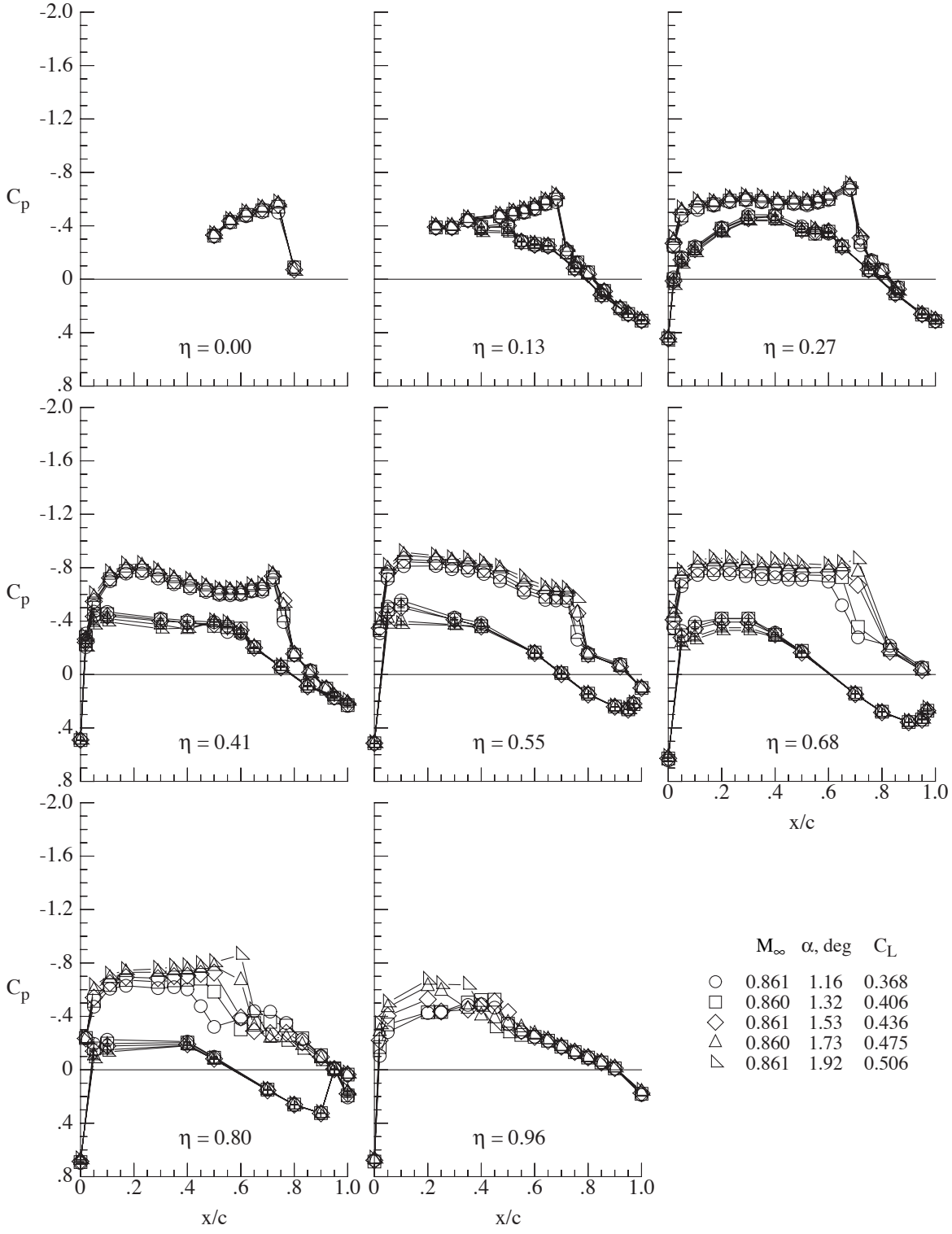

(a) Angle of attack from 1.16° to 1.92°.

Figure 39. Wing chordwise pressure coefficient variation at various angles of attack for the basic configuration at a Mach number of 0.86 and a Reynolds number of 25.0 x 10^6. Symbols with + indicate wing lower surface.

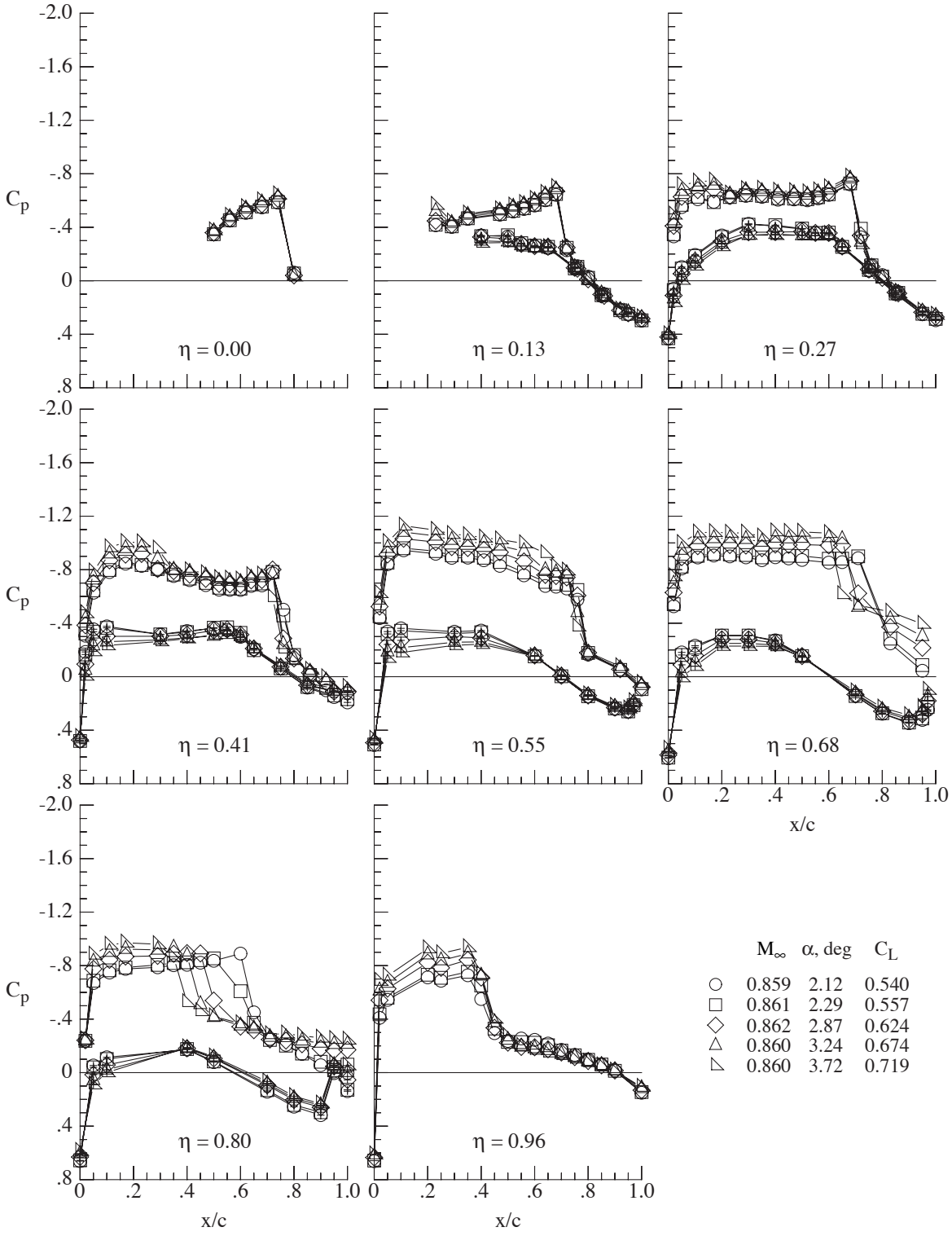

(b) Angle of attack from 2.12° to 3.72°.

Figure 39. Concluded.

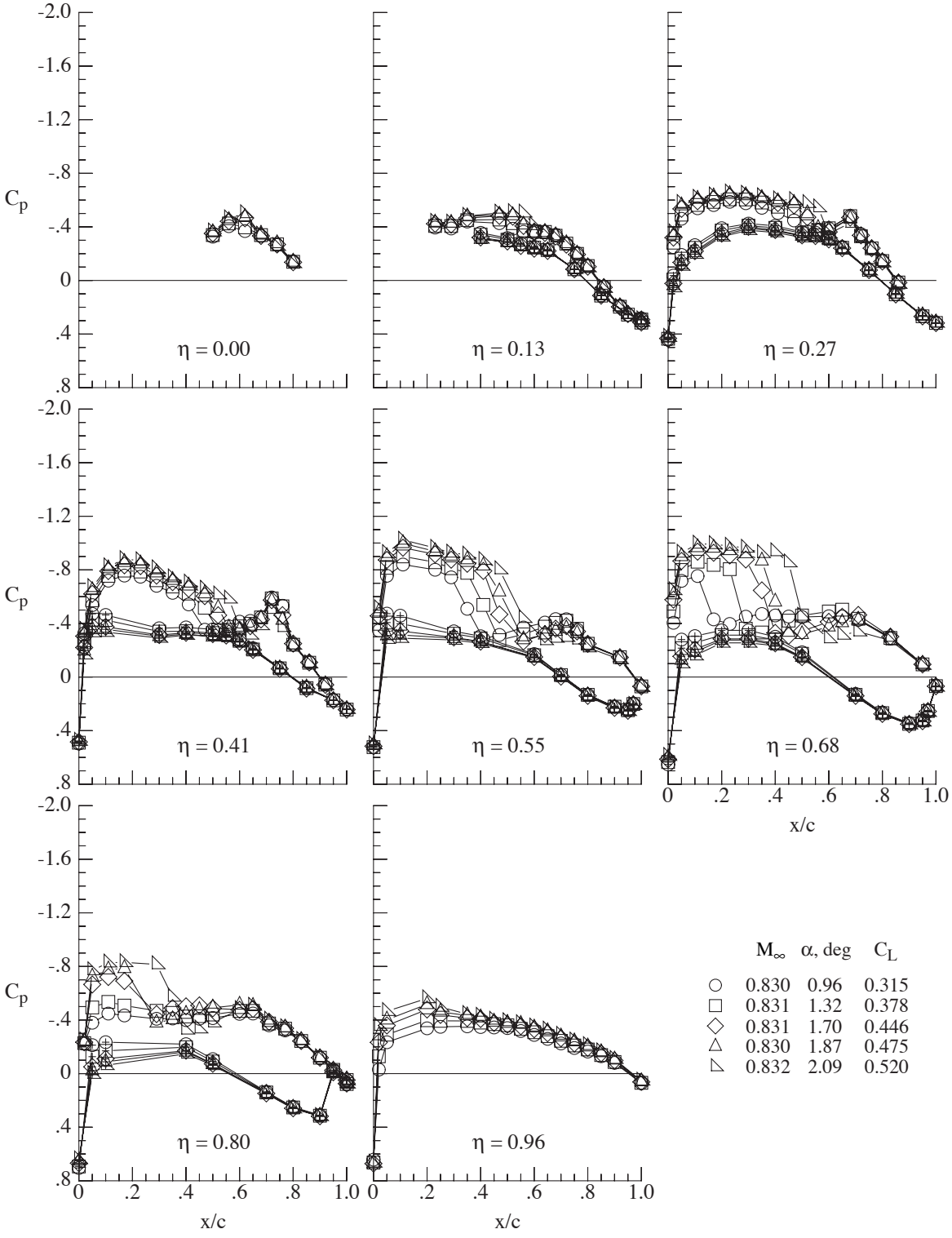

(a) Angle of attack from 0.96° to 2.09°.

Figure 40. Wing chordwise pressure coefficient variation at various angles of attack for the configuration with winglets at a Mach number of 0.83 and a Reynolds number of 25.0 x 10^6. Symbols with + indicate wing lower surface.

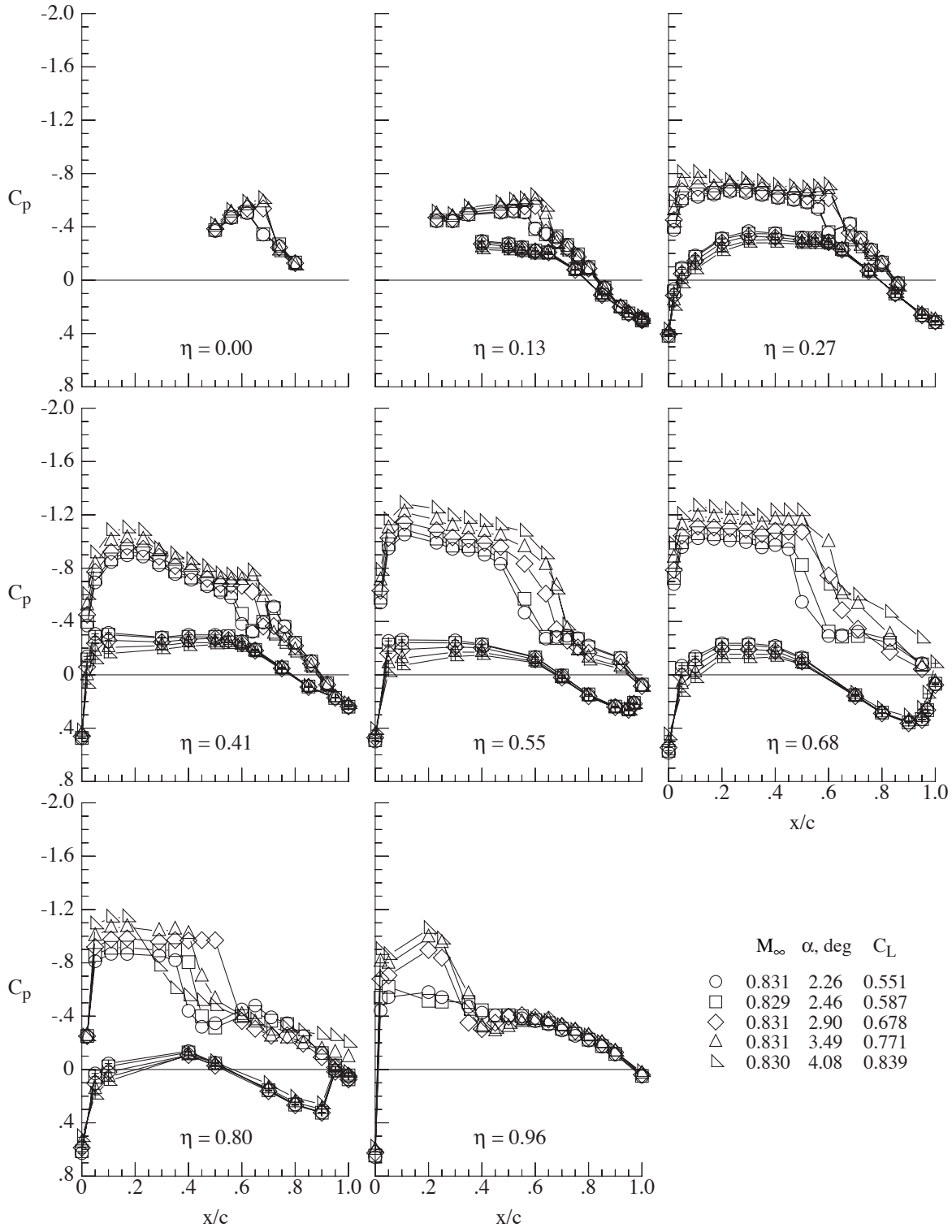

(b) Angle of attack from 2.26° to 4.08°.

Figure 40. Concluded.

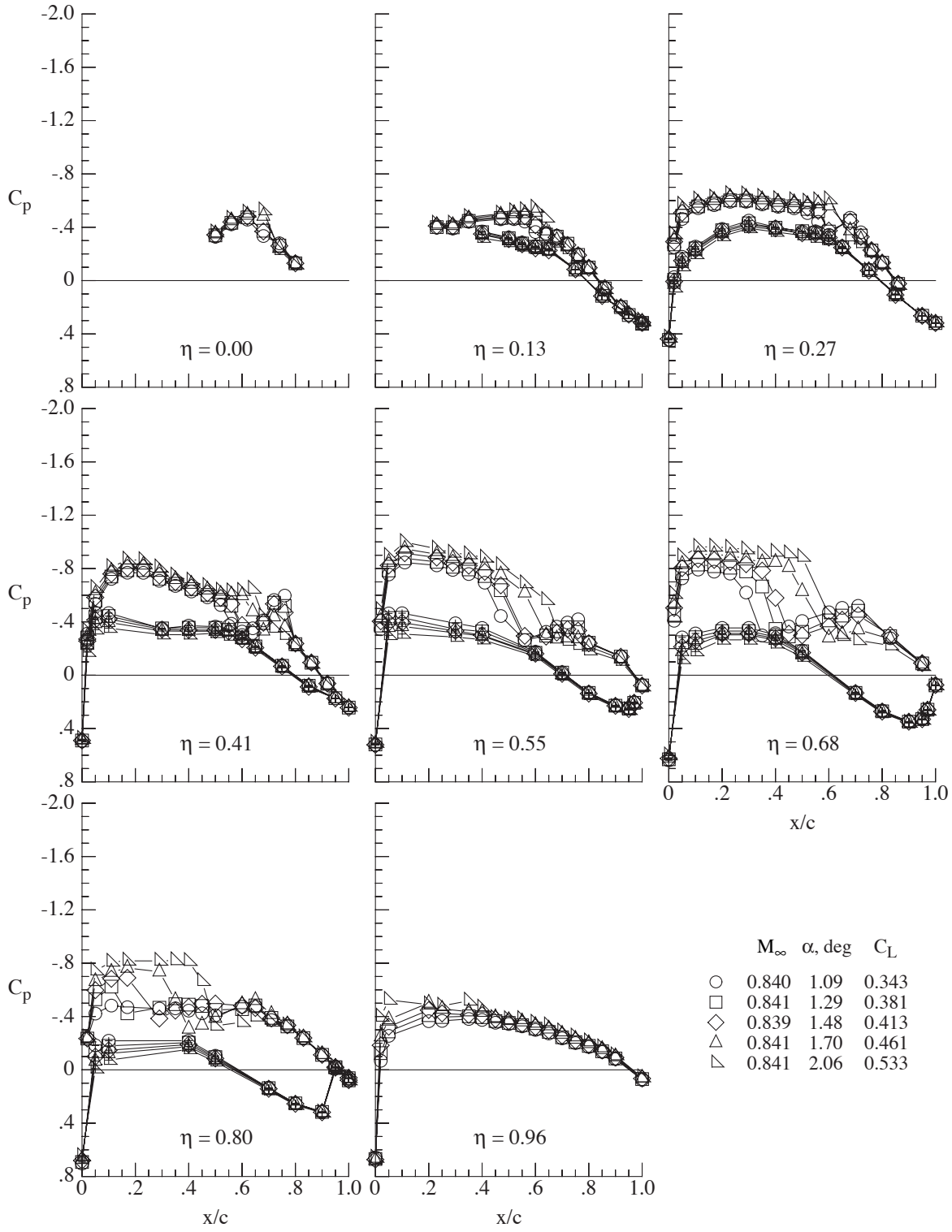

(a) Angle of attack from 1.09° to 2.06°.

Figure 41. Wing chordwise pressure coefficient variation at various angles of attack for the configuration with winglets at a Mach number of 0.84 and a Reynolds number of 25.0 x 10^6. Symbols with + indicate wing lower surface.

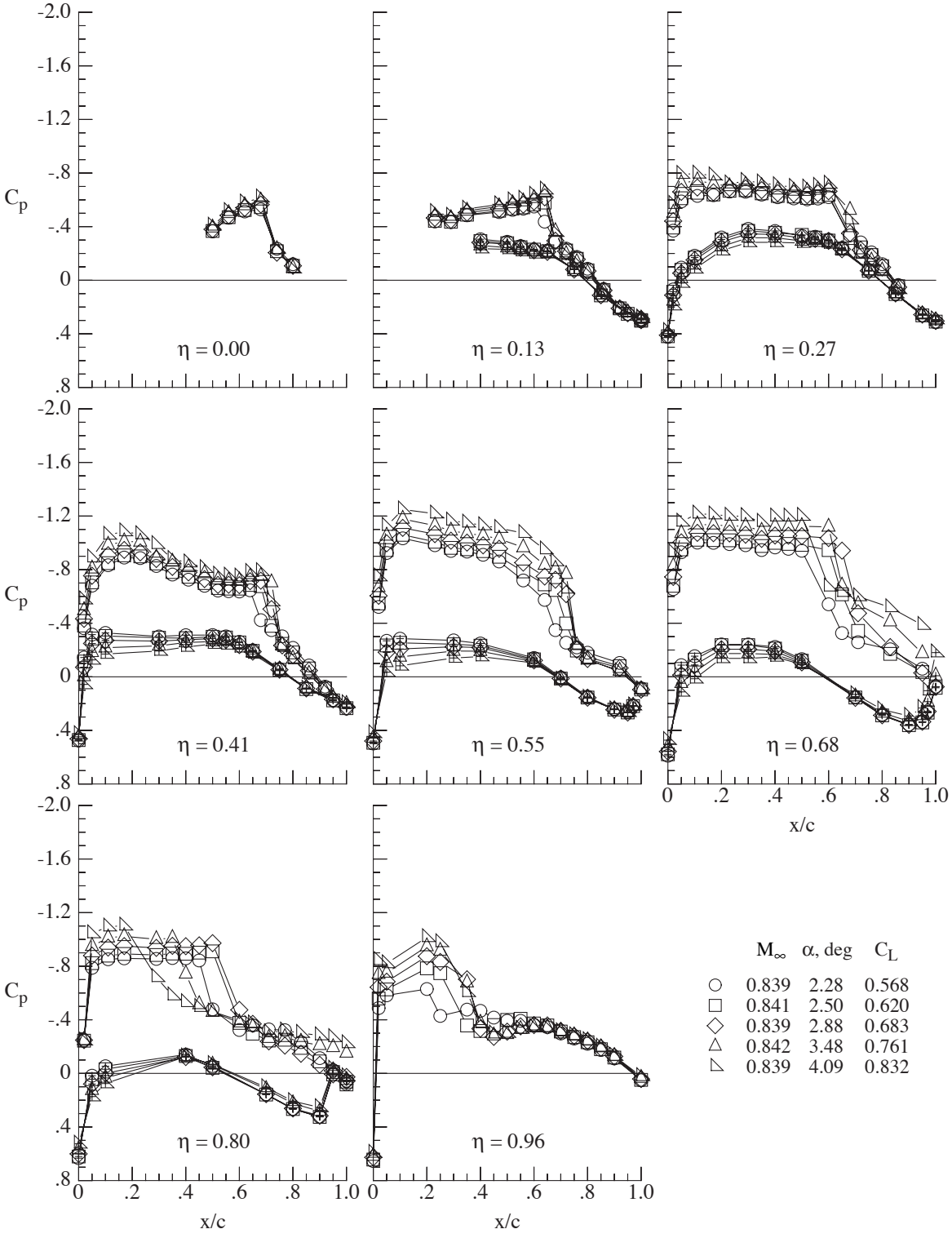

(b) Angle of attack from 2.28° to 4.09°.

Figure 41. Concluded.

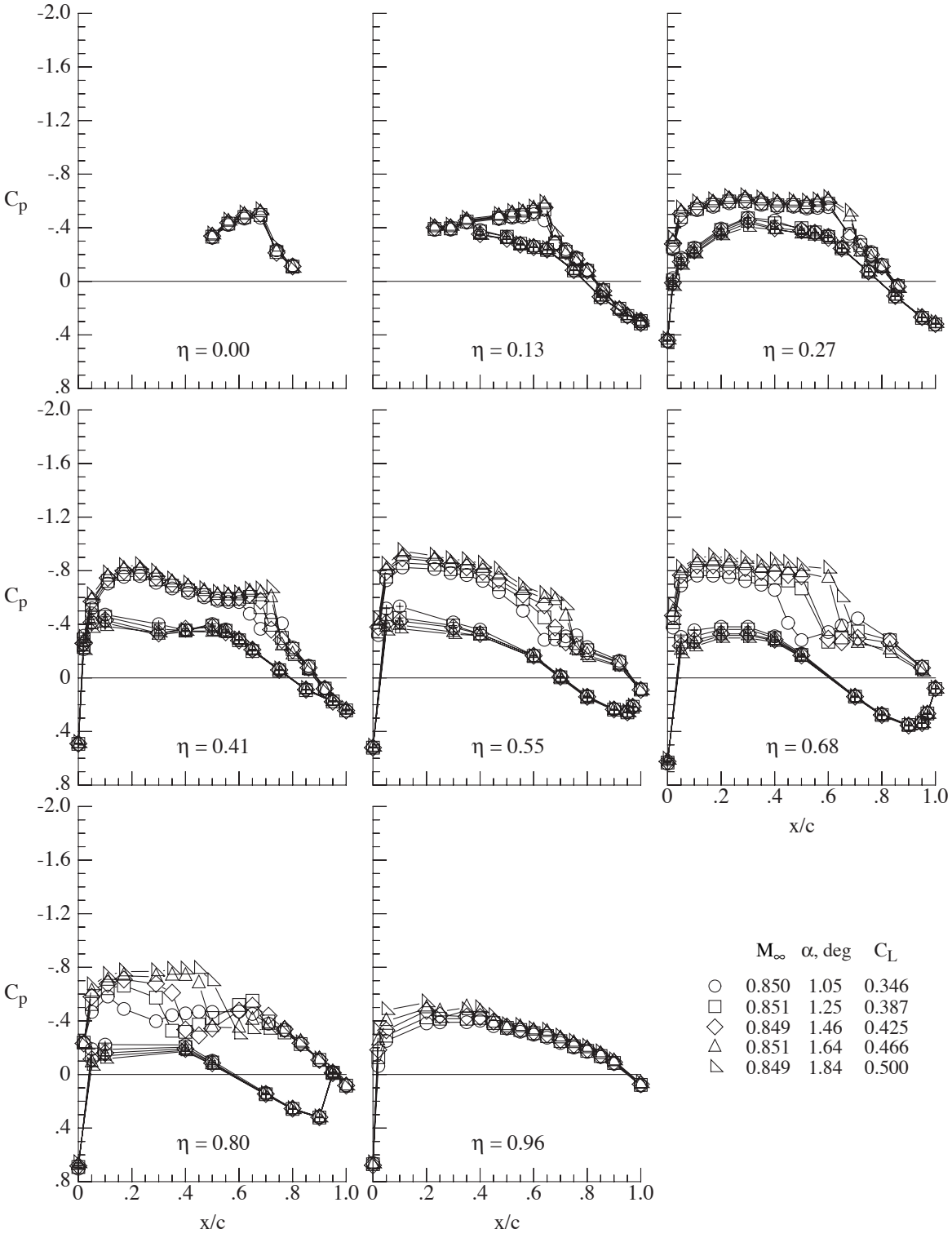

(a) Angle of attack from 1.05° to 1.84°.

Figure 42. Wing chordwise pressure coefficient variation at various angles of attack for the configuration with winglets at a Mach number of 0.85 and a Reynolds number of 25.0 x 10^6. Symbols with + indicate wing lower surface.

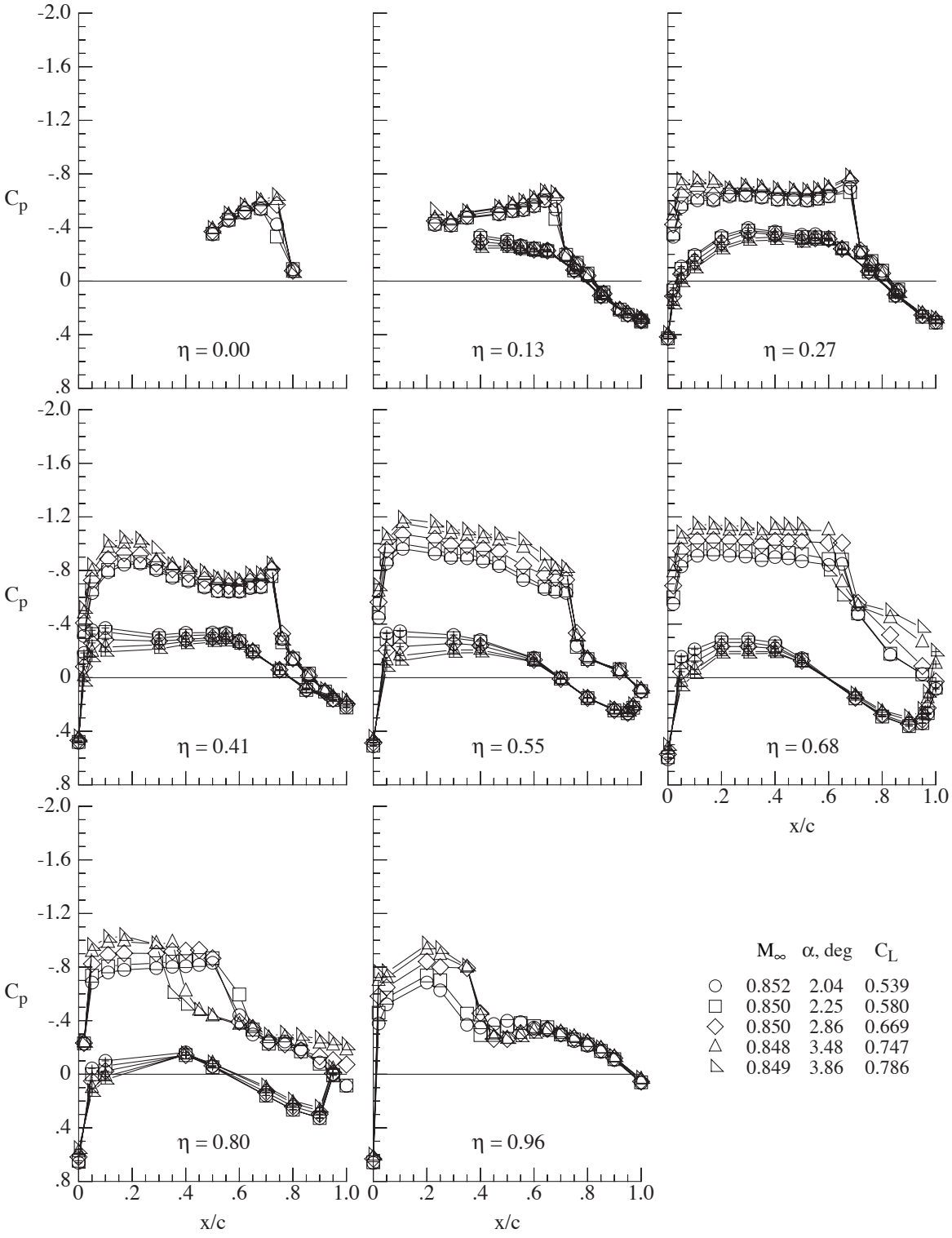

(b) Angle of attack from 2.04° to 3.86°.

Figure 42. Concluded.

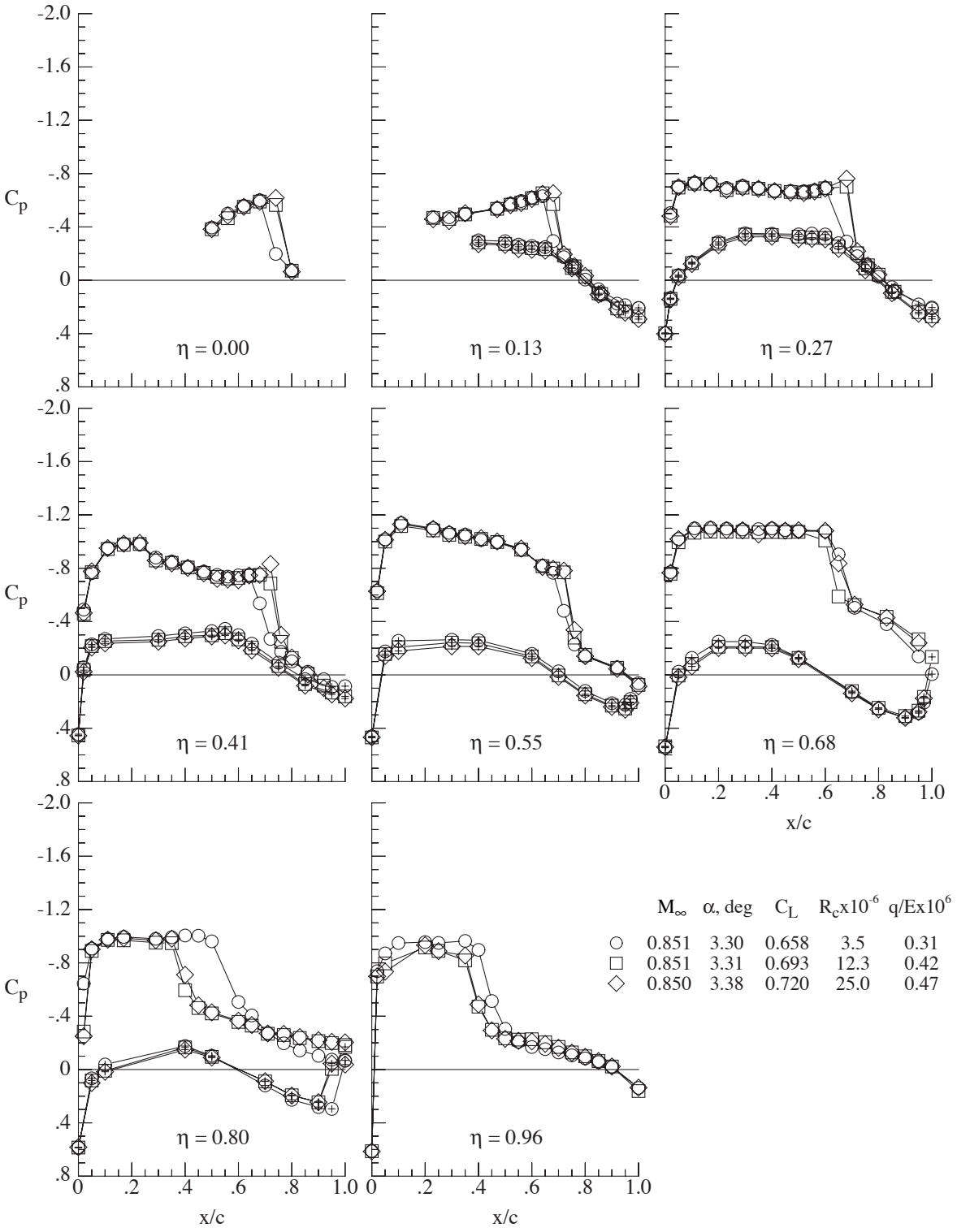

(a) Angle of attack of approximately 3.3°.

Figure 43. Comparisons of the effect of Reynolds number and dynamic pressure on wing chordwise pressure coefficient distributions for the basic configuration at a Mach number of 0.85. Symbols with + indicate wing lower surface.

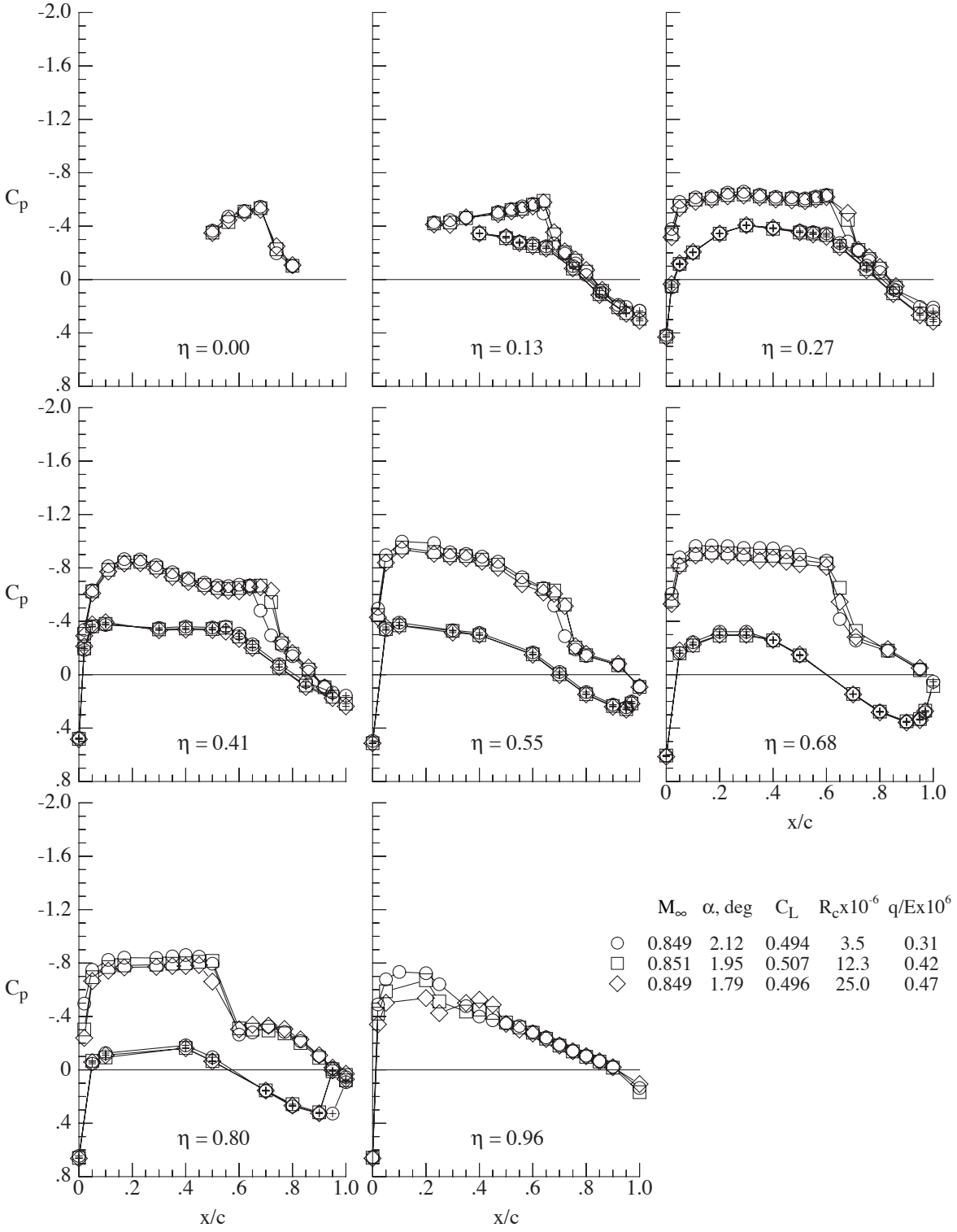

(b) Life coefficient of approximately 0.5.

Figure 43. Concluded.

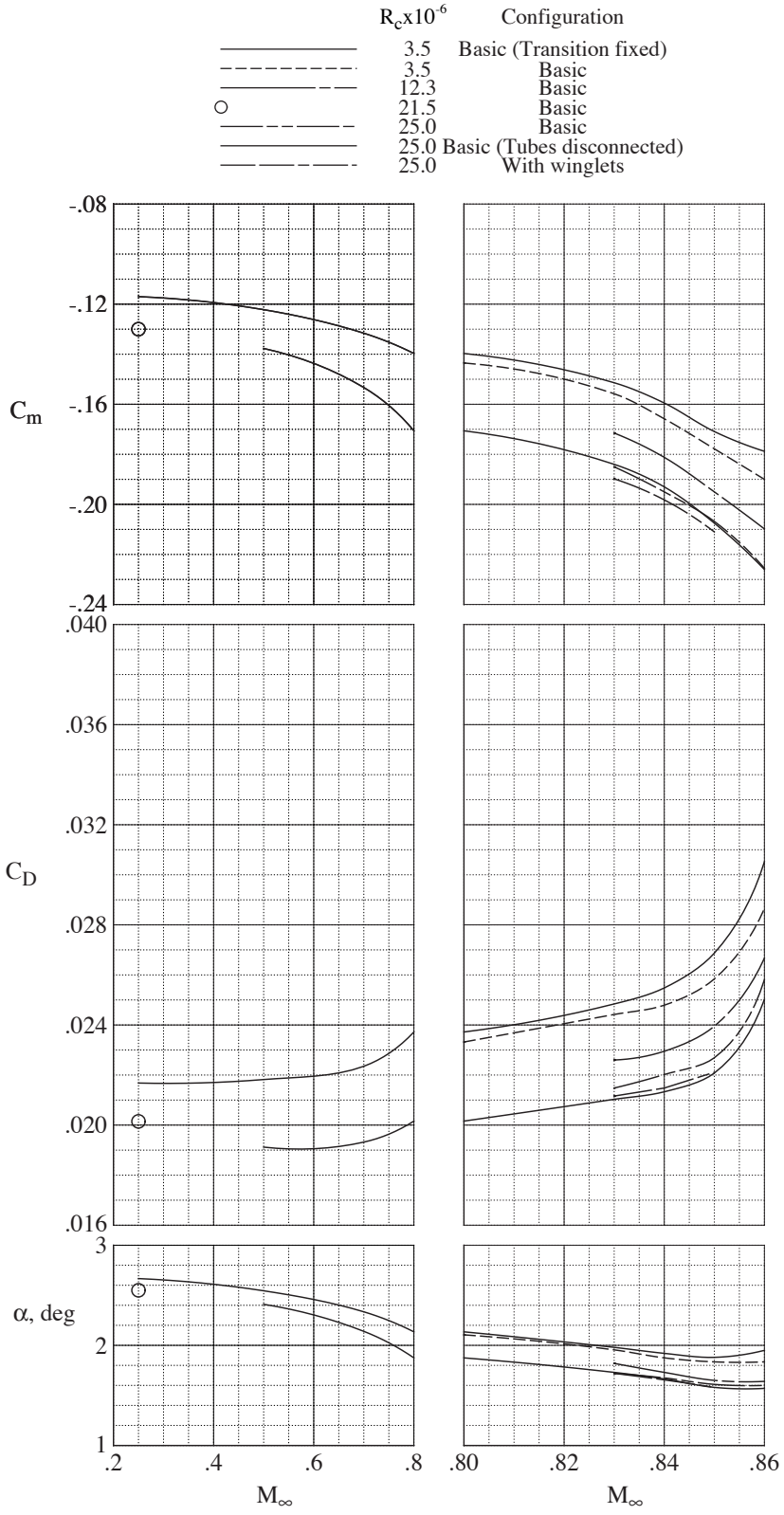

Figure 44. Effect of Mach number on angle of attack, drag coefficient, and pitching moment coefficient at a $C_L = 0.45$ for the model at various Reynolds numbers.

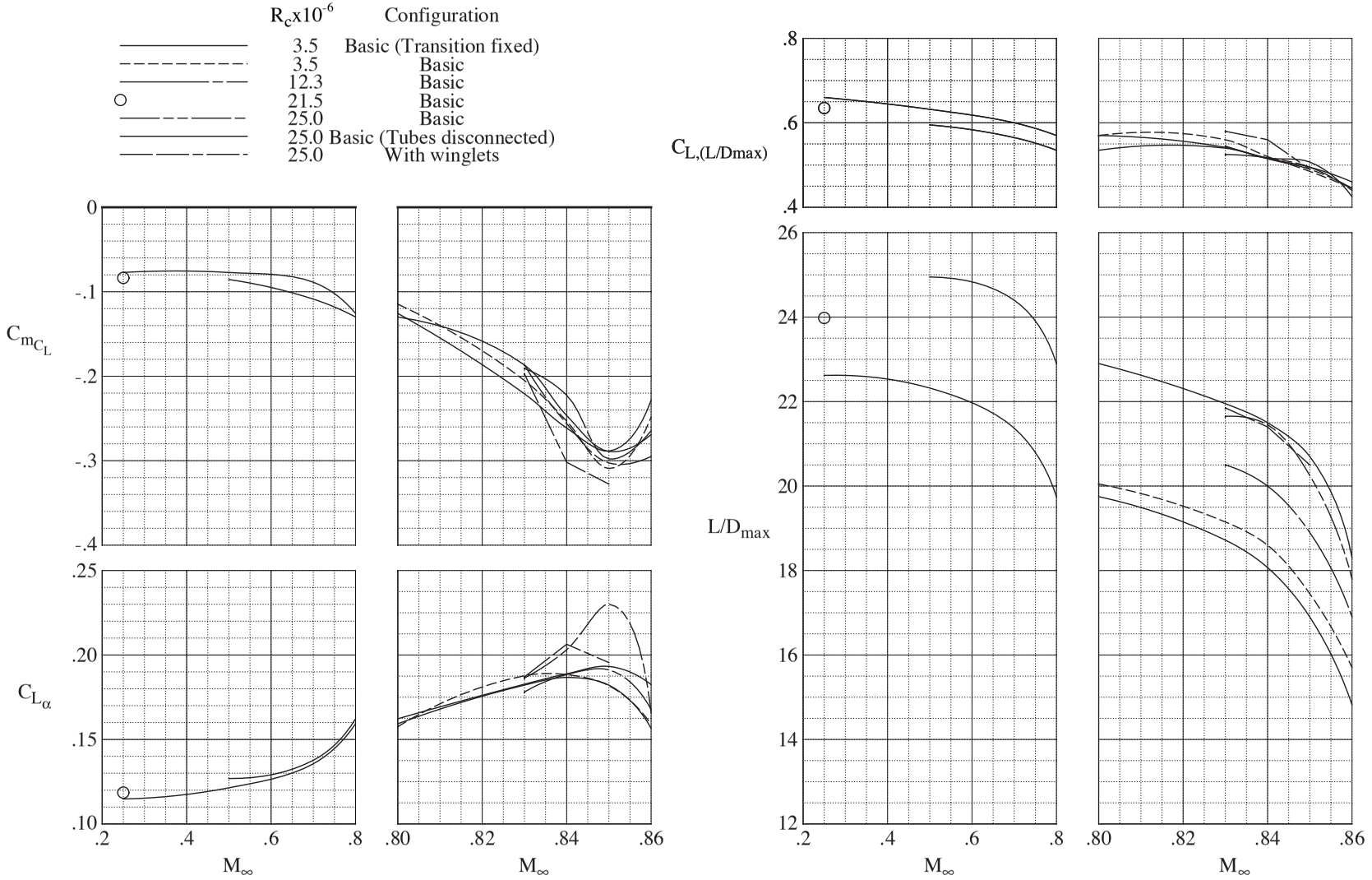

Figure 45. Effect of Mach number on lift curve slope and longitudinal stability at a $C_L = 0.45$ and maximum lift drag ratio and lift coefficient for maximum lift drag ratio for the model at various Reynolds numbers.

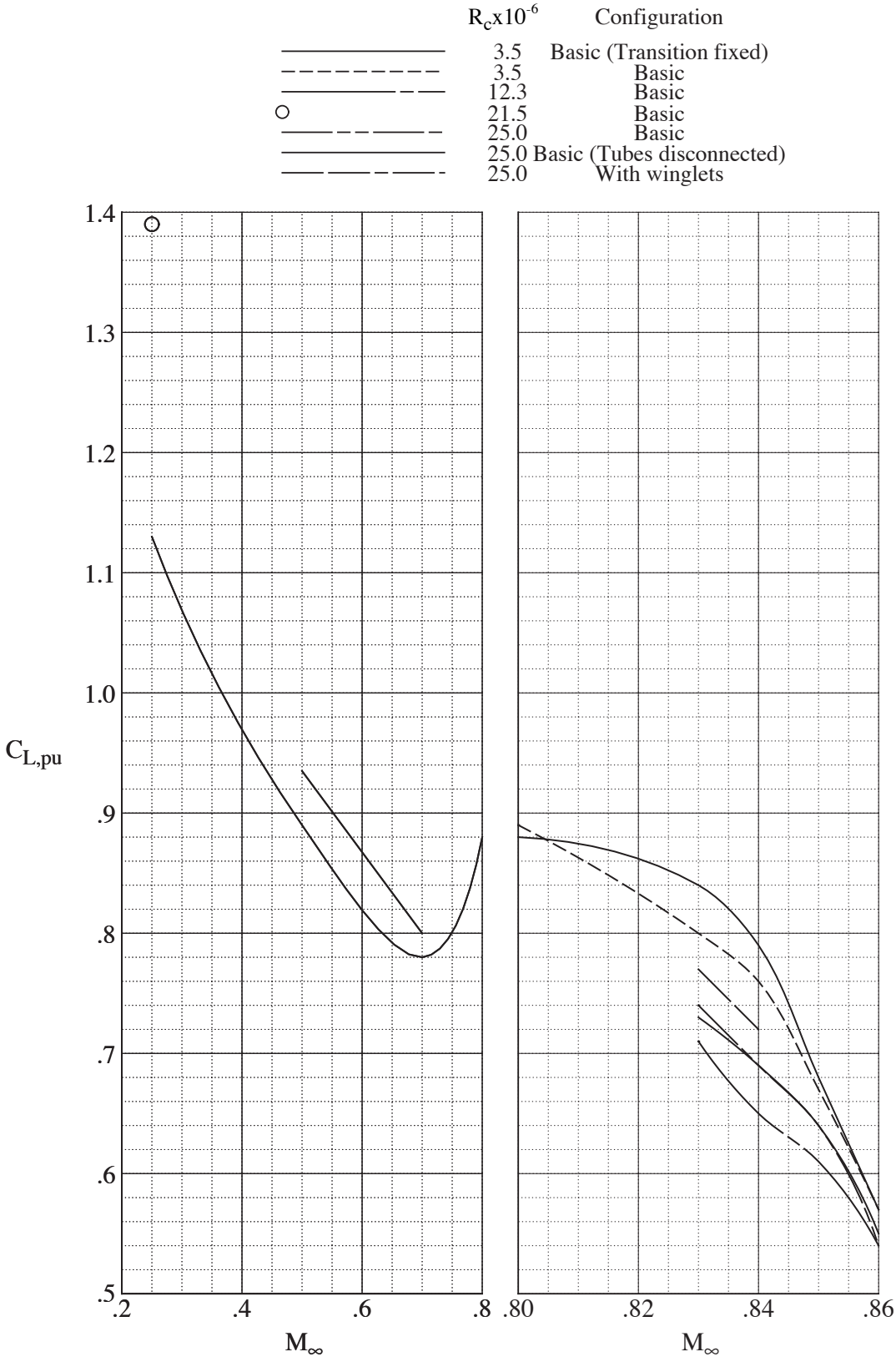

Figure 46. Effect of Mach number on lift coefficient at pitchup for the model at various Reynolds numbers.

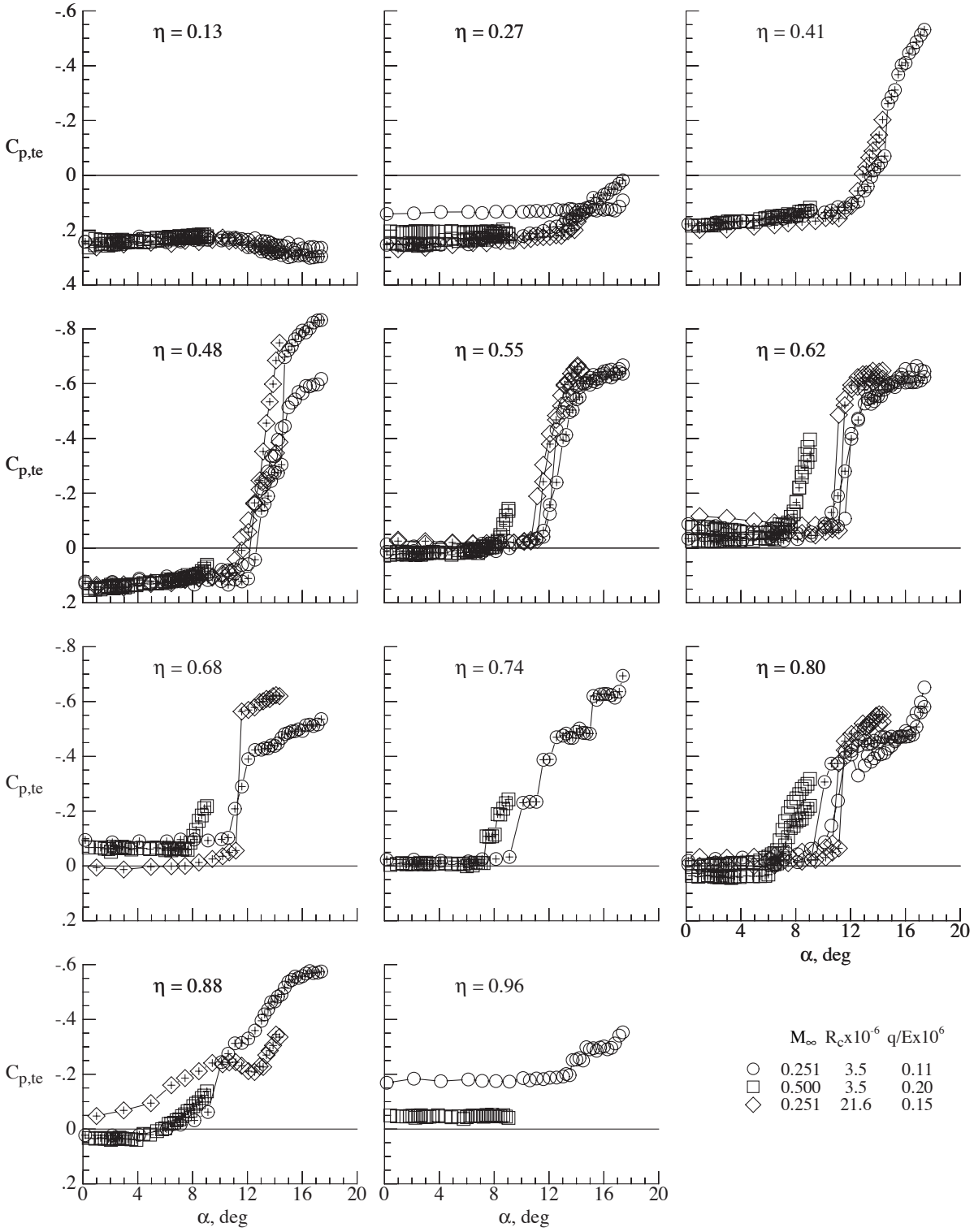

Figure 47. Variation of wing trailing edge pressure coefficient with angle of attack at Mach numbers 0.25 and 0.50 for the basic configuration at Reynolds numbers of 3.5 x 10^6 and 21.5 x 10^6. (Open symbols indicate trailing-edge orifices on right wing and symbols with plus signs indicate trailing-edge orifices on left wing.)

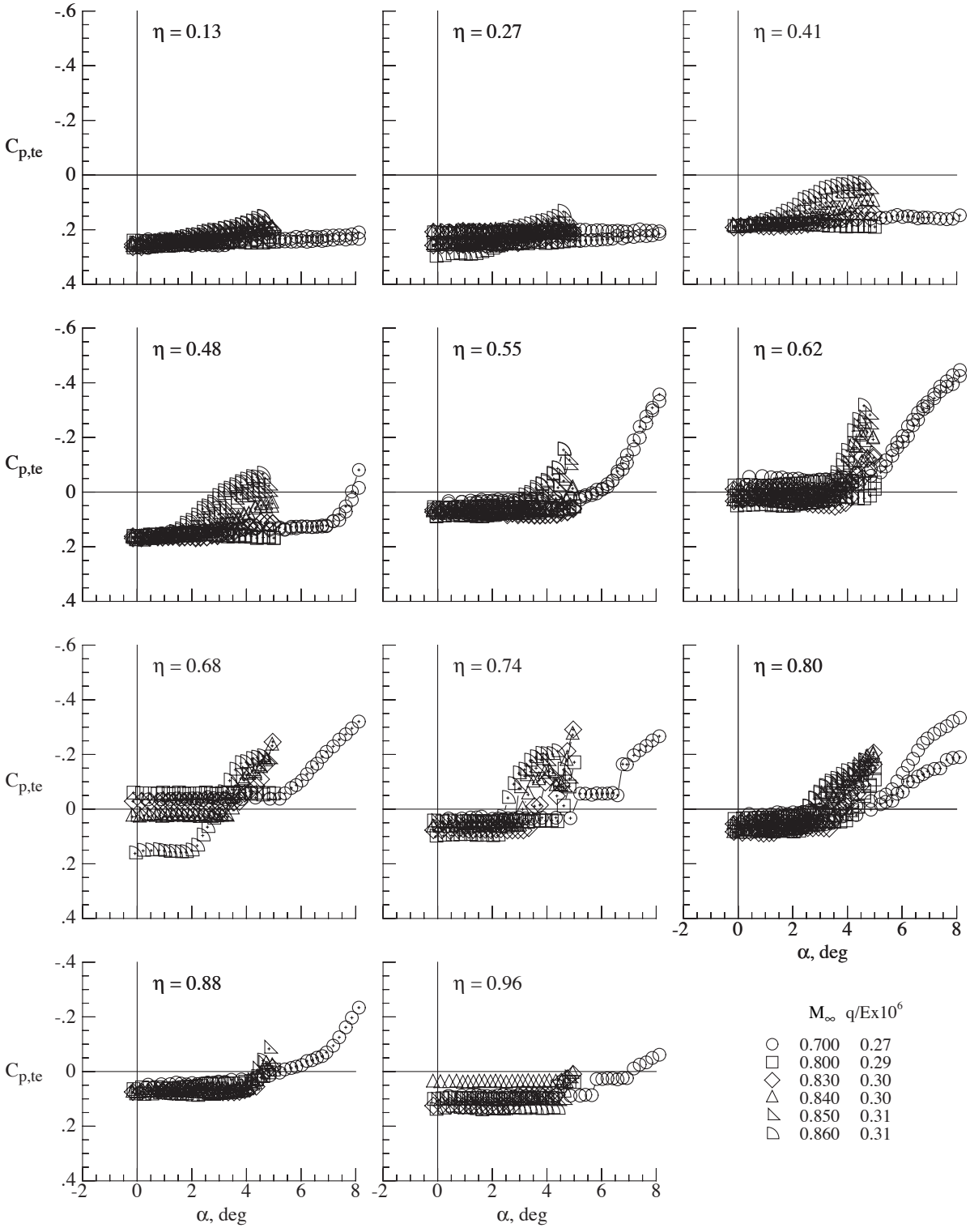

Figure 48. Variation of wing trailing edge pressure coefficient with angle of attack at Mach numbers greater than 0.50 for the basic configuration at a Reynolds number of 3.5 x 10^6. (Open symbols indicate trailing-edge orifices on right wing and symbols with plus signs indicate trailing-edge orifices on left wing.)

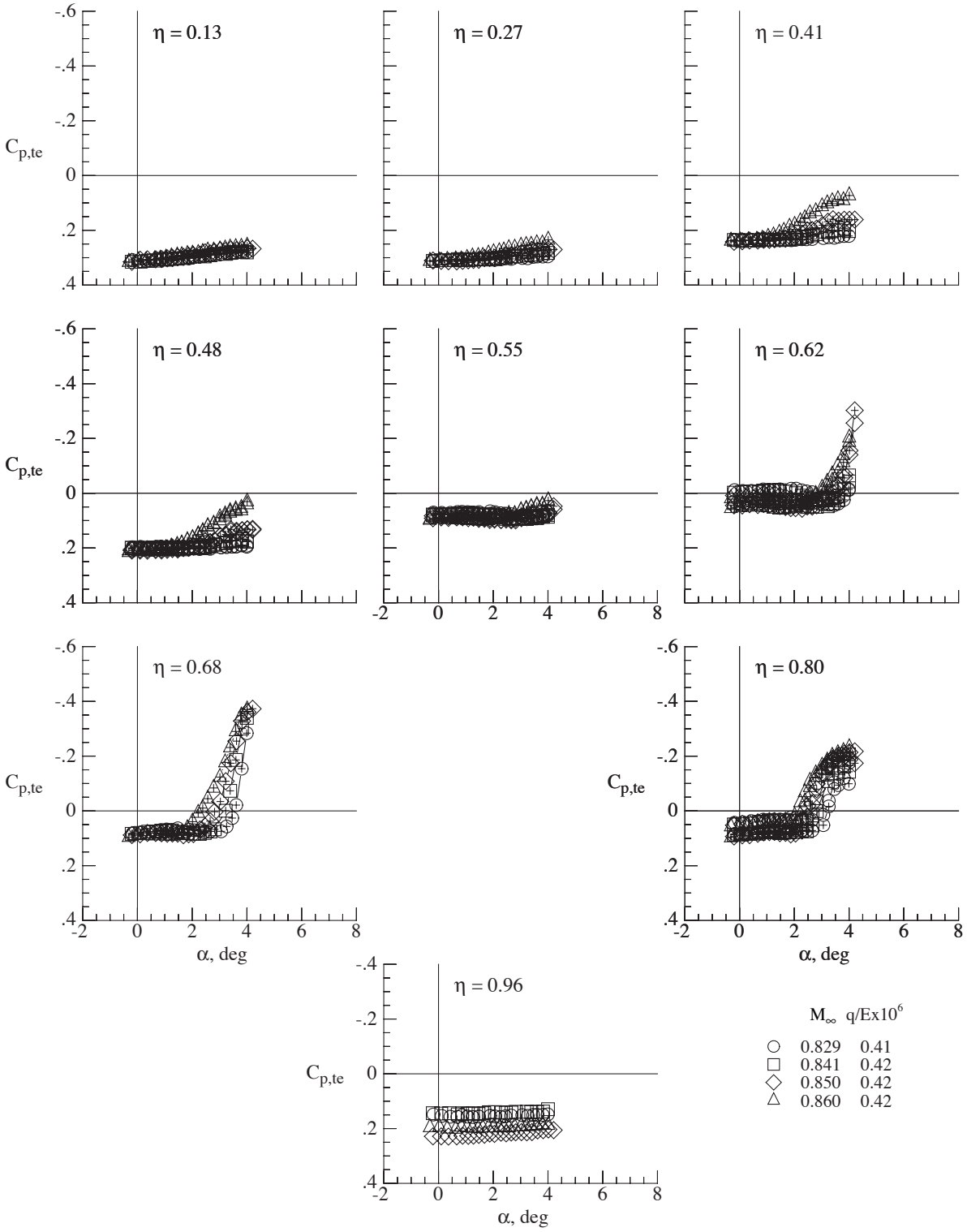

Figure 49. Variation of wing trailing edge pressure coefficient with angle of attack at Mach numbers greater than 0.80 for the basic configuration at a Reynolds number of 12.3 x 10^6. (Open symbols indicate trailing-edge orifices on right wing and symbols with plus signs indicate trailing-edge orifices on left wing.)

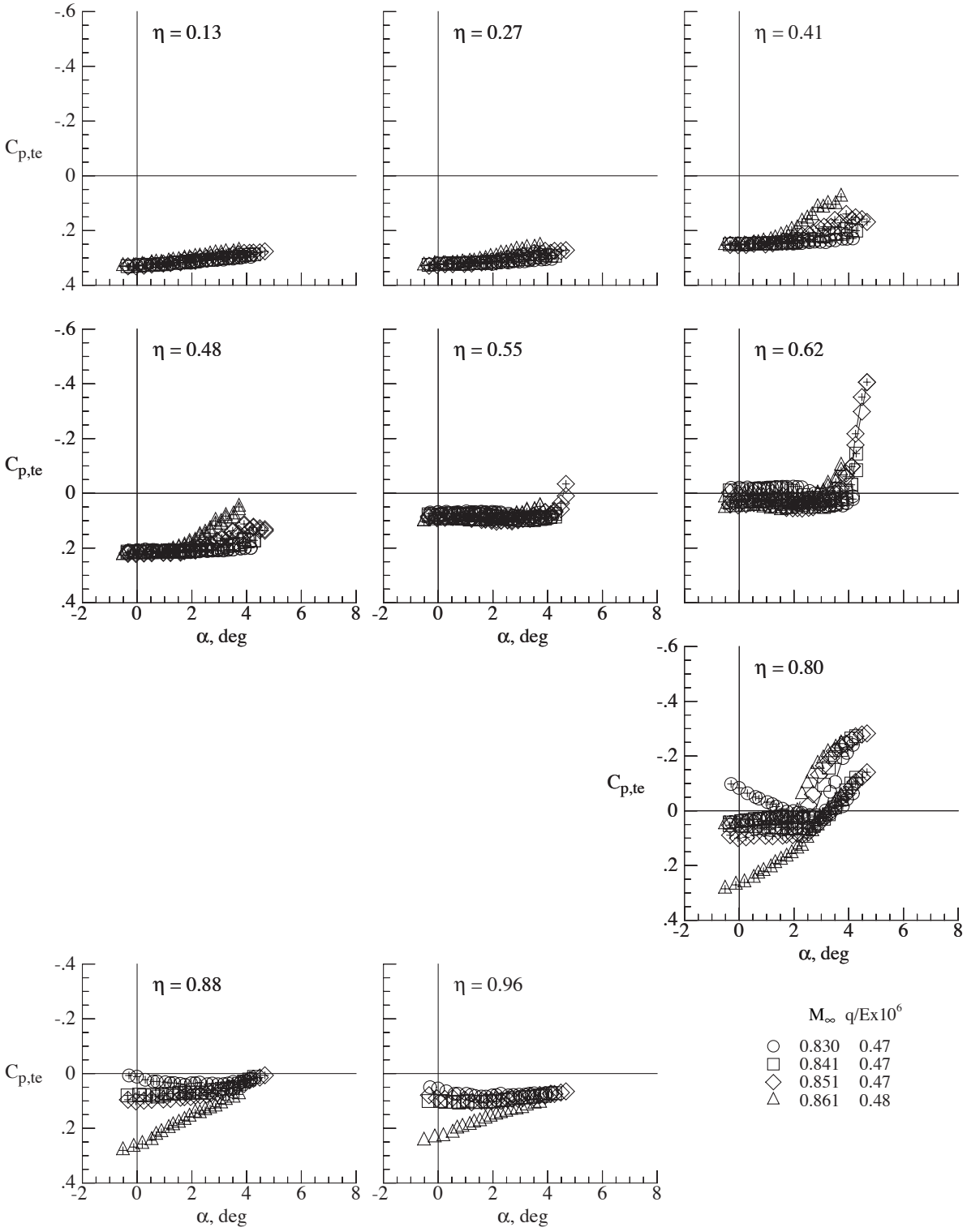

Figure 50. Variation of wing trailing edge pressure coefficient with angle of attack at Mach numbers greater than 0.80 for the basic configuration at a Reynolds number of 25.0 x 10^6. (Open symbols indicate trailing-edge orifices on right wing and symbols with plus signs indicate trailing-edge orifices on left wing.)

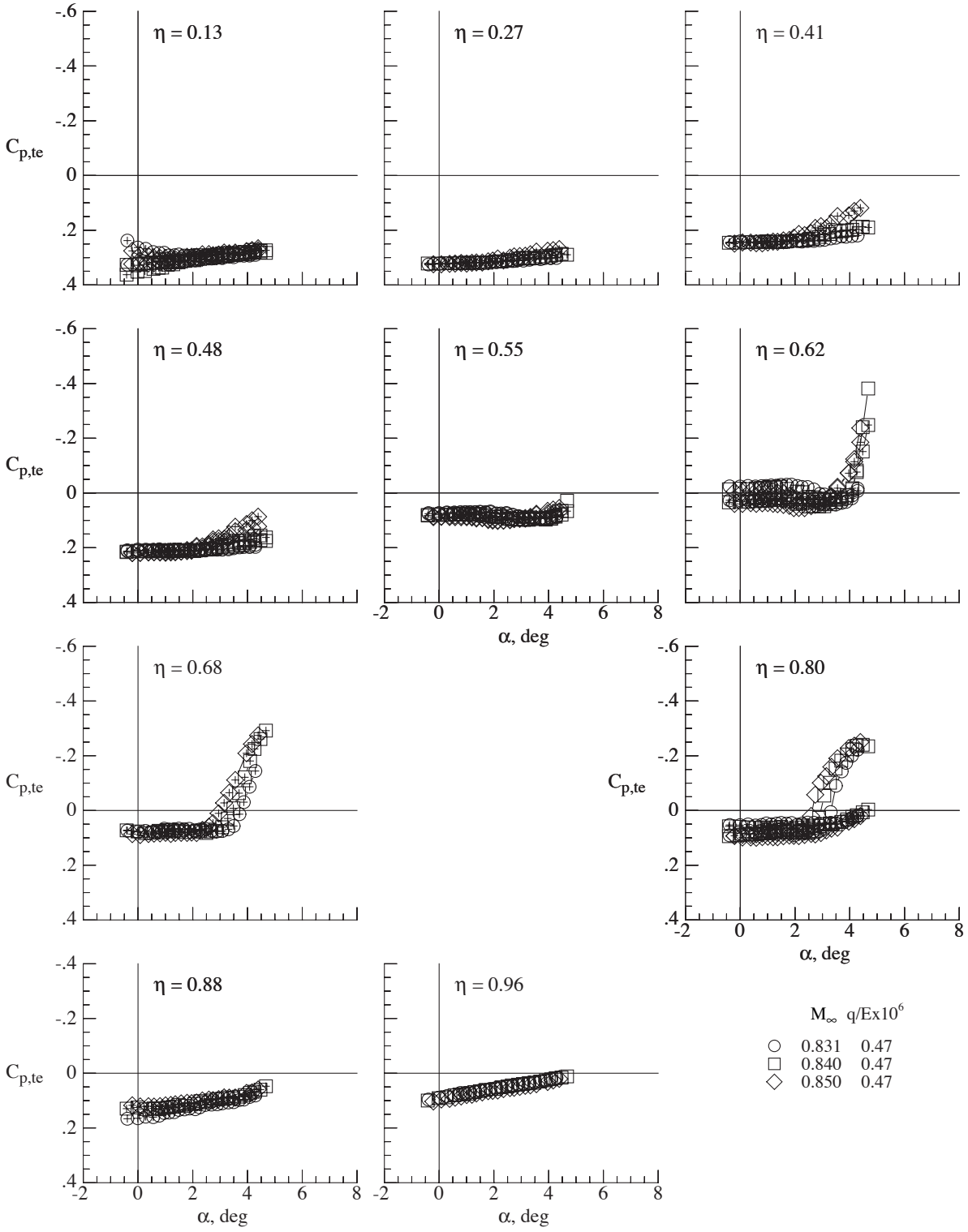

Figure 51. Variation of wing trailing edge pressure coefficient with angle of attack at Mach numbers greater than 0.80 for the configuration with winglets at a Reynolds number of 25.0 x 10^6. (Open symbols indicate trailing-edge orifices on right wing and symbols with plus signs indicate trailing-edge orifices on left wing.)

REPORT DOCUMENTATION PAGE

Form Approved
OMB No. 0704-0188

1. REPORT DATE *(DD-MM-YYYY)*	2. REPORT TYPE	3. DATES COVERED *(From - To)*
01- 08 - 2005	Technical Memorandum	

4. TITLE AND SUBTITLE

Longitudinal Aerodynamic Characteristics and Wing Pressure Distributions of a Blended-Wing-Body Configuration at Low and High Reynolds Numbers

5a. CONTRACT NUMBER

5b. GRANT NUMBER

5c. PROGRAM ELEMENT NUMBER

6. AUTHOR(S)

Re, Richard J.

5d. PROJECT NUMBER

5e. TASK NUMBER

5f. WORK UNIT NUMBER

23-714-80-VG

7. PERFORMING ORGANIZATION NAME(S) AND ADDRESS(ES)

NASA Langley Research Center
Hampton, VA 23681-2199

8. PERFORMING ORGANIZATION REPORT NUMBER

L-19113

9. SPONSORING/MONITORING AGENCY NAME(S) AND ADDRESS(ES)

National Aeronautics and Space Administration
Washington, DC 20546-0001

10. SPONSOR/MONITOR'S ACRONYM(S)

NASA

11. SPONSOR/MONITOR'S REPORT NUMBER(S)

NASA/TM-2005-213754

12. DISTRIBUTION/AVAILABILITY STATEMENT

Unclassified - Unlimited
Subject Category 02
Availability: NASA CASI (301) 621-0390

13. SUPPLEMENTARY NOTES

Re, Langley Research Center, Hampton, VA.
An electronic version can be found at http://ntrs.nasa.gov

14. ABSTRACT

Force balance and wing pressure data were obtained on a 0.017-Scale Model of a blended-wing-body configuration (without a simulated propulsion system installation) to validate the capability of computational fluid dynamic codes to predict the performance of such thick sectioned subsonic transport configurations. The tests were conducted in the National Transonic Facility of the Langley Research Center at Reynolds numbers from 3.5 to 25.0 million at Mach numbers from 0.25 to 0.86. Data were obtained in the pitch plane only at angles of attack from -1º to 8º at Mach numbers greater than 0.25. A configuration with winglets was tested at a Reynolds number of 25.0 million at Mach numbers from 0.83 to 0.86.

15. SUBJECT TERMS

NTF; Blended-wing-body; Reynolds number effects; Winglets

16. SECURITY CLASSIFICATION OF:			17. LIMITATION OF ABSTRACT	18. NUMBER OF PAGES	19a. NAME OF RESPONSIBLE PERSON
a. REPORT	b. ABSTRACT	c. THIS PAGE			STI Help Desk (email: help@sti.nasa.gov)
					19b. TELEPHONE NUMBER *(Include area code)*
U	U	U	UU	108	(301) 621-0390